DEVELOPMENT OF NOVEL 3D NMR-COMPATIBLE BIOREACTORS AND DYNAMIC NUCLEAR POLARIZATION (DNP) TECHNIQUES FOR THE STUDY OF REAL-TIME METABOLISM

Kayvan Rahimi-Keshari

A dissertation submitted to the faculty of the University of North Carolina at Chapel Hill in partial fulfillment of the requirements for the degree Doctor of Philosophy in the Department of Biomedical Engineering.

Chapel Hill
2009

Approved by,

Jeffrey M. Macdonald, PhD

Michael P. Gamcsik, PhD

Oleg Favorov, PhD

John Kurhanewicz, PhD

Daniel B. Vigneron, PhD

©2009
Kayvan Rahimi-Keshari
ALL RIGHTS RESERVED

ABSTRACT

KAYVAN RAHIMI-KESHARI: Development of novel 3D NMR-compatible bioreactors and dynamic nuclear polarization (DNP) techniques for the study of real-time metabolism
(Under the direction of Jeffrey M. Macdonald, PhD)

It is well known that ^{13}C NMR spectroscopy (as well as other nuclei) has been limited in its ability to characterize metabolic states due to its low sensitivity. This low sensitivity is a result of the low natural abundance of ^{13}C (1.1%) in addition to the low gyromagnetic ratio of carbon. Traditionally, this is compensated by high sample concentrations as well as the introduction of ^{13}C-enriched substrates. Dynamic nuclear polarization (DNP) results from the coupling of nuclear spins in an amorphous solid, at ~1°K, to unpaired electrons of a stable organic free radical and their subsequent irradiation. Recent advances in the field of low temperature physics, electronic paramagnetic resonance (EPR) and NMR have provided for the adaptation of the DNP technique, to metabolically appreciable systems.

NMR-compatible engineered bioreactor and 3D perfusion systems have been used to study cellular metabolism on the order of hours primarily by ^{31}P and ^{13}C metabolic tracers. Due to the inherent ability to translate *in vitro* derived biomarkers to clinical *in vivo* MRI/MRSI, these model systems have been of great interest, though they have been limited by low sensitivity.

In this dissertation, methods are described to combine hyperpolarized techniques with an NMR-compatible bioreactor and observe *real time* metabolism in a fluidized packed bed design of rat hepatoma cells (JM1). This was extended to a novel hollow fiber bioreactor design, which provided the advantage of immobilization of cells and tissues for imaging. Prostate adenocarcinoma cells (PC3) and primary prostate tissue slices were shown to be viable for greater than 2 days demonstrating the long-term viability of these culture systems. Real time metabolism via hyperpolarized MR was also observed in the hollow fiber cartridge with the potential for future primary culture experiments. Additionally, new hyperpolarized probes and techniques (secondary and multi-probe polarization) that allow the study of metabolism, physiology (pH, apoptosis/necrosis, bioenergetics), and ligand-host binding were developed and tested. In summary, the findings of this dissertation research demonstrate the feasibility of fusing hyperpolarized MR with new NMR-compatible bioreactors to provide a robust platform for studying biological systems as well as chemical reactions useful in drug design and development.

ACKNOWLEDGEMENTS

Though the completion of a doctoral dissertation requires years of coursework and research, its most vital requirement is the support of family and friends. I am especially indebted to my parents, brother and sister for their support and advice through this process. Additionally I'd like to thank my thesis advisors, Jeff and John, for being willing to look past my shortcomings and guide me through this endeavor.

In the 10th century epic *Shahnameh*, the Persian poet Ferdowsi states the following immortal words:

بناهای آباد گردد خراب
ز باران و از تابش آفتاب

پی افکندم از نظم کاخی بلند
که از باد و باران نیابد گزند

از آن پس نمیرم که من زندهام
که تخم سخن را پراکندهام

هر آنکس که دارد هش و رای و دین
پس از مرگ بر من کند آفرین

With that in mind, this dissertation is my word.

TABLE OF CONTENTS

LIST OF TABLES viii

LIST OF FIGURES ix

Chapter

1. Introduction and Background 1

- 1.1 Specific Aims of Project 1
- 1.2 Steady State and Non-Steady State Enzyme Kinetics 3
- 1.3 NMR studies of Biochemical Kinetics 10
- 1.4 DNP Physics: the Solid State Effect and Hyperpolarization 12
- 1.5 Current developments in NMR-compatible Bioreactor Culture Systems 20

2. Fluidized Bioreactor and Hyperpolarized NMR 27

- 2.1 Design of Fluidized Bioreactor System and Methods 27
- 2.2 Steady State Metabolism of JM1 cells (^{31}P and ^{13}C) 35
- 2.3 Real-time DNP Measurements of JM1 Cell Metabolism 39

3. Cartridge Bioreactor Design and Hyperpolarized NMR 46

- 3.1 Design of Cartridge Bioreactor System 46
- 3.2 Oxygen Diffusion as it Applies to Bioreactor Development 48
- 3.3 Characterization of Cartridge System by Steady State (^{31}P), Dynamic measurements (^{13}C), and Imaging in Human Prostate Cells and Tissues 55
- 3.4 Prostate Cancer Metabolism in Human Biopsies and Comparison to Bioreactor Studies 66

4. Hyperpolarized Metabolic Tracer and Probe Development 78

- 4.1 Secondary Labeling by Acetic Anhydride and Extension to Short Peptides 78
- 4.2 Polarization of Hexoses: Fructose 99
- 4.3 Binding by DNP 112

4.4 Other Novel Compounds 117
4.5 Multipolarization 125

5. Conclusions and Future Directions 143
5.1 Next Generation NMR-compatible Bioreactors 144
5.2 Future Developments in Hyperpolarized Probes 145
5.3 The "Proof is in the Pudding" 146

APPENDIX A: Fluidized Bioreactor 148
APPENDIX B: Cartridge Bioreactor 151
APPENDIX C: Culture Media 153

REFERENCES 157

LIST OF TABLES

Table

2.1 Metabolite Concentrations for JM1 cell 2D cultures 37

4.1 Secondarily Acetylated Amino Acids 87

4.2 Secondarily Acetylated Glycine, Diglycine and Triglycine 91

4.3 T_1 relaxation times at 11.7T and 3T and
percent polarization for each Fructose Isomer 105

4.4 Spin-lattice Relaxation Values and Percent Polarization
Achieved for Multi-compound Polarization at 11.7T 138

LIST OF FIGURES

Figure

1.1 LDH Enzymatic Conversion of Pyruvate to Lactate 8

1.2 Formation of Enol-Pyruvate-Adduct 9

1.3 Titration of Steady State Lactate Synthesis with External Pyruvate 10

1.4 Percent Polarization as a function of Temperature 15

1.5 Graphical Representation of Spin Polarization 15

1.6 Graphical Representation of DNP Polarizer and High Field NMR system 17

2.1 Schematic of Bioreactor Setup 31

2.2 Representative ^{1}H Spectrum and TOCSY Spectra of JM1 cell extracts 36

2.3 JM1 Cell Metabolism – Distribution of ^{13}C Label 38

2.4 Representative ^{31}P Spectra and Histology of Encapsulated JM1 cells 39

2.5 ^{31}P monitoring and dynamic ^{13}C Spectra of JM1 cells 40

2.6 Dynamic ^{13}C Spectra of JM1 cells with LDH and ALT Flux 42

3.1 Schematic of Bioreactor Cartridge 47

3.2 Schematic of Simplified Culture Dish 48

3.3 Gas Diffusion with Time and Depth 51

3.4 Estimated Steady State Concentrations of Oxygen in a Slice through a HF 54

3.5 ^{31}P Spectrum of PC3 cells at 44 hours of Perfusion 58

3.6 Hyperpolarized ^{13}C Spectra in a PC3 cell Bioreactor 58

3.7 Copolarization in a PC3 cell Bioreactor 59

3.8 Hyperpolarized [2-^{13}C] Fructose in aPC3 cell Bioreactor 60

3.9 Hyperpolarized [1-^{13}C] Glycine in a PC3 cell Bioreactor 61

3.10 ^{31}P Time Course in a Prostate Tissue Slice Bioreactor 63

3.11 ^{31}P spectrum at 63 hours in the Bioreactor 64

3.12 Diffusion-weighted Images of Tissue Slices 65

3.13 ^{13}C Summed Spectrum in Tissue Slices 65

3.14 Hyperpolarized EPI images of Pyrvate Distribution 66

3.15 ^{13}C Spectra of Lactate in a Tissue Slice Bioreactor 66

3.16 Visualization of Mutual Information with Respect to Entropy 71

3.17 Power of Spectral Clustering 72

3.18 Representative ^{1}H HR-MAS Spectra of Human Prostate Biopsies 73

3.19 Metabolite Concentrations for Predominantly Glandular, Stromal and Cancer Groups 74

3.20 Spectral Clustering of 126 Human Biopsies 75

4.1 General Strategy for Secondary Hyperpolarization 85

4.2 Hyperpolarized Spectrum of Amino Acids 86

4.3 Thermal Spectrum corresponding to Hyperpolarized Amino Acids 89

4.4 Sample Dynamic Data Set of Hyperpolarized [1,1-^{13}C] Acetic Anhydride and Glycine 90

4.5 Chemical Structure of N-acetyl MSH 92

4.6 Generation of Hyperpolarized Acetylcysteine 93

4.7 Hyperpolarized RGD 94

4.8 Hyperpolaried RGD in a TRAMP Mouse 95

4.9 Mechanism of GLUT5 Transport and Metabolism of Fructose 101

4.10 Natural Abundance and Hyperpolarized Spectra of Fructose 102

4.11 Enzymatic conversion of Fructose to Fructose-6-Phosphate 107

4.12 Hyperpolarized Fructose in a TRAMP Mouse 108

4.13 Hyperpolarized Fructose in a Diffuse Tumor 110

4.14 Hyperpolarized Benzoic Acid 113

4.15 Change in T_1 of Benzoic Acid with Binding 114

4.16 Binding Curve of Benzoic Acid and β-Cyclodextrin 115

4.17 Hyperpolarized Naproxen 116

4.18 Compartmentation of Serine Synthesis 117

4.19 Reaction Scheme for Glycine Conversion by SHMT and Glycine Cleavage System 119

4.20 Hyperpolarized [1-^{13}C] Glycine 119

4.21 Reversible Mechansim of Creatine Kinase 120

4.22 Hyperpolarized [guanidino-^{13}C] Creatine 121

4.23 Enzymatic Scheme of Nicotinamide Metabolism 122

4.24 Reaction Scheme for Synthesis of [7-^{13}C] Nicotinamide 123

4.25 Hyperpolarized ^{31}P Spectra of Phosphoric Acid 125

4.26 Dynamic Copolarization of Pyruvate and Bicarbonate 132

4.27 *In vivo* Copolarization in a Normal Mouse 135

4.28 *In vivo* Copolarization in a TRAMP Mouse 136

4.29 Multi-compound polarization 137

Chapter 1: Introduction and Background

1.1 Motivation and Specific Aims of Project

Recent developments in low temperature physics and nuclear magnetic resonance (NMR) have allowed for the increase in signal intensity of conventional low gamma nuclei (i.e. ^{13}C) to be observed on the order of water (^{1}H). This technique, and adaptation of dynamic nuclear polarization (DNP), shows great promise for its clinical translation as well as its application to all facets of biological research. Changes observed as a result of hyperpolarized NMR can be applied not only to biological systems, but also chemical reactions, allowing drug design and development to be greatly accelerated. These designs need a testing bed that is reproducible and robust. For the last 3 decades, a great deal of research has been conducted in the field of bioreactor design, most of which has been geared toward application to biological systems. It is thus a logical progression to try to fuse hyperpolarized NMR with new NMR compatible bioreators in order to study [1-^{13}C]-pyruvate metabolism and to develop new hyperpolarized probes and techniques.

With this proposition in mind, the specific aims of this dissertation are:

A. Development and application of hyperpolarized carbon to a fluidized bioreactor
    i. Development of a fluidized bioreactor design which is applicable to the injection of hyperpolarized agents
    ii. Apply this bioreactor design to an immortalized hepatoma cell line (JM1 – rat hepatoma cells) and assess real time metabolism of [1-^{13}C]-pyruvate
    iii. Compare these results to steady state measurements of glycolytic metabolism by standard cellular extraction methods

B. Development of a new immobilized cartridge bioreactor and application of DNP NMR
    i. Design and Development of an immobilized NMR-compatible cartridge with potential for imaging
    ii. Application of this cartridge design to an immortalized prostate cancer cell line (PC3 – prostate adenocarcinoma cells)
    iii. Comparison of the observed metabolism to perfused prostate tissue slices and human biopsies from patients

C. New techniques and agents for DNP
    i. Design of new targeting methods including secondary labeling via acetic anhydride
    ii. Demonstration of hyperpolarization of non-conventional carbons, specifically hemiketals
    iii. Investigation of the effects of binding on hyperpolarized spins, specifically host ligand interactions
    iv. Development of new agents to probe other processes such as pH, bioenergetics, redox, apoptosis, perfusion and their combination in a multipolarization approach

The results of these specific aims will be a step toward the greater understanding of *in vivo* metabolism. Dynamic measurements made in a robust system can impact the development of clinically translatable agents as well as be surrogate biomarkers for the effects of future therapies and drugs.

1.2 Steady State and Non-Steady State Enzyme Kinetics

Generally the simplest rate equation in the context of biochemical enzyme kinetics, where one substrate is converted to one product, can be defined as:

$$E + S \underset{k_2}{\overset{k_1}{\rightleftarrows}} \left(ES \underset{k_4}{\overset{k_3}{\rightleftarrows}} EP \right) \underset{k_6}{\overset{k_5}{\rightleftarrows}} E + P \qquad [1.1]$$

Where E, S, and P represent the enzyme, substrate and product respectively. ES and EP are defined as the transition state enzyme-substrate and enzyme-product complexes. The rates k_n describe the velocity for each enzymatic process in a given direction. Disassociation constants K_S and K_P can be defined to produce a simplified enzymatic scheme:

$$E + S \xleftrightarrow{K_S} ES \underset{k_4}{\overset{k_3}{\rightleftarrows}} EP \xleftrightarrow{K_P} E + P \qquad [1.2]$$

Assuming the substrate and product are in fast equilibrium with the enzyme, the forward reaction (v_f) and reverse reaction (v_r) can be defined as:

$$v_f = \frac{dP}{dt} = \frac{k_3 E_0 S_0}{\left(K_S + S_0\right)} \qquad [1.3]$$

$$v_r = \frac{dS}{dt} = \frac{k_4 E_0 P_0}{\left(K_P + P_0\right)} \qquad [1.4]$$

Where S_0 and P_0 are the initial concentrations of substrate and product respectively. E_0 is the total enzyme concentration with reaction velocities k_n defined in [1.3,1.4]. It is important to define the difference between rate and flux. The rate (constant) k_n, is a unidirectional rate of change in time, for example k_3 in the above reaction. The net flux *J* can be defined as the difference between the overall forward and backward reactions.

$$J = v_f - v_r = \frac{E_0\left(k_3 S - \frac{k_4 K_S P}{P}\right)}{S + K_S\left(1 + \frac{P}{K_P}\right)} \qquad [1.5]$$

Note that k_3, k_4, K_S and K_P are related via the equilibrium constant of the reaction (K_{eq}) in terms of the Haldane relationship:

$$K_{eq} = \frac{k_3 K_P}{k_4 K_S} \qquad [1.6]$$

Incorporating the equilibrium constant into [1.5] for *J*:

$$J = \frac{k_3 E_0 S\left(1 - \frac{P}{S K_{eq}}\right)}{S + K_S\left(1 + \frac{P}{K_P}\right)} \qquad [1.7]$$

It follows that flux is a function of enzyme properties (K_m *and* V_{max}), but also E_0, *S* and the deviation of their ratio from equilibrium. The effect of thermodynamic disequilibrium is expressed as the term $1 - \frac{P}{SK_{eq}}$, with the sign determining reaction direction. These standard equations define the flux through a pathway, which can be extended to multiple pathways. This approach is the most basic set of assumptions applied to biochemical pathways.

Steady State and Non-Steady State Assumptions in Enzyme Kinetics

In an enzyme catalyzed reaction, steady state kinetics can be defined as the state when the concentrations of free enzyme (E_0), enzyme substrate complex (ES) and enzyme product complex (EP) change more slowly than the reactant concentration. For application to biochemically relevant systems, it is also assumed that equilibrium is established rapidly before the rate is measured as a result of instant mixing, generally referred to as the well-mixed assumption. Steady state is thus achieved when the reactant is also in excess of the enzyme concentration(Cook 2007). These conditions imply the following for steady state:

$$\frac{d[E_0]}{dt} = \frac{d[ES]}{dt} = \frac{d[EP]}{dt} = 0 \qquad [1.8]$$

$$S_t > E_t \Rightarrow \frac{dS}{dt} >> \frac{dE}{dt} \qquad [1.9]$$

$$S_{total} = S_{free} + ES \Rightarrow S_{total} \approx S_{free} \qquad [1.10]$$

Typically, steady state measurements are made as close to time zero as possible to limit the effect of substrate conversion to product and the final and initial concentrations of substrate are similar. This is important, because increases in product formation can lead to product inhibition and changes in substrate concentration can lead to substrate inhibition. Both effects can dramatically change the observed reaction velocity. In practice, rates measured where the substrate concentration has changed by less than 10% are usually considered initial rates. This is not the case in reversible reactions, which favor the substrate. In those cases rates are measured at 90% completion, or analogously when 10% of the reaction is left, because the catalysis is dominated by the backward component.

In the case of flux, at steady state, the rate of production of P is constant. However, if substrate is introduced at a high concentration, flux can be decreased as a result of substrate inhibition. This will change, as a function of the magnitude of disequilibrium, meaning this effect on flux will decrease as the ratio comes closer to the equilibrium ratio. Flux can also decrease if the substrate concentration is allowed to deplete or product is allowed to buildup (product inhibition). In the case of biochemical pathways *in vivo*, molecular mechanisms such as transport and enzymatic cascades maintain an intracellular concentration of both substrate and product such that the flux at each pathway (in steady state) does not change. Furthermore, at steady state, the only changes would be in the final end product of a given system, which is typically transported out of the cell.

Non-steady or unsteady state kinetics are generally defined as a state where both flux and concentrations are changing while the reaction is taking place. In the context of further explanation this can be applied to perfused systems where substrates are controlled and their utilization is specific. In this case, a two-state model is used where fluxes are measured when the overall state has changed. Since both flux and total concentration are varying in time, flux changes must be assessed in response to changing substrate/product concentrations. Due to the complexity associated with non-steady state kinetics, measurements of metabolic reactions in this *metabolic non-steady state* are generally reduced to steady state approximations.

Lactate dehydrogenase (LDH) kinetics

Lactate dehydrogenase (LDH) has been the focus of a great deal of recent scrutiny as a result of the interest in metabolism of hyperpolarized pyruvate (§1.3). In the late 1920s, Otto Warburg and coworkers(Warburg 1927) explored the metabolism of tumors and later describe a metabolic state(Warburg 1956) where tumor cells generate extensive amounts of lactic acid even in the presence of oxygen concentrations, which would warrant oxidative metabolism. This is counterintuitive given the generally accepted competitive advantage of a cell using primarily oxidative metabolism to produce energy (ATP). The Warburg Hypothesis has been the driving force for extensive research into the reasons why this occurs in cancer cells(Gatenby 2004; Costello 2005; DeBerardinis 2008), what the competitive advantage is(Gatenby 2004; Gillies 2007; Denko 2008; Ganapathy 2008) and how it can be used to target cancer as it develops and progresses(Gatenby 2007; Kroemer 2008).

At steady state, the kinetics of LDH can be viewed as an ordered bireactant kinetic scheme [1.11].

$$E \underset{k_2}{\overset{k_1 A}{\rightleftarrows}} EA \underset{k_4}{\overset{k_3 B}{\rightleftarrows}} EAB \Leftrightarrow EPQ \underset{k_6 P}{\overset{k_5}{\rightleftarrows}} EQ \underset{k_8 Q}{\overset{k_7}{\rightleftarrows}} E \qquad [1.11]$$

The enzyme (LDH, E) first binds the reduced dinucleotide cofactor nicotinamide adenine dinucleotide (NADH, A). It then binds the substrate (pyruvate, B) catalyzes the conversion from the enzyme-substrate-cofactor (EAB) to the enzyme-product-oxidized cofactor complex (EPQ). It then releases the product (lactate, P). The rate equation can be written in terms of a varying substrate concentration (here pyruvate) in [1.12].

$$\frac{1}{v} = \left(\frac{K_b}{VB}\right)\left[1 + \left(\frac{K_{ia}}{A}\right)\left(1 + \frac{Q}{K_{iq}}\right)\right] + \left(\frac{1}{V}\right)\left[1 + \left(\frac{K_a}{A}\right)\left(1 + \frac{Q}{K_{iq}}\right)\right] \qquad [1.12]$$

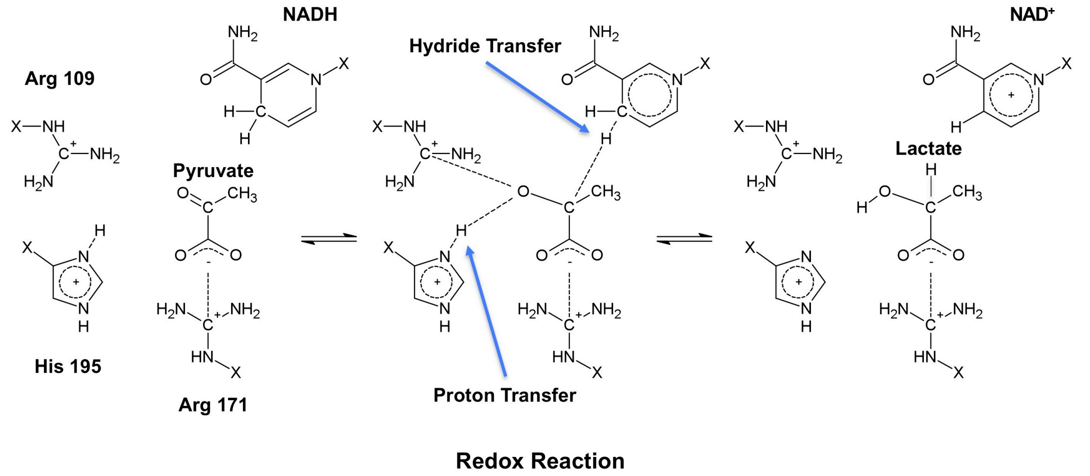

Figure 1.1: LDH enzymatic conversion of pyruvate to lactate. Amino acids are shown abbreviated with –X to simplify the scheme.

With K_a and K_b defined as the disassociation constants for the first two reaction steps and K_{ia} and K_{iq} defined as the disassociation constants for the EA ($\frac{k_2}{k_1}$) and EQ ($\frac{k_2}{k_1}$) complexes respectively. The enzymatic conversion of pyruvate to lactate can be diagramed as in **Figure 1.1**, with the relevant amino acids of the enzymatic pocket shown. As in the kinetic scheme [1.11], after recruiting NADH, pyruvate is shown stabilized by the enzyme complex and held to facilitate conversion to lactate. The restriction of the hyperpolarized probe that occurs in the enzyme complex can have a significant effect on the magnetic moment of a spin. This effect will be explained in later chapters, but this concept is of great importance to hyperpolarized carbon NMR and its ability to assess the enzymatic reactions.

It has been reported that at high concentrations of pyruvate, enolization can occur and enol-pyruvate (**Figure 1.2**) can interact with LDH creating an adduct(Burgner 1974; Burgner 1978; Wilton 1979). The adduct forms as a result of the oxidized cofactor being bound to LDH subsequently hindering the reaction rate at high concentrations of substrate. This phenomenon, as well as transport rates, availability of cofactor and substrate inhibition can all modulate the apparent flux through a pathway. Substrate inhibition of LDH by pyruvate has been shown *in vitro*(Wang 1977) and this has also been demonstrated in effluent collected from a perfused organ system(Strong 1979) where extracellular concentrations of pyruvate were varied. Strong and coworkers titrated pyruvate concentrations between 0 and 15mM and measured the lactate synthesis rate as shown in **Figure 1.3** (reprinted from Strong 1979). They postulated that the decrease in lactate production at high concentrations of pyruvate reflects either substrate inhibition of LDH or competition between lactate and pyruvate for the transport system. As a result of these kinetic properties it is necessary to take into account the substrate concentration and enzyme binding when interpreting velocity and flux data.

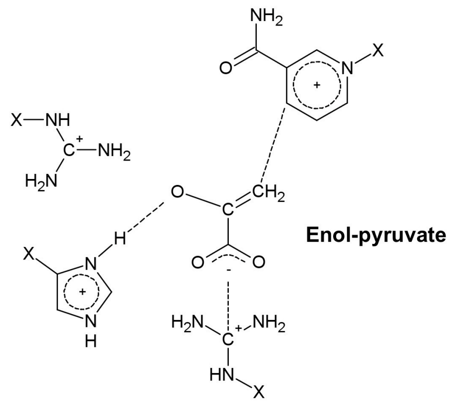

Formation of enol-pyruvate-adduct

Figure 1.2: Formation of enol-pyruvate-adduct in the LDH enzyme pocket. The reaction occurs with the NAD$^+$-enzyme complex (EQ).

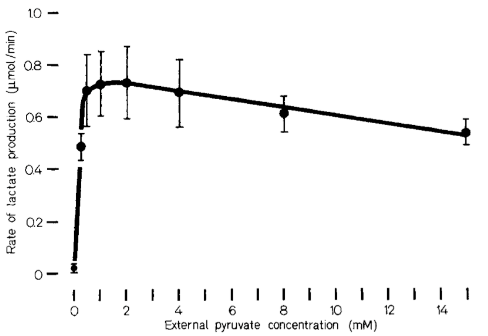

Figure 1.3: Reprinted from Strong et al. 1979. Titration of steady state lactate synthesis with external pyruvate. Hearts were equilibrated for 15min at 10kPa aortic pressure with 0.5mM octanoate as substrate before adding pyruvate to the perfusion buffer. Final pyruvate concentrations between 0 and 15mM were tested in randomized sequence, with a 5-min delay at each pyruvate concentration before collecting a 1-min sample of coronary effluent for lactate determination.

1.3 NMR Studies of Kinetics

NMR spectroscopy has been used to study both dynamic and static enzyme kinetics. Typically these studies have focused on detection of the ½ spin nuclei ^{1}H, ^{13}C and ^{31}P, because they are the most abundant nuclei found in metabolites. Each nucleus has its limitations and thus a combination of these is the standard approach to metabolic investigation.

^{1}H NMR spectroscopy is the most sensitive and traditionally most utilized technique for probing metabolism. Due to extensive overlap of metabolites in standard ^{1}H NMR, most approaches involve either observing dynamic changes with the addition of substrate or indirect detection of another probe via directly attached protons. Iorio and coworkers(Iorio 2005) have demonstrated a method for quantifying choline kinase activity using a dynamic ^{1}H spectroscopy method. Specifically, choline was added to cell extracts, in the presence of excess ATP and $MgCl_2$, and the resonance corresponding to the head group of phosphocholine (3.23 ppm) was observed over time. By comparing the signal area of the phosphocholine to choline peak as a function of time a rate constant was estimated. Similarly, steady state methods using ^{13}C labeled substrates can be used to investigate multiple pathways. Fan and coworkers(Lane 2007; Fan 2008; Fan 2008; Fan 2009) have demonstrated ^{1}H NMR spectroscopic methods that indirectly observe changes in ^{13}C labeling of glucose, lactate, alanine, and glutamate. These 1D and 2D methods provide a steady state distribution of label and give relative isotopomer distributions and take advantage of the sensitivity of protons.

^{31}P NMR spectroscopy, though less sensitive than ^{1}H, has also been used to measure metabolic kinetics. A recent example of this technique is that of Gabellieri et al(Gabellieri 2009), in which choline conversion to phosphocholine was observed dynamically via production of the phosphocholine resonance, which was used to calculate choline kinase activity. This approach was extended to study competitive inhibitors of choline kinase and demonstrated the power of ^{31}P as a technique for observing metabolic kinetics with very little spectral overlap, in comparison to ^{1}H.

Possibly the most interesting nuclei for studying metabolically related mechanisms has been ^{13}C. Though sensitivity and natural abundance have been limitations to the application of ^{13}C NMR spectroscopy, many studies have been conducted using perfused ^{13}C-labeled substrates. Direct observation of steady state ^{13}C NMR has been applied to perfused organs, specifically heart and liver(Jucker 1998; Lu 2002; Burgess 2003) to determine distribution of fluxes, specifically TCA and glycolytic flux. Dynamic ^{13}C NMR spectroscopy has has been used to study enzymatic processes both *in vivo*(Shulman 1985; Sibson 1997; Macdonald 2002; De Graaf 2003; Gruetter 2003; Thelwall 2005; Lei 2007; Mason 2007) and in engineered bioreactor systems(Gamcsik 1999; Gamcsik 2004; DeBerardinis 2007). Typically the enzymatic processes that have been studied by Dynamic ^{13}C NMR spectroscopy have long turn over rates (on the order of 12 hours). The low sensitivity of ^{13}C NMR, and resulting low temporal resolution, prohibits the direct assessment of fast enzymatic reactions. This major limitation can be addressed by in the dramatic increase in signal provided by hyperpolarized NMR (§1.4).

1.4 DNP Physics: Solid State Effect and Hyperpolarization

It is well known that ^{13}C NMR spectroscopy (as well as other insensitive nuclei) has been limited in its ability to characterize metabolic states due to its low sensitivity. This low sensitivity is a result of the low natural abundance of ^{13}C (1.1%) in addition to the low gyromagnetic ratio of carbon (6.728284 x 10^7 rad/T s). These characteristics reduce the overall sensitivity of ^{13}C nearly 4 orders of magnitude in comparison to ^{1}H NMR (6400 fold without NOE or INEPT, 1600 fold if INEPT is included) and even more impressively for ^{15}N (up to 270,000 fold). Traditionally, the low nuclear polarization and low natural abundance of carbon was addressed by using high concentrations of ^{13}C-enriched substrates for metabolic studies. Depending on the nucleus, direct detection methods require hours to days to record spectra with sufficient signal to noise for analysis.

With this difficulty in mind, a number of techniques have been proposed to increase the polarization of nuclear spins to overcome their low gyromagnetic ratios. In addition to enrichment, indirect detection methods have been widely practiced, but these require a convenient scalar coupled proton. Newer methods that provide a much greater sensitivity enhancement have recently been developed. These methods of hyperpolarization include: para-hydrogen-induced polarization (PHIP) (Golman 2001), optical pumping(Goodson 2002) and dynamic nuclear polarization (DNP) (Ardenkjaer-Larsen 2003; Golman 2003). Each of these methods has the potential to generate a 100% nonthermal polarization of the chosen ½ spin nucleus. PHIP, also known as PASADENA(Bowers 1987; Canet 2006) and ALTADENA(Pravica 1998), relies on the introduction of a para-hydrogen substrate through catalytic hydrogenation. Though this method has been shown to be successful(Goldman 2005) it is only applicable to reactions involving substrates with double and triple bonds. Optical pumping utilizes circularly polarized laser light and has been successfully applied to the hyperpolarization of ^{3}He and ^{129}Xe gases (Goodson 2002). This method is restricted to a subset of the noble gases and has limited application to the study of metabolism. The final method, DNP, is based on the polarization of nuclear spins in an amorphous solid state at ~1°K through coupling of the nuclear spins and unpaired electrons via an organic free radical. Recent advances in the field of low temperature physics, electronic paramagnetic resonance (EPR) and NMR have provided for the adaptation of the DNP technique, described as early as the 1950s(Abragam 1958), to the study of metabolism both *ex vivo* and *in vivo*(Chen 2007; Kohler 2007; Merritt 2007). Due to its applicability, the purpose of this section is to describe this emerging technique of hyperpolarization and its application to the investigation of metabolic systems.

Solid State Effect and Hyperpolarization

Conceptually, what we consider dynamic nuclear polarization (DNP) is an extension of what has been previously described as the "solid state effect"(Abragam 1958). In the early 1950s, Overhauser postulated that an NMR signal could be increased as a result of the interaction between a nucleus and the electrons of a metal(Overhauser 1953). This principle was later applied to non-metals by Abragam et al. (Abragam 1955) and in 1974(de Boer 1974) demonstrated that through thermal contact between nuclear and electronic spins, dynamic nuclear polarization can be produced(de Boer 1974).

To investigate the underlying physics of the solid state effect, first consider a set of nuclear spins *I* embedded in a solid containing a small percentage of paramagnetic impurities with spins *S*. These spins are of ½ and have Larmor frequencies ω_I and ω_S. For a given spin, the spin density where all magnetization is along the z-axis corresponds to the equilibrium among states governed by the Boltzmann distribution. A spin $I = \frac{1}{2}$ can be characterized by two states $|\alpha\rangle$ and $|\beta\rangle$. The probability of finding a spin in each of the states is then proportional to:

$$P_\alpha \propto e^{\frac{-E_\alpha}{kT}} \approx 1 - \frac{E_\alpha}{kT},\ E_\alpha = \frac{-\hbar\gamma_I B_0}{2} \qquad [1.13]$$

$$P_\beta \propto e^{\frac{-E_\beta}{kT}} \approx 1 - \frac{E_\beta}{kT},\ E_\beta = \frac{\hbar\gamma_I B_0}{2} \qquad [1.14]$$

The overall spin polarization of this system is the population difference between the $|\alpha\rangle$ and $|\beta\rangle$ states. This population difference or percent polarization is demonstrated in **Figure 1.4** for electron, proton and carbon spins with respect to temperature.

At low temperatures (on the order of 1°K) in a strong magnetic field, the electron polarization is near unity while other nuclei are not, yielding a distribution of uniformly oriented spins *S* and disoriented spins *I* (**Figure 1.5**). These spins *I* and *S* are coupled through dipolar interactions and this permits the simultaneous reversal of these spins in the same direction (producing two "up" spins) or opposite directions (producing one spin "up" and one spin "down") if the spins were originally anti-parallel. These spin "flips", which require energy $h(\omega_S \pm \omega_I)$ to occur, are analogous to the spin-lattice relaxation mechanism (T_1 spin relaxation). At low temperatures, the time of this "flip" process for the target nucleus *I* is on the order of 10^3 s, while it is 10^{-3} s for a lone electron spin *S*, as a result of its coupling to the lattice. By providing energy *via* a laser with frequency $\Omega = \omega_S \pm \omega_I$, these flips can be induced and because the order of electron relaxation is much faster than that of the target nucleus, the spins *S* will bring all of the spins *I* to their "up" position. It has been

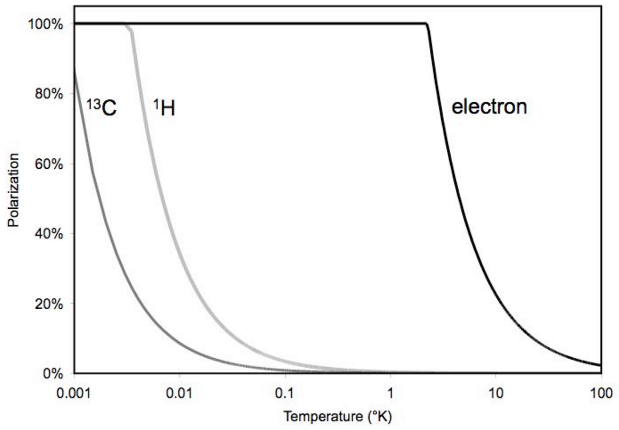

Figure 1.4: Above is a plot of the percent polarization as a function of temperature for each indicated spin. These were derived using equation 12 at a magnetic field strength of 3.35 T.

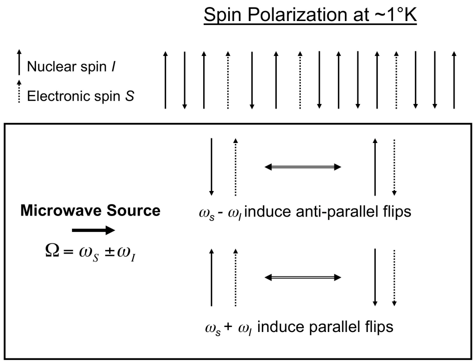

Figure 1.5: A graphical representation of spin polarization of the nuclear spin *I* and electron spin *S* is shown. After exposure to an RF signal at frequency $\Omega = \omega_S \pm \omega_I$ the induced flips are shown.

shown(Abragam 1978) that the case of anti-parallel flips is impossible leading to the association of spin change with $\Omega = \omega_S + \omega_I$. When all of the I spins are in their "up" position, the target material can be deemed hyperpolarized.

It follows that for a low electronic concentration; each spin *S* must "flip" many nuclear spins. For this to occur, it has been shown that the following condition is required(Abragam 1978):

$$f = \left(\frac{N_I}{T_n}\right)\left(\frac{N_S}{T_e}\right)^{-1} << 1 \qquad [1.15]$$

Where N_I and N_S are the number of respective spins and T_n and T_e are the respective longitudinal relaxation times. With this dipolar coupling as the only means of relaxation, it is assumed that the polarization P_n of the nuclei would reach unity (i.e. that of the electron spins). Due to other mechanisms, such as leakage relaxation as a result of coupling with another species or saturation by microwaves of frequency ω_S, this nuclear polarization can be much less than P_e (Abragam 1978). In practice, de Boer et al. were able to increase the polarization of natural abundance ^{13}C to ~46% in a complex of 1,1,2,2-ethanediol-$(CD_2OH)_2$ and Cr^V(de Boer 1974). Recently, Ardenkjaer-Larsen et al. have shown a method of DNP polarization utilizing a labeled compound at liquid helium temperatures with the introduction of an organic free radical. These studies have shown polarizations of 37% for ^{13}C and 7.8% for ^{15}N, corresponding to a 44,400 and 23,500 fold enhancement over the equilibrium room temperature polarizations, respectively, when the hyperpolarized sample is brought to a liquid at room temperature(Ardenkjaer-Larsen 2003). It should be pointed out, and as shown in **Figure 1.4** that at liquid helium temperatures (i.e., 1°K) there is a significant increase in the equilibrium polarization of approximately 300-fold over room temperature (310°K).

Hardware and Pulse Sequences

Aside from the traditional NMR spectrometer, DNP-NMR requires the addition of a unit composed of multiple components collectively termed a “polarizer”. The key components of this DNP system are as follows: polarizing magnet, microwave source, variable temperature insert (VTI), sample holder, dissolution system, control electronics and solid-state NMR monitor (polarimeter). These elements work in concert to take a sample from its native spin polarization state at room temperature to a highly polarized state at room temperature by way of polarization at liquid helium temperatures.

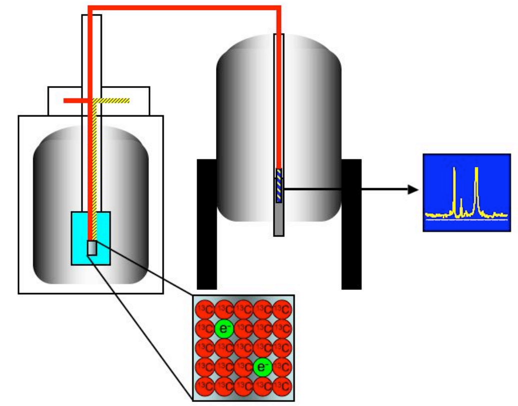

Figure 1.6: A graphical representation of the DNP polarizer (left) and high-field NMR system (center). The red line indicates the flow of the sample after hyperpolarization. The yellow line represents the microwave source and its irradiation of the sample chamber. The sample chamber houses the amorphous solid at ~ 1.2°K. After polarization the sample is observed in the NMR spectrometer.

Figure 1.6 demonstrates a graphical representation of the polarizer and an adjoining high field magnet. The method described here is analogous to the method described by Ardenkjaer-Larsen et al(Ardenkjaer-Larsen 2003) though there are other methods of generating DNP(Bowers 1987; Golman 2001). A concentrated mixture of ^{13}C labeled substrate is mixed with an organic free radical and placed inside of the sample holder. This sample holder is then lowered into the VTI to the center of the magnet. The sample chamber is filled with liquid helium from the magnet dewar and vacuum pumped to a vapor pressure of ~0.8 mbar, resulting in a temperature of ~1.2°K. The sample is then irradiated for typically 60 minutes at the microwave frequency associated with the free radical (on the order of 94 GHz). As the electron spins polarize the nuclear spins, the polarimeter monitors the percent polarization. Once the solid-state sample has reached maximum polarization, it is mixed with a super heated buffer (450°K, 10 bar) through the dissolution system. This process takes less than 2-3 seconds and brings the sample to room temperature while still preserving the low-temperature nuclear polarization(Ardenkjaer-Larsen 2003). The sample is then injected into the medium of interest and observed in a conventional MRI or NMR spectrometer. Control electronics allow for this process of dissolution and injection to be on the order of seconds. At physiological temperatures, the T_1 of pyruvate carboxyl carbon is on the order 40 to 60 secs, depending on the magnetic field strength used, which implies that the initial polarization in the animal is very close to that at the end of the polarization in the microwave polarizer. The effective experimental time available is around 5 T_1 or ca. 200 secs, when the sensitivity has decreased to <1% of its initial value (and see below). Observed magnetization changes can be corrected for the exponential magnetization loss due to relaxation.

Due to the limited lifetime of the polarized substrate, which is proportional to the T_1 relaxation, fast pulse sequences must be implemented *in vivo* and *ex vivo* to capture substrate uptake and metabolism in real time. For both *ex vivo* spectroscopy and *in vivo* single voxel spectroscopic imaging, the task is fairly simple. Generally, a standard direct detect one-dimensional carbon sequence is used with a very small flip angle (on the order of 5-15°) and a single acquisition. The use of a low flip angle allows the bulk polarization to be preserved in the I_z vector. A 10° flip angle preserves 98% of the magnetization along z, and the x component is 17% of the equilibrium value. This allows for multiple scans to be taken as the substrate is metabolized. Recent studies have shown the effectiveness of small flip angles in hyperpolarized tissue culture experiments, with ^{13}C signals lasting for minutes of continuous pulsing(Day 2007; Merritt 2007; Keshari 2008). This procedure has also been adapted for *in vivo* single voxel spectroscopy in rat(Kohler 2007) and mouse models(Goldman 2005; Chen 2007; Albers 2008) to explore changes in metabolic kinetics. Pulse sequences have been developed for the probing of polarization transfer experiments as a result of the hyperpolarized substrate(Frydman 2007) as well as the measurement of polarization through dipolar coupling(Merritt 2007). DNP-NMR has also been applied to spectroscopic imaging of pre-clinical animal models(Day 2007; Albers 2008). Magnetic Resonance spectroscopic imaging of hyperpolarized probes required the development of fast pulse sequences and sampling techniques to acquire spectrally and spatially resolved data within the time-frame of the DNP experiment (≈ 5 T1's of the labeled probe). Different k-space sampling techniques have been utilized to reduce scan time, including centric(Chen 2007), ellipsoid(Reeder 2007), and spiral(Levin 2007). This in addition to adiabatic refocused double spin echo sequences(Cunningham 2008) and echo planar fly back encoding allow for the acquisition of a 8 x 8 x 16 MRSI matrix with 0.135 cc spatial resolution in under 14 secs(Chen 2007; Chen 2007). Least squares chemical shift imaging has also been applied, using a priori knowledge of the resonances of interest, to further reduce the number of necessary data points acquired (Reeder 2007).

1.5 Current developments in NMR compatible bioreactor culture systems

The purpose of this section is to give a brief overview of the state of the art as it pertains to bioreactor designs. These have been implemented to study immobilized cells in side of an NMR magnet and monitor their changes. Each design has its benefits and disadvantages, which were considered in the designs that are discussed in future chapters (§2 and 3).

Hydrogel threads, Sponges and Beads

The most common technique for cell immobilization in NMR-compatible bioreactors has been stabilization of cells via a hydrogel. These hydrogel constructs have been used to create an environment similar to an *in vivo* 3D structure so as to allow cells to be perfused by recirculating medium. Hydrogel designs can be broken up into 3 major constructs: Gel Threads, Sponges and Encapsulates.

Gel threads or filaments, are constructed of Agarose, a temperature sensitive polysaccharide isolated from seaweed. It has been used to study many cell types including Sertoli cells(Farghali 1996), lymphocytes(Lyon 1986), hepatocytes(Farghali 1992), and erythrocytes(Lundberg 1994). Threads are made by suspending cells in a liquid agarose solution. The mixture is then extruded through tubing into long filaments, the diameter of which determines the filament diameter. As the filaments form, the agarose cools forming a semi-rigid gel. Filaments are then perfused in side of an NMR tube, generally a 10mm, and observed in time. Agarose filaments can support a total number of cells in the spectrometer sensitive volume on the order of 10^8 cells(Kaplan 1994), which can potentially produce ^{31}P spectra with 10min temporal resolution, depending on cell type. At this high cell density, experiments can be carried out for short periods (1-2 days).

Agarose has also been extended to production of agarose beads(Ronen 1989; Bental 1990; Ronen 1990). These tend to be made similar to the filaments, except that the agarose-cell mixtures are dropped into vortexed mineral oil. Due to lack of fine control, bead diameters tend to be varied (0.3-3mm) as a function of vortex and infusion rate. Another inherent limitation of agarose is its inapplicability to anchorage dependent cell types. Agarose is a good immobilization medium for suspension cells and those with minimal surface-attachment requirements, such as erythrocytes(Lundberg 1994), but for other cell types agarose beads can result in the cells being in a non-proliferating state(Daly 1988). To work around this issue, Matrigel® has been used as replacement construct. Isolated from cancer cells, Matrigel® has been used to grow cells for periods of longer than a week (Daly 1988). Unfortunately, Matrigel® is not completely defined and complications arise from the influence of the mixture itself on the metabolism of cells of interest. It is also expensive and can lead to hindered diffusion of large macromolecules.

Collagen sponges have also been used as a gel construct for the support of cells. Typically cells are grown in the collagen sponge for a period of weeks(Gamcsik 2004) and these are monitored prior to perfusion in a bioreactor system. Collagen, typically type-1, is utilized because it is a natural occurring extracellular matrix constituent. In comparison to Matrigel®, type-1 collagen is assumed to have no cancer related signaling and induces differentiation(Macdonald 2001) and is thus a less confounding mode of immobilization for both benign and malignant cells. Difficulties arise from collagen sponges, in that they are hard to perfuse. Typically sponges are 1cm cubes, which limits the diffusion distance necessary for supporting high-density cell cultures. This leads to less dense cell cultures (~10^7 cells), which can make NMR acquisition times long and limit temporal resolution.

The third major hydrogel type is alginate encapsulation. In this scheme, typically mammalian cells are entrapped in calcium alginate beads and perfused similar to the previously mentioned filaments and sponges. This method has been used to study lymphocytes(Kaplan 1991), hepatocytes(Murtas 2005; Chandrasekaran 2006), prostate cancer cells(Narayan 1990; Macdonald 1993), pancreatic cells(Constantinidis 2006) and many other cell types. These encapsulates can also be coated with immunosuppressant compounds to facilitate implantation in the case of beta islets(King 2000) and hepatocytes(Weber 2009). Encapsulates are made by suspending cells in an alginate mixture, similar to the agarose derived constructs. This solution is then pushed through a small tube (diameter of catheter) at a constant rate to create uniform droplets. Analogous to an inkjet printer, droplet sizes are controlled by a voltage gap created inside the catheter via a strong voltage source. The droplets then fall into a high calcium bath (110-150mM) to allow the beads to calcify(Mørch 2006). These solid beads are then quickly removed from the calcium bath and resuspended in media. If coating is required, layers of poly-lysine or chitosan(Serp 2000) can be applied to further stabilize the beads.

Alignate encapsulates are superior to gel threads and sponges for maintenance of high-density cultures as a result of the high surface area to volume ratio of the spheres. Assuming a maximum oxygen diffusion distance of 0.25mm, a 0.5mm sphere can provide for a construct that far surpasses a 1cm cube or a 0.5mm diameter thread in creating an environment for cellular growth. Due to the high density, perfusion media must be re-oxygenated at a high rate to provide the adequate oxygen tension to support the cells. This requirement can be facilitated by an artifical lung gas exchanger(Gillies 1993; Gamcsik 1996), which can oxygenate media based on fundamental gas properties.

Hollow Fibers

Hollow fiber (HF) bioreactors have been developed over the last 20 years as a platform for study as MR compatible systems, but also for high throughput manufacturing of proteins and artificial organ systems such as the liver. HF designs have also been implemented in high volume filtration systems for industrial water purification(Busch 2007) due to their high efficiency. Conventional HF bioreactor designs consist of hollow fiber bundles(Mancuso 1990; Gillies 1993), which separate the region of interest into two compartments: cell mass and media (effluent). Typically cell mixtures are loaded into the inner portion of a fiber and media is perfused in the space surrounding the fibers. The HF diffusion distance is then a function of the fiber diameter, which is usually limited to less than 1mm for this reason. More recently, coaxial HF bioreactors have been designed which increase the viability of cells by creating a third compartment inside of the cell mixture compartment(Macdonald 1998; Wolfe 2002). This fiber within a fiber design dramatically increases mass transfer of nutrients (potentially 4 fold) and can be compared in design to the structure of the liver acinus. Oxygen diffusion models have shown appropriate levels of oxygen concentration through various distances in the HF bioreactor(McClelland 2003) and these will limit the regions of anoxia that can greatly inhibit the efficiency of a biroeactor(Gasbarrini 1992). The HF bioreactor designs though are limited in their application to high-resolution NMR systems due to the size requirements of the construct. HFs take up a lot of space inside the RF coil, thus limiting the global cell density in sensitive volume of the NMR probe, and perfusion designs have also required many ports which can not be placed inside of a standard NMR probe. High flow rates are also required to induce Starling Flow and limit radial gradients(Heath 1990). Future designs that are controlled in a 1-way fashion may overcome these limitations.

Microcarriers

The last group of immobilization constructs is Microcarriers. These are typically spheres both porous and non-porous. Non-porous carriers act as support structures that cells can grown on, which are typically collagen-coated to allow for anchorage dependent cells to grow. These have been applied to many cell types including prostate cancer cells(Pilatus 1997), fibroblasts(Galons 1995), breast cancer cells(Mancuso 2004) and glioma cells(Mancuso 2005). Similar to alginate beads, non-porous microcarriers can be perfused in a packed-bed design. The advantage of these non-porous microcarriers is that they have a very limited diffusion distance since there is between 1-3 layers of cells on the outside of a carrier. These microcarriers are limited in that: the effects of high flow rates can cause shear forces to act on these cells, the growing cells can decrease the inter-sphere space thus causing channeling over time, and most importantly the bead center is wasted as a result of no cells and this limits the global cell density within the sensitive volume of the NMR probe, resulting in decreased signal intensity. Cell densities can be on the order of previously described experiments (10^7 cells), though they are continuously subject to shear force. Porous microcarriers are applied in a similar fashion to the non-porous version, though they suffer from compressibility problems as a result of the loss in rigidity. Typically they require slow flow rates, which in turn limits the ability to maintain high cell densities inside of an NMR. It has been successfully applied in a packed-bed design(Mancuso 2005) with a total of 10^8 glioma cells, though not for extended periods of time. Also, collagen microcarriers are used in hollow fiber bioreactors (Gillies 1993) (Gillies 1991). The cells are first attached to the microcarrier and then the mass is inoculated into the bioreactor. The use of degradable collagen microcarriers helps anchorage-dependent transformed cell lines to expand while reducing attachment to the hollow fiber, which cause fiber fouling and clogging of fiber pores.

Chapter 2: Fluidized Bioreactor and Hyperpolarized NMR

2.1 Design of Fluidized Bioreactor system and Methods

There is growing interest in the changes in fluxes through a variety of metabolic pathways associated with the evolution and progression of cancer(Gatenby 2007; Christofk 2008; DeBerardinis 2008; Fan 2008; Hsu 2008; Munger 2008; Tessem 2008) and its response to therapy. More recently dynamic nuclear polarization, (DNP) spectroscopic techniques have been used to study these metabolic fluxes in real-time(Day 2007; Albers 2008). Focus has been placed on changes in pathways associated with lipid synthesis and degradation(Ackerstaff 2003; Iorio 2005), bioenergetics(Kurhanewicz 1992; Bonarius 2001), and redox potential(Gillies 1994; Thelwall 2005). Increases in lactate dehydrogenase (LDH) activity(Day 2007; Albers 2008), changes in glutaminolysis(DeBerardinis 2007), and decreases in pyruvate kinase activity(Christofk 2008) have been associated with cancer. These studies have been conducted primarily in extracts of cell cultures(Fan 2008) or by way of *in vivo* animal studies(Jucker 1998; Macdonald 2002; van Zijl 2007). Cell culture studies provide a controlled platform for long-term metabolic studies, but they are tedious since each measurement requires new cells. In contrast, in *in vivo* studies the same animal can be used for multiple metabolic measurements but they are more costly, biologically heterogeneous, require many animals to be sacrificed and inefficient for the initial screening of novel metabolic tracers.

For the last three decades, cell perfusion or "bioreactor" systems have been developed in an attempt to address these fundamental issues(Mancuso 1990; Gillies 1994; Wolfe 2002). These 3D culture perfusion systems have allowed the monitoring of steady state metabolites and their changes with time(Farghali 1996; Mancuso 2005), typically through the analysis of output parameters such as concentrations of lactate, glucose and alanine in media(Bailey 1998). Studies have also been performed in order to assess slow metabolic processes, such as phospholipid(Beloueche-Babari 2006), glutathione(Gamcsik 2004), and glutamine metabolism(DeBerardinis 2007), but these systems do not have the temporal resolution to study fast kinetic reactions.

Due to the dynamic nature of cellular metabolism and its instantaneous response to changing stimuli (environmental, genetic, etc…) the study of flux through pathways, now dubbed "fluxomics", has become a rapidly expanding area of research in metabolomics(Massou 2007; Droste 2008). An inherent problem associated with determining real time fluxes is the speed of some metabolic reactions. Enzymes of clinical interest, such as LDH (lactate dehyrdogenase), have been measured to have relatively high velocities(Chowdhury 2005) and thus measurement of flux through LDH in a living system is difficult. While glucose conversion to lactate by ^{13}C NMR has been achieved, it has involved, long glucose infusion periods relative to the rates of the reactions in tissues of interest(van der Zijden 2008). A great deal of work has been done determining steady state metabolite concentrations and inferring metabolic flux by mass spectrometry(Miccheli 2006), NMR(Burgess 2003) and spectrophotometry(Stephanopoulos 2001). However, these traditional methods require the system to be quenched and extracted for each time point necessary to calculate flux. NMR spectroscopy is a research tool that can be readily translated to the clinic. ^{13}C NMR spectroscopy provides high spectral resolution and has been used to study metabolic fluxes in a variety of systems(Lane 2007). The major shortcoming of ^{13}C NMR spectroscopy is its lack of sensitivity, due to a low gyromagnetic ratio (γ), resulting in the inability to measure flux with high spatial and temporal resolution. This major hindrance has been recently overcome through the development of dynamic nuclear polarization (DNP) NMR spectroscopy(Ardenkjaer-Larsen 2003). ^{13}C labeled substrates have been recently polarized using DNP techniques to obtain tens of thousands fold enhancement of ^{13}C NMR signals of the substrate and it's metabolic products, enabling measurement of rapid metabolic fluxes such as those catalyzed by LDH and ALT (alanine aminotransaminase).

Recent studies of hyperpolarized ^{13}C labeled compounds, by way of the DNP method(Chen 2007; Day 2007; Albers 2008), have been used to investigate metabolic processes associated with increases in aerobic glycolysis, deemed the Warburg effect(Warburg 1927; Warburg 1956). The Warburg intermediates (elevated lactate, alanine and pyruvate) have been used as a way to characterize cancer aggressiveness(Albers 2008) and response to therapy(Day 2007). In this series of studies, JM1 (immortalized rat hepatoma) cells were cultured in a 3D NMR-compatible bioreactor, and injections of hyperpolarized [1-^{13}C] pyruvate were used to serially measure LDH and ALT fluxes in real-time.

Cell Culture and Bioreactor

JM1 rat hepatoma cells (Michalopoulos Lab, University of Pittsburg) were cultured in DMEM medium (Invitrogen, 3g/L glucose) supplemented with 10% fetal calf serum, 100 units/mL penicillin and 100 μg/mL streptomycin (Invitrogen). Cells were grown in T150-flasks (Fisher) to incubated at 37°C in a 95% air/5% CO_2 incubator. For 2D culture extract experiments, cells were plated on 150cm^2 collagen coated plates (Fisher Scientific) and grown to less than 90% confluency (12.6 x 10^6 cells). Media was changed for each plate and replaced with analogous media supplemented with uniformly labeled ^{13}C-glucose (u-^{13}C glucose). Plates were allowed to progress for 23 hr (n = 4). At each time point an aliquot of media was collected, plates were washed twice with ice-cold PBS and extracted in ice-cold methanol as previously described(Maharjan 2003). Residual pellets were also extracted in deuterated choloroform to assess the labeling of lipids(Tyagi 1996). Fractional enrichment (FE) was defined as the percent of ^{13}C labeled compound relative to the total pool.

For bioreactor experiments, cells were trypsinized, washed in PBS and electrostatically encapsulated at a concentrations of 25 (n=1), 50 (n=2) and 127 x 10^6 (n=1) cells/mL in 500μm beads as previously described(Chandrasekaran 2006). Approximately 1.5mL of encapsulates were perfused using the same media formulation as above, re-circulated at a rate of 4mL/min. The bioreactor loop contains 40 mL in circulation. Media was kept at a constant 37°C by way of water-jacketed lines and gas pressures were maintained by a Gas Exchange Module (GEM) using 95% air/5% CO_2 gas as previously described(Gamcsik 1996). A schematic of the bioreactor system is shown in **Figure 2.1** (for further descriptions of the bioreactor see **Appendix A**). Encapsulates were removed at the end of the experiment, embedded in optimal cutting temperature (OCT) and stained with hematoxylin and eosin (H&E) as previously described(Tessem 2008) to confirm cells were greater than 90% viable.

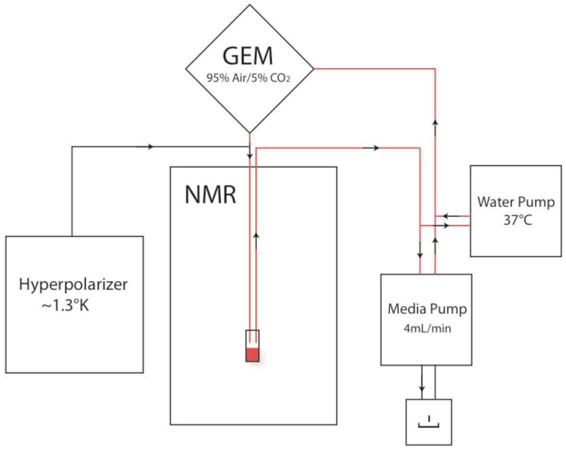

Figure 2.1: Schematic of bioreactor setup. The red line indicates the flow of media as it recirculates in the bioreactor. GEM – gas exchange module

Hyperpolarization Methods

[1-^{13}C]-pyruvate was hyperpolarized by the DNP method(Ardenkjaer-Larsen 2003) using the Hypersense® (Oxford Instruments) to an average polarization of ~15%. The compound polarized was a mixture of [1-^{13}C] -pyruvic acid (14.2M) and the trityl radical (15mM, Tris[8-carboxyl-2,2,6,6-tetra[2-(1-hydroxyethyl)]-benzo(1, 2-d:4,5-d)bis(1,3)dithiole-4-yl]methyl sodium salt) (General Electric Medical). Samples were dissolved in a dissolution solution containing $NaPO_4$ (50mM)/EDTA (0.3mM) to bring the sample to the desired concentration and average pH of 7.5. A solution of 1mL of the hyperpolarized pyruvate was injected into the bioreactor system with continuous flow, resulting in a final concentration of between 2-14mM pyruvate. Higher concentrations were used in bioreactors, which contained a higher cell concentration. This was done to keep the same relative substrate concentration throughout the group of bioreactors. The bioreactor is water jacked and there were no observed temperature changes in the cell mass during the studies. These concentrations were kept constant relative to the encapsulated cell concentration, allowing the cell suspension to see an analogous influx of mass of pyruvate at each injection.

NMR Acquisition and Analysis

Cell extract samples were placed in a Speed-Vac® for 8 hours to evaporate the methanol. Cell pellets were then reconstituted in 100% D_2O (with 2.5mM TSP for quantification). Media aliquots were supplemented with 10% D_2O (and a final concentration of 2.5mM TSP). ^{1}H and 2D ^{1}H-^{1}H TOCSY (total correlation spectroscopy) spectra were acquired at 16.4T Varian INOVA (700MHz ^{1}H, Varian Instruments) equipped with 5mm ^{1}H/^{13}C indirect probe at 25°C. ^{1}H spectra of extracts were acquired using a total repetition time (TR) of 12.65s, number of transients (nt) of 64 and a 90° flip angle. Data were analyzed using ACD Labs 9.0 1D NMR Processor (ACD Labs). ^{1}H spectra were zero-filled to 32,000 points, line broadened 0.5Hz using an exponential Gaussian function. Peaks and ^{13}C satellites corresponding to glucose, lactate, alanine, glutamate, and the nucleotide spin systems of the purines and pyrimidines (AXP+GXP, UXP+CXP) were peak fit and quantified relative to TSP in ACD as previously described(Lane 2007; Swanson 2008).

2D TOCSY data were acquired with TR=2.48s, nt=16, and number of indirect dimension increments (ni) of 64. Data was linear predicted in 3 x N in the indirect dimension and zero-filled to 2,000 points. The data was 2D Fourier Transformed and cross-peaks corresponding to unlabeled and ^{13}C labeled lactate, alanine, glutamate, and the ribose of nucleotides were volume integrated as previously described(Lane 2007). These points were then used to calculate fractional enrichment as the sum of the of center cross-peaks to the total volume. The peak areas from the 1D ^{1}H and volumes from the 2D ^{1}H-^{1}H TOCSY were used to calculate the absolute number of mmols of each compound that were generated as a result of u-^{13}C-glucose metabolism.

For bioreactor studies, ^{13}C and ^{31}P spectra were acquired on an 11.7T Varian INOVA (125MHz ^{13}C and 202MHz ^{31}P, Varian Instruments) equipped with a 10mm triple-tune direct detect broadband probe at 37°C. ^{31}P time courses were acquired before and after hyperpolarized injections using a TR=3s, nt=1024 and a 90° flip angle. ^{31}P spectra were zero filled to 40,000 points and line broadened 15Hz. Assessment of changes in the βNTP resonances as a function of time was used to monitor cell health through the progression of the bioreactor experiments *in vivo*. Hyperpolarized ^{13}C experiments were acquired using a 5° flip angle, TR=3s and acquired for 300s. Data were zero-filled to 16,000 points and line-broadened 5Hz. The resonances of pyruvate (171 ppm), lactate (182 ppm) and alanine (175 ppm) were integrated and compared as a function of time to determine the characteristics of enzymatic interconversion as a result of pyruvate injections. Fluxes were determined using a model of LDH and ALT labeling flux implemented in Interactive Data Language (IDL, ITT Visual Information Solutions, Boulder, CO) normalized for injected hyperpolarized pyruvate concentration and cell concentration estimated from relative changes in βNTP peak area. Briefly, the pyruvate peak area over time (M_p) was modeled to determine the arrival time (t_a), rate of injection (k_i) and signal decay of pyruvate (k_p).

$$M_p(t) = \begin{cases} \frac{k_i}{k_p}\left(1 - e^{-k_p(t-t_a)}\right) & \forall t_a \le t < t_e \\ M_p(t_e)e^{-k_p(t-t_e)} & \forall t \ge t_e \end{cases} \qquad [2.1]$$

The t_e represents the end of the pyruvate injection time. These fitted parameters were then used to fit the ^{13}C lactate and alanine data to estimate LDH and ALT labeling fluxes (k_{px}) where x represents either lactate or alanine [2.2].

$$M_p(t) = \begin{cases} \dfrac{k_{px}k_i}{k_p - k_x}\left(\dfrac{1-e^{-k_x(t-t_a)}}{k_x} - \dfrac{1-e^{-k_p(t-t_a)}}{k_p}\right) & \forall t_a \le t < t_e \\ \dfrac{M_p(t_e)k_{px}}{k_p - k_x}\left(e^{-k_x(t-t_e)} - e^{-k_p(t-t_e)}\right) + M_x(t_e)e^{-k_x(t-t_e)} & \forall t \ge t_e \end{cases} \qquad [2.2]$$

One pool of pyruvate, lactate and alanine was assumed in this model. In contrast to the model described by Day and coworkers(Day 2007) this model includes the rate of injection, which is a result of the flow of material into the bioreactor. This was not necessary in a model of cells in a non-perfused system, but is important when small tip angles are used to assess magnetization as the substrate is flowing into the system. The exchange of lactate and alanine back to pyruvate was also not included in this model. While this will have an impact on measurement of ^{13}C label fluxes, it has been shown in an *in vivo* study of rats after injection of hyperpolarized [1-^{13}C] lactate that minimal hyperpolarized [1-^{13}C] pyruvate and [1-^{13}C] alanine signal is generated. This suggests that the impact of ignoring the exchange of ^{13}C label back to pyruvate in this model is relatively small, but more importantly for the goals of this study, reflects the physiological system during ^{13}C DNP MRSI experiments(Chen 2008).

2.2 Steady State Studies of JM1 cell cultures

Extracts of 2D Cultures and Determination of the Mass Balance of u-^{13}C-Glucose

Figure 2.2a is a representative ^{1}H spectrum of the aliphatic region obtained from a methanol extraction of JM1 cells after metabolism of ^{13}C-substrate for 23 hours. ^{13}C satellites of lactate, alanine, glutamate (both as glutamate and as the glutamyl group of the tripeptide glutathione) and the nucleotide riboses (not pictured) are visible. The concentrations of these five compounds plus pyruvate and glucose in the initial media formulation and at 23 hours from the cell methanol extract and 2D culture media are given in **Table 2.1.** In comparison to normal rat liver(Nicholas 2008), the JM1 rat hepatoma cell-line produces significantly more lactate and alanine, and ribose (**Table 2.1**), demonstrating the Warburg effect and pentose phosphate pathway products for nucleotide synthesis, respectively. They also demonstrate a high concentration of glutathione, which has been observed in other cell lines such as MCF-7 human breast cancer(Gamcsik 2002) and DU145 prostate cancer cells(Balendiran 2004). In fact, one of the largest resonances in the ^{1}H spectrum is from glutathione (**Figure 2.2a**).

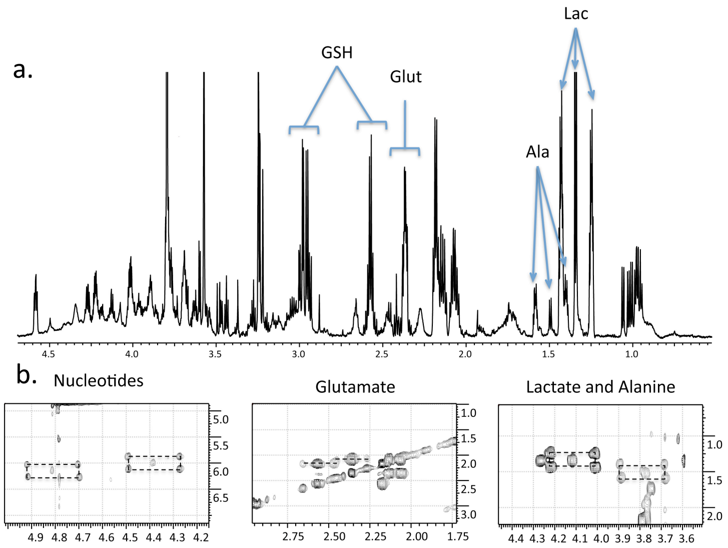

Figure 2.2. (a) Representative ^{1}H spectrum of water soluble metabolites at 23 hours (b) Representative TOCSY spectra showing fractional enrichment of compounds by infusion of u-^{13}C-glucose.

	Initial Media (μmols/15mL)	**2D Cultures (Methanol)** (μmols/10^6 cells)	**2D Cultures (Media)** (μmols)
Glucose	249	-	111.84 ± 7.61
Pryuvate	15	-	-
Glutamate	0	0.037 ± 0.002	-
Glutamine	60	-	53.95 ± 0.63
Glutathione	0	0.046 ± 0.004	-
Alanine	0	0.026 ± 0.003	17.07 ± 1.53
Lactate	0	0.091 ± 0.007	242.57 ± 15.79
X-Purine	0	0.002 ± 0.0004	-
X-Pyrimidine	0	0.002 ± 0.0005	-

Table 2.1. Table of the glucose, pyruvate, glutamate, glutamine, alanine, lactate, X-Purine, X-Pyrimidine, and glutathione concentrations in the cell methanol extract (t=23hr), media from 2D cultures at 23 hr, and from the initial media formulation. – indicates compounds below detection

Representative regions of a typical 2D ^{1}H-^{1}H TOCSY spectrum are shown in **Figure 2.2b**, demonstrating cross-peaks used to determine the ^{13}C fractional enrichment (FE) of the previously mentioned compounds. At 23 hours, lactate and alanine FE's are 88.9 ± 2.9 % and 57.8 ± 3.1% respectively. The glutamate and glutamyl of GSH have FE's of 7.1 ± 2.2% and 10.1 ± 2.4% respectively. The FE's of the ribose in nucleotides were similar for both purines and pyrimidines, enriching to 91.6 ± 2.7 and 91.5 ± 3.8%. It is important to note that after 5 minutes, the lactate pool inside the cell had a FE of 55.1 ± 7.9%, while that of alanine was 14.0 ± 5.9%. Glutamate labeling was not detectable at 5min. Not surprising, lipids were not labeled to a detectable level, likely because lipids form from anapleurotic products of the Krebs cycle. These intermediates were at most labeled to 10% as can be inferred from the glutamate FE and could have in turn labeled the lipids to a level below detection in this study.

By quantifying the absolute number of μmols of ^{13}C for each compound at 23 hours in the cell, a distribution of label can be generated, which is shown in **Figure 2.3.** Nearly 85% of the label is present as either lactate or alanine in JM1 cells after 23 hours. Activity of the pentose phosphate pathway in converting glucose to the ribose backbone of nucleotides accounts for approximately 4.7% of the ^{13}C label distribution while another 9.2% are resident in glutamate (half of which is GSH). At the 23hr time point, each 150cm^2 plate of JM1 cells had produced 242.57 ± 15.79 μmols of lactate and 17.7 ± 1.53 μmols of alanine and exported it to the media.

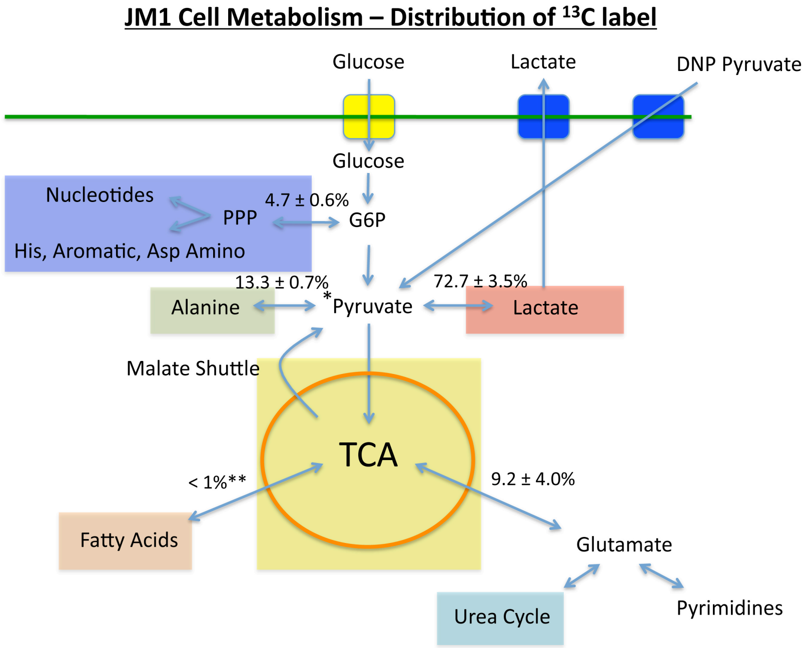

Figure 2.3. Cancer Metabolic Phenotype. Percentages ± standard of deviation are shown for the distribution of ^{13}C compounds in the cell as a result of media supplemented with u-^{13}C glucose. The DNP pyruvate arrow denotes the mechanism for infusion of hyperpolarized pyruvate and its relationship to the distributions measured in 2D cultures of JM1 cells. Yellow box – GLUT (1,3,4) Blue box – MCT – monocarboxylate transporter (predominantly 4). Light blue – Pentose Phosphate Pathway (PPP) flux into ribose etc.... Pink box – Anerobic/Aerobic glycolysis. Light yellow box – Tricarboxylic Acid Cycle (TCA). Aqua box – Urea cycle. Light Red box – Fatty Acid synthesis as a result of exchange with TCA pathway. Light green box – flux through ALT and into protein synthesis. * Indication of methodology of hyperpolarized pyruvate. **In lipid extracts, carbon labeling was below detection.

2.3 Real-time DNP measurements of JM1 cell metabolism

Bioreactor cultures of JM1 cells and ^{31}P NMR studies

^{31}P spectra were used to monitor changes in cell energetics with growth over time. **Figure 2.4a** shows a representative 500μm bead of encapsulated JM1 cells, cryosectioned and stained by hematoxylin and eosin (H&E) at 20X magnification. JM1 cells were evenly distributed throughout the alginate beads and were predominantly spherical. **Figure 2.4b** shows a representative ^{31}P spectrum of JM1 cells encapsulated to a concentration of 1.2 x 10^8 cells/mL at 4 hours of perfusion in the bioreactor. NMR signals for the phopsphates of the NTPs (γNTP, αNTP, and βNTP), phosphocholine (PC), inorganic phosphate (Pi), glycerophoshocholine (GPC), glycerophosphoethanolamine (GPE), nicotinamide (NADH, reduced and oxidized), diphosphodiesters (DPDE - most commonly UDP-glucose)(Kurhanewicz 1992; Gillies 1994; Macdonald 1998) and the sugar phosphate groups (Sugar PO_4^{-3}) are readily visible.

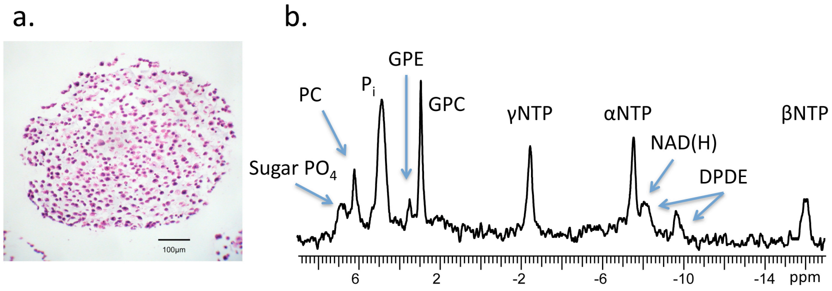

Figure 2.4. Representative ^{31}P and histology of encapsulated beads. (a) H&E stained section of a 500μm bead of encapsulated JM1 cells at 20x magnification. (b) representative ^{31}P spectrum at 4 hours post encapsulation and perfusion in the bioreactor. γNTP, αNTP, and βNTP represent the phosphates of the NTPs. PC – phosphocholine, Pi – inorganic phosphate, this peak is composed of the P_i inside and outside the cell. GPC – glycerophoshocholine, GPE – glycerophosphoethanolamine, NAD(H) – nicatinamide (reduced and oxidized), DPDE – Diphosphodiesters most commonly UDP glucose. Sugar PO4 – sugar phosphate groups

Figure 2.5a shows a representative ^{31}P time course of βNTP changes of JM-1 cells growing in the bioreactor over the time course of the bioreactor studies. The dotted red lines indicate the time of injection of hyperpolarized [1-^{13}C] pyruvate. Increases in βNTP correlate to the cell concentration and is indicative of the cell growth with time(Kurhanewicz 1992; Macdonald 1993; Gillies 1994; Mancuso 2005). About 80% of βNTP is adenine nucleotide and about 90% is NMR visible in rat liver(Masson 1992). As cells grew inside of the bioreactor, hyperpolarized [1-^{13}C] pyruvate was injected to assess conversion of pyruvate to its metabolic products. **Figure 2.5b** demonstrates ^{31}P spectra before and immediately after two injections of hyperpolarized [1-^{13}C] pyruvate at 4 and 18.5 hours. Increases in the

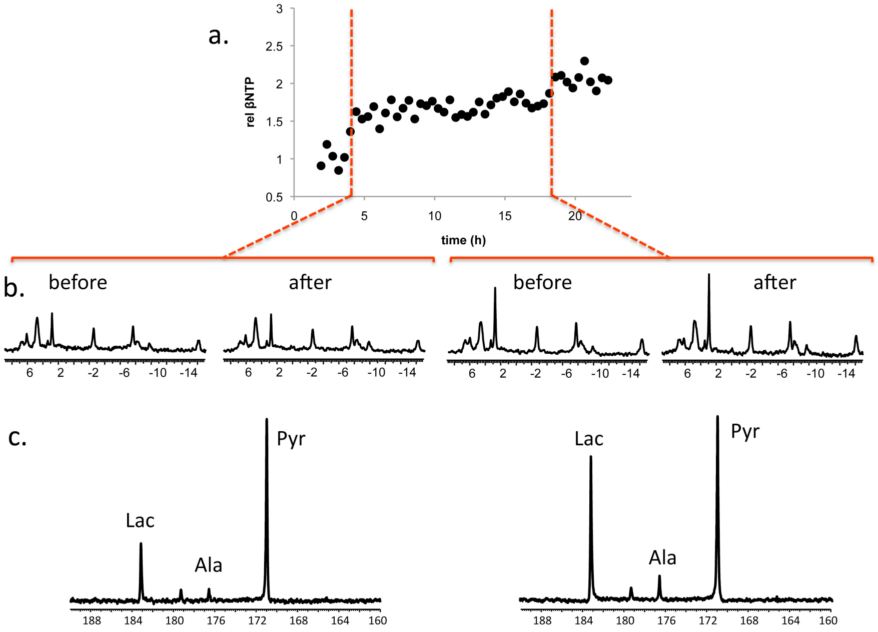

Figure 2.5. ^{31}P monitoring and dynamic ^{13}C spectra of JM1 cells. (a) A ^{31}P time course showing the relative changes in βNTP as JM1 cells encapsulated at a concentration of 127 x 10^6 cells/mL change over time. (b) before and after ^{31}P spectra at the dictated time points of injection of 1mL of 7.1mM hyperpolarized pyruvate, 4 hours and 18.5 hours respectively. (c) ^{13}C spectra at 90s post injection, demonstrating the conversion of pyruvate (171ppm) to lactate (182ppm) and alanine (175ppm).

^{31}P resonances at the later time point demonstrate that the cells not only survive the injection, but continue to grow over time.

Previous ^{31}P NMR studies of NMR-compatible bioreactors containing alginate encapsulated transformed cells(Narayan 1990) showed that cells are viable for several days. Here we demonstrate that the cells double in a comparable period of time as in 2D cultures of JM1(Macdonald 1993). This is likely due to the uniform diameter of 500 μm, which was permitted by use of electrostatic encapsulation. In normal aerobic cells such as hepatocytes, the diffusion distance for oxygen is typically 200 μm, cells become hypoxic at greater diffusion distances(Macdonald 1998; Gross 2007). Transformed cells consume less oxygen than primary hepatocytes at 250 μm, the maximal diffusion distance in the 500 μm diameter encapsulates. Although an oxygen gradient is created in the 500 μm diameter encapsulates, dictated by the diffusion coefficient and oxygen consumption rate, there would be little or no hypoxic zone within the encapsulate compared to previous studies that used >1 mm diameter(Narayan 1990). In short, the relatively small and uniform diameter of the encapsulates permitted sufficient diffusion of hyperpolarized [1-^{13}C] pyruvate to the cells.

Bioreactor cultures of JM1 cells and ^{13}C NMR DNP studies

Figure 2.5c demonstrates injections of 1ml of 7.1mM hyperpolarized [1-^{13}C] pyruvate at 4 hours and 18.5 hours in the same bioreactor system. Each ^{13}C spectrum is at 90s post-injection and shows the high signal-to-noise ratio of labeled lactate and alanine as a result of interconversion from the injected pyruvate. The spectrum on the right exhibits higher SNR, due to the characteristic cell growth over time of the JM1 cells in the bioreactor. Lactate and alanine production as a result of flux through LDH and ALT, respectively was seen to scale with cell concentration as expected.

Hyperpolarized ^{13}C spectra were integrated and time courses of lactate and

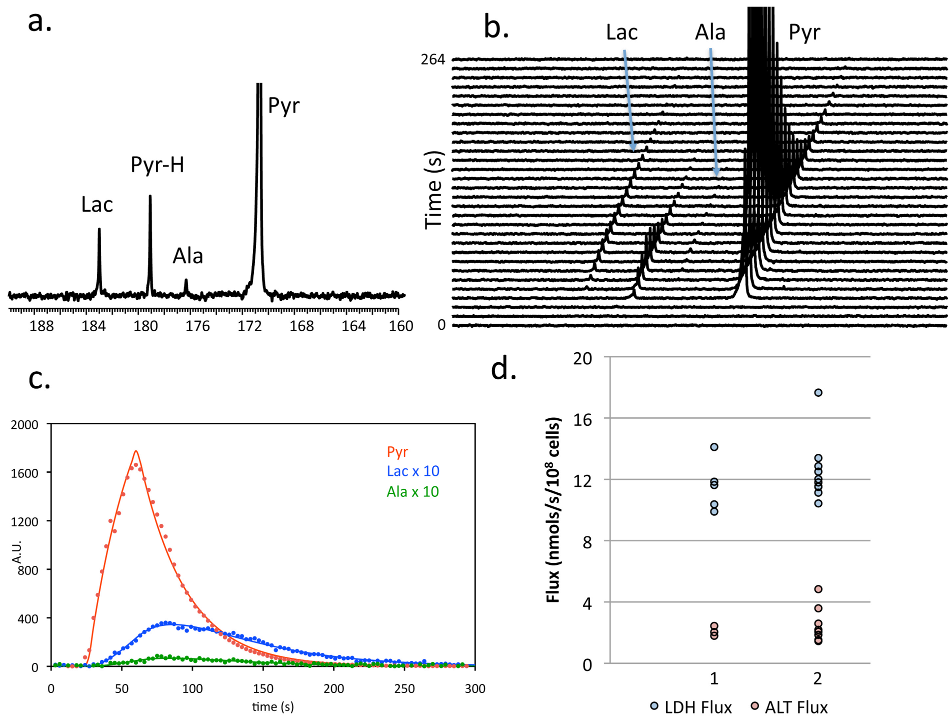

Figure 2.6. Study in bioreactor of JM1 cells at a concentration of 50 x 10^6 cells/mL. (a) ^{13}C spectrum acquired at 84s post injection of 2mL of 3.56mM hyperpolarized pyruvate. (b) Every third ^{13}C spectrum acquired demonstrating the hyperpolarized ^{13}C labeling of lactate (Lac) and alanine (Ala) as result of ^{13}C pyruvate (Pyr). Pyruvate hydrate (Pyr-H) is also shown which is in equilibrium with pyruvate. (c) red dots – pyruvate, blue dots – lactate x 10, green dots – alanine x 10, the lines for each respective color are the fits as a result of the flux model for ^{13}C labeling of lactate and alanine via LDH and ALT respectively. (d) LDH (blue) and ALT (red) flux measurements for day 1 and 2 in the bioreactors.

alanine were generated. **Figure 2.6** shows the ^{13}C spectrum of a bioreactor at 84s post-injection (a) and its representative signal over time (b). The influx of pyruvate as a result of the injection is shown and peaks corresponding to it's metabolic products, lactate and alanine, are observed within 2 scans (i.e. 6 secs) of the pyruvate signal. A representative time course of ^{13}C lactate, alanine and pyruvate is shown in **Figure 2.6c**. This data was fit to a 2 state model of the interconversion of pyruvate to lactate and alanine, and the fit is shown as the solid line through the raw data. The flux rates of [1-^{13}C] pyruvate to [1-^{13}C] lactate and [1-^{13}C] alanine, facilitated by LDH and ALT, were determined to be 12.18 ± 0.49 nmols/s/10^{8} cells and 2.39 ± 0.30 nmols/s/10^{8} cells respectively. The low standard error in the bioreactor supports the reproducibility of the system as a real-time measurement of the flux through LDH. The measurement for ALT flux exhibited a higher standard error, most likely due to the lower signal to noise of [1-^{13}C] alanine in hyperpolarized studies, in comparison to lactate. **Figure 2.6d** demonstrates the differences between flux measurements that were made on the first and second day in the bioreactor system. LDH flux and ALT flux were not found to be significantly different between the two days (p=0.4 and 0.6 respectively). Multiple injections of hyperpolarized [1-^{13}C] pyruvate were done on all bioreactors yielding similar results, thus reinforcing the robustness of not only the bioreactor system, but also the flux measurement by hyperpolarized [1-^{13}C] pyruvate injection. This data suggests that differences in metabolic fluxes with cellular perturbations (i.e. changing oxygen tension, metabolic substrates, and/or therapy) as small as 5% can be measured in the bioreactor. Also having accurate control over the bead size (500 μm) of the encapsulated cells provided an environment in which all cells are equally perfused (i.e., the 250 μm diffusion limit was maintained), a situation that is closer to physiological than provided by other NMR-compatible bioreactors(Mancuso 1990; Narayan 1990; Macdonald 1993; Macdonald 1998).

The pyruvate metabolism in the bioreactor system, assessed by the DNP method, demonstrated analogous fluxes through LDH and ALT as those of glucose in the standard 2D culture system. Unlike the first cell study showing flux through LDH by DNP(Day 2007), concentrations in this study (**Table 2.1**) were closer to the physiologic conditions, as a result of continuous perfusion. The bolus of pyruvate creates a spike in pyruvate concentration that is similar for both perfused bioreactor and *in vivo* MRSI studies. Typically, the serum concentrations for these compounds are in the half to several millimolar range, and media is near this range except for glucose which several fold higher (25 mM (4.5g/L) versus 3.9 to 6.1 mM (0.7-1.1 g/L) as well as pyruvate, which is very low in serum (500 μM versus 100 μM). The goal of this study was to generate a model similar to an animal model. Although both in bioreactor and *in vivo* DNP studies a non-physiologic bolus of pyruvate is given, a similar dose can be given in both cases for comparison of the *ex vivo* and *in vivo* fluxes. This information can be used in order to rapidly test novel molecules and save time, money, and animal lives for development of DNP imaging.

Metabolic fluxes, even for kinetically fast enzymes such as LDH, can be measured while maintaining cells in a physiologically viable state. This also allows for the monitoring of enzyme concentration as well as real time metabolism by way of modulation of substrate concentration. Combining ^{13}C labeling inter-leaved between hyperpolarized ^{13}C studies would allow for the assessment of both kinetically fast and slow metabolic processes. It must be noted that hyperpolarized ^{13}C studies may not be appropriate for measuring slower metabolic fluxes or sequential steps in an enzymatic pathway (i.e. flux to glutamate or fatty acids).

However, the dramatic increase in sensitivity provided by DNP will potentially allow for the measurement of fast metabolic fluxes in people.

Summary of JM1 DNP experiments

This study demonstrates that hyperpolarized ^{13}C NMR can be combined with an NMR-compatible bioreactor to measure metabolic fluxes in 3D cell cultures. JM1 hepatoma cells were found to have high rate of aerobic glycolysis in both conventional 2D culture and in the bioreactor. The high sensitivity of hyperpolarized ^{13}C NMR allowed the measurement of metabolic fluxes in real time. Although this preliminary study involved immortalized cells, this combination of technologies could be extended to the real-time metabolic exploration of primary benign and cancerous cells and tissues.

Chapter 3: Cartridge Bioreactor Design and Hyperpolarized NMR

3.1 Design of cartridge bioreactor system

As was discussed in Chapter 2, the most efficient diffusion of metabolic nutrients and gases can be achieved in a perfused bioreactor composed of beads (spheres). Since the diffusion coefficient of oxygen, resulting in the local oxygen concentration, tends to be the limiting factor in most bioreactor designs, a sphere with radius of ≤0.25mm(McClelland 2003; Gross 2007) is ideal. The major limitation resulting from the perfused bead or fluidized bioreactor design is the difficulty in imaging the system. Imaging can provide a means of looking at the heterogeneity in perfusion and metabolism of hyperpolarized probes, and becomes particularly important for bioreactors involving more complex cell co-cultures and in tissues. Because the "cells/tissue" is constantly moving in packed-bead bioreators, resulting in blurring artifacts, it is not conducive to high-resolution imaging or spectroscopic imaging. This implies the need for transition to bioreactor designs that will be stationary and thus take advantage of the high spatial resolution imaging, which can be achieved by hyperpolarized techniques.

Other bioreactor designs (cf. 1.4) have attempted to overcome the diffusion limitation in more stationary fixtures, including gel threads. These are difficult to perfuse and tend to aggregate and further exclude regions from perfusion at physiologic temperatures (37°C). In contrast, hollow fiber (HF) bioreactors maximize diffusion rates, though they are difficult to adapt to high-resolution systems. With the diffusion distance limitation as a prerequisite, a composite HF bioreactor was designed to fit inside of a standard 10mm NMR probe. This cartridge system is perfused from the top through a center HF (**Figure 3.1**). When the perfusate exits the fiber it refluxes back up through 8 radially distributed 1mm HFs and exits the top of the cartridge. A cell ECM mass is inoculated in the extra-hollow fiber space and is perfused via radial diffusion (or Starling Flow leakage), similar to an inversion of the traditional bioreactor system where the perfusate is outside of the fiber and the cell mixture is inside the fiber core. The effect these diffusion distances have on oxygen gradients will be discussed in the following section (§3.2).

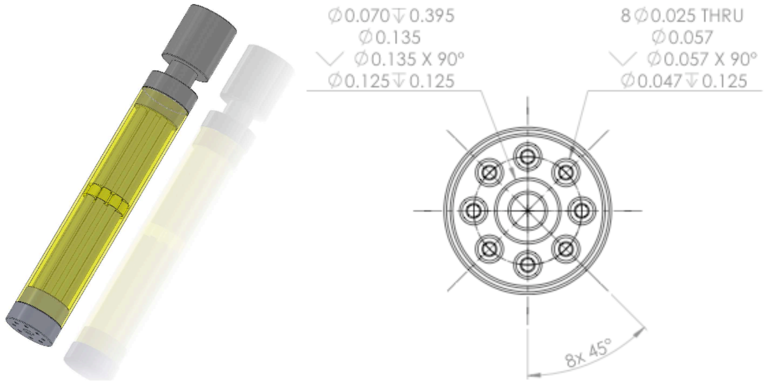

Figure 3.1. Schematic of bioreactor cartridge showing ring of 8 HFs (diamter 1mm) and central HF line (diameter 3mm).

The cell mixture can be any combination of cell suspension and ECM, which provides a rigidity and potential signaling necessary for cell survival and growth. In the series of studies associated with this chapter, the ECM will be Matrigel®, a basement matrix which contains an array of constituents (predominantly collagen type 1) and has been previously used in cell culture studies of cancer cell lines(Gillies 1993; Benelli 1999; Ackerstaff 2001). One property of this ECM is that it is a liquid at low temperatures and solidifies at higher temperatures (~37°C), which makes it conducive to pouring into a mold on ice and allowing to solidify as a cell culture is brought to physiologic temperatures. In comparison to agarose, Matrigel® can be kept at cold temperatures during the inoculation process, potentially preserving cell viability. This allows for a potentially higher cell viability and uniform bioreactor inoculation.

3.2 Oxygen diffusion as it applies to bioreactor development

Oxygen diffusion into a cell culture system has been the subject of investigation and modeling as early as the mainstream adoption of long-term cell

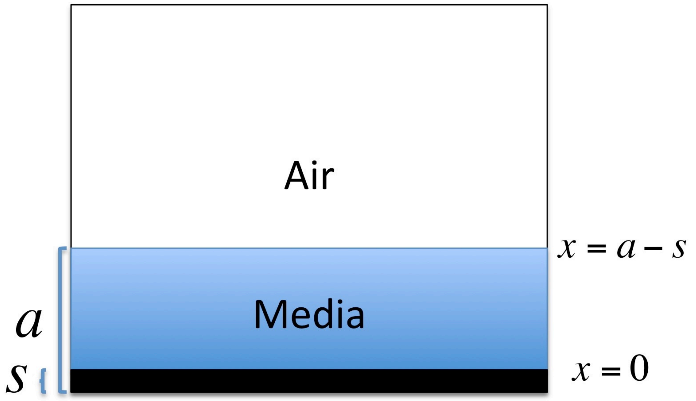

Figure 3.2. Schematic of simplified culture dish. s = monolayer of cells, a-s = height of fluid, x = height

cultures(McLimans 1968). Some of the first estimations were geared toward the modeling of a tissue culture dish (or flask) to understand the fluid depth necessary to balance between compensation of cell respiration and anoxia. If we define a tissue culture flask (**Figure 3.2**) with a monolayer of cells of some height *s*, and some layer of air above the fluid, the concentration of a gas (here oxygen) can be modeled as a function of time:

$$c(x,t) \quad \forall x \in [0,a-s] \quad \forall t \geq 0 \qquad [3.1]$$

We assume that the partial pressure in the air layer maintains a constant source *b*.

$$c(a-s,t) = b \quad \forall t \qquad [3.2]$$

Since the initial [O_2] in the media layer was *b* then we assume at *t=0*:

$$c(x,0) = b \quad \forall x \in [0,a-s] \qquad [3.3]$$

Because there is an inherent gradient, the diffusion and resulting concentration of gas (here oxygen) into media at the bottom of a cell culture flask can be modeled starting from Fick's Law(Fick 1855):

$$J = -D\nabla c \qquad [3.4]$$

It is assumed that the area in two dimensions is constant (the gradient is in the z or height direction) thus Fick's Law becomes one dimensional including the cross sectional area (*A*):

$$J(x) = -D\frac{\partial c(x,t)}{\partial x}Adt \qquad [3.5]$$

$$J(x+dx) = -D\frac{\partial c(x+dx,t)}{\partial x}Adt \qquad [3.6]$$

The net *J* or *ΔJ* can be defined as :

$$\Delta J = J(x) - J(x+dx) = -D\left[\frac{\partial c(x,t)}{\partial x} - \frac{\partial c(x+dx,t)}{\partial x}\right]Adt = D\frac{\partial^2 c(x,t)}{\partial x^2}Adtdx \qquad [3.7]$$

With the total change in $[O_2]$:

$$[c,(x,t+dt) - c(x,t)]Adx = \frac{\partial c(x,t)}{\partial t}Adtdx \qquad [3.8]$$

Equating equation 24 with 25 yields the standard diffusion equation.

$$\frac{\partial c}{\partial t} = D\frac{\partial^2 c}{\partial x^2} \qquad [3.9]$$

The sink *Q*, is defined as the rate of loss of the gas (in this case the utilization). Because net flow is maintained at *x=0*:

$$D\left[\frac{\partial c(0,t)}{\partial x}\right] = Q \qquad [3.10]$$

With boundary conditions [3.1, 3.2, 3.10] the concentration in time can be approximated by solving the partial differential equation (PDE) [3.9]. This PDE can be solved in many ways; one method is by using separation of variables and the general solution (shown below in equation 3.11).

$$u_\lambda(x,t) = \left(A_\lambda \cos\lambda x + B_\lambda \sin\lambda x\right)\exp\left\{-\lambda^2 Dt\right\} \qquad [3.11]$$

Boundary conditions can be applied:

$$\frac{\partial u(0,t)}{\partial x} = 0 \Rightarrow B_\lambda = 0 \qquad [3.12]$$

$$\cos\lambda(a-s) = 0 \qquad [3.13]$$

$$\lambda = \left(\frac{2n+1}{2(a-s)}\right)\pi \quad n = 0,1,2,\ldots$$

The general solution, after application of the boundary conditions then becomes:

$$u(x,t)=\sum_{n=0}^{\infty} A_n \cos\left(H_n x\right)\exp\left\{-H_n^2 Dt\right\}\ ,\ H_n=\frac{2n+1}{2\left(a-s\right)}\pi \qquad [3.14]$$

After solving for A_n using the boundary conditions and transformation back to *c(x,t)*, with substitution of *(a-s-x)(Q/D)* the equation becomes:

$$c(x,t)=b-\frac{2Q}{\left(a-s\right)D}\sum_{n=0}^{\infty} H_n^{-2}\cos\left(H_n x\right)\left[1-\exp\left\{-H_n^2 t\right\}\right] \qquad [3.15]$$

With steady state solution:

$$c(x,\infty)=b-\left(a-s-x\right)\frac{Q}{D} \qquad [3.16]$$

As defined in [3.16] the steady state concentration is a function of the sink, source, height of media and diffusion coefficient. The sink can be further delineated to represent the actual components of respiration at the level of the monolayer [3.17].

$$c(0)=b-(a-s)\frac{Q}{D}=b-(a-s)\frac{RC}{D} \qquad [3.17]$$

Where R = cellular respiration rate and C = cell number/cm^2.

McLimans et al. (1968) have applied this model to both immortalized cell lines and primary hepatocytes in monolayer culture to estimate the relationship

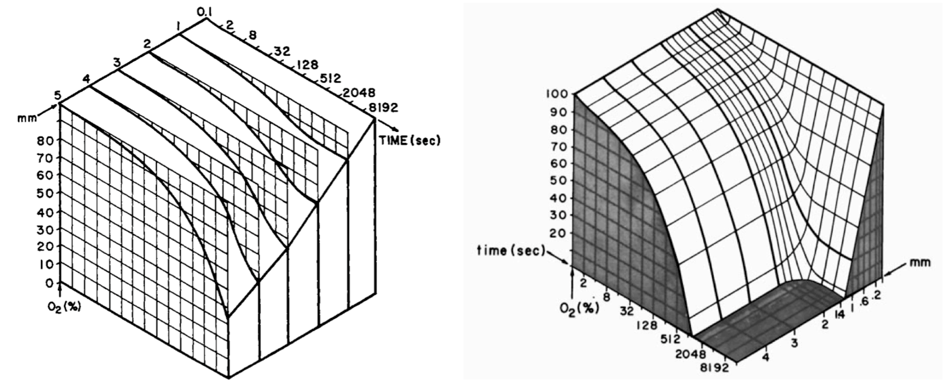

Figure 3.3. Reproduced from McLimans et al. 1968. Gas diffusion with time and fluid depth are shown for both immortalized cells (left) and primary hepatoctyes (right).

between fluid depth and oxygen concentration for respiring cells. **Figure 3.3** demonstrates the difference in oxygen concentration with respect to time for both immortalized mammalian cells and primary hepatocytes with respiration rates of 1.42×10^{-12}mL O_2/cell/sec and 7.36×10^{-12}mL O_2/cell/sec (both at cell densities of 2.63×105 cells/cm^2). For immortalized cells, with 2mm solution depth 93% of the original oxygen concentration will be present after 128 secs. In contrast, at 1.6mm of media, the initial equilibrated oxygen in a primary culture of hepatocytes will be completely exhausted in 1280 secs, implying that in cell culture plates, primary hepatocytes at this cell density will not survive greater than 2mm solution depths. Thus media levels can directly influence the extent of cell growth, the ultimate density of cells, and the maintenance of this density. Furthermore, the real time presence of an oxygen gradient in an engineered system has great implications for the sustainability of high-density cultures.

This has been further extended to more sophisticated experimental procedures to measure the mass transfer at the bottom of a T-flask(Randers-Eichhorn 1996). Randers-Eichorn et al. (1996) demonstrate the growth of murine hybridoma cells in a T-225 flask is a function of dissolved oxygen (DO) at the level of the monolayer. Cells grow in log phase until they approach the limitations of the DO in culture. This has dramatic impact on the performance of a 3D bioreactor design, because oxygen diffusion can limit the survival of a high density of perfused cells.

The diffusion properties of an HF bioreactor have been estimated to an equation similar to [3.9] allowing for a term, *q*, which represents the respiration rate of cells in culture(McClelland 2003).

$$\frac{\partial C}{\partial t} = D_{normal}\left[\left(\frac{\partial^2 C}{\partial x^2}\right)\right] - q \qquad [3.18]$$

This model of the concentration through a HF is applicable along the entire length of the fiber assuming the flow rate is high enough to induce Starling Flow(Starling 1896) or leakage flow, because diffusion alone is often insufficient to provide adequate mass transfer of substrates. Changes in radial flow velocities have been modeled in a concentric HF bioreactor(Heath 1990) and these create added complexity for cell systems design at high media flow velocities (e.g. 250mL/min). High flow velocities in hollow fiber bioreactors have been used to yield axial velocties, which can compensate for mass transport across large distances (> 2mm). Assuming a flow rate necessary to generate Starling flow radially, the plots in **Figure 3.4** were generated to estimate the steady state concentration of oxygen in a given slice through a fiber. Assuming the concentration of oxygen at the center is the concentration delivered by a HF, radial diffusion with consumption by hepatocytes (0.42nmols/s/10^6 cells)(Macdonald 1999), steady state concentrations of oxygen can be significantly depleted at distances greater than 500μm from an HF. Using this distance as a limit, a HF design was constructed with 8 polysulphone HFs (AG/Technology, Needham, MA) in a ring, no more than 0.5mm from center to center (**Figure 3.4**). As can be seen this greatly enhances the oxygen concentration in the region of interest and limits the axial flow velocity necessary to maintain the nutrient concentration at steady state.

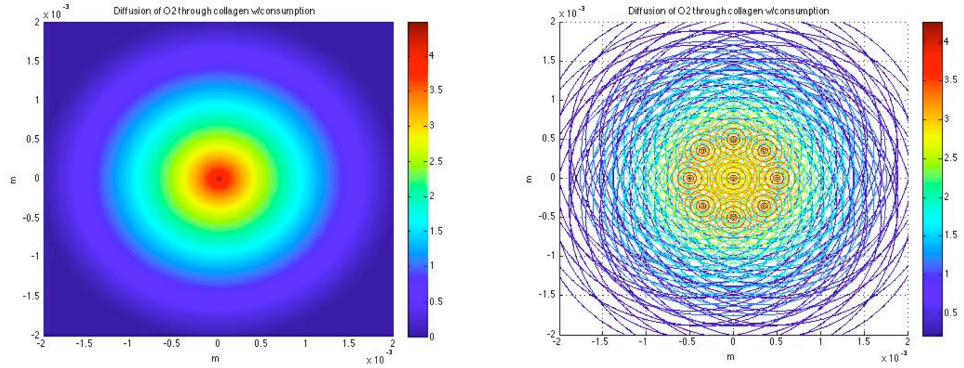

Figure 3.4. Estimated steady state concentrations of oxygen in a slice through a HF into ECM. One fiber (left) and an 8 fiber ring around a central fiber (right) are shown to demonstrate the gradient of oxygen concentration over a distance from the center of any given fiber. The units of the gradient are in mM O_2.

This model design was used to construct an HF based NMR-compatible cartridge for perfusion of cell cultures and tissues (§Appendix B). The central body is constructed of a susceptibility matched (to water) material, Ultem 1000®, with top and bottom caps milled from Delrin®. The caps are designed to hold eight 1.2 mm outer diameter HFs, equidistantly spaced in a ring around a central 3mm outer diameter HF (AG/Technology, Needham, MA). The 1.2 mm polysulphone HFs have a high porosity of 0.65 µm pore size with a hydraulic permeability of 3.6×10^{-4} mL/min/mm Hg/mm^2, while the 3 mm polysulphone HF is far less porous with 0.1 µm pore size with a hydraulic permeability of 5.3×10^{-6} mL/min/mm Hg/mm^2 (Wolfe 2002). Together, these HFs allow for the radial diffusion of nutrients throughout the cartridge. The structure is designed so that the fibers are held in place by the cartridge caps and the extracellular matrix used to imbed the cells. If the cartridge is applied to tissues or tissue slices, they are suspended inside of the cartridge and the fibers can allow for structure and increased axial diffusion.

3.3 Characterization of cartridge system by steady state (^{31}P), dynamic measurements ^{13}C and imaging in Human Prostate Cells and Tissues

As previously introduced (§2.1 and 3.1), the dynamic assessment of metabolic systems is of great interest both for the characterization of cellular systems *in vitro* and for the extension to probing changes. Perfusion systems or bioreactors, have been used to investigate a wide range of disorders through manipulations of cell lines(Ronen 1989; Narayan 1990; Gillies 1994; Mancuso 2004) observing changes in metabolism (§1.3). The extension of these systems to cell masses and tissues has been very difficult due to the limitations in diffusion distances. This same problem arises in subcutaneous injections of oncogenic cells in nude mice. Typically tumors that arise from these cell lines are poorly vascularized making them atypical in metabolism as well as difficult to probe using real time methods such as hyperpolarized MR. The purpose of this section is to introduce the application of the cartridge bioreactor to both human prostate tissue slices and an extracellular embedded mass of human prostate cancer (PC3) cells.

Prostate Cancer (PC3) cell Study Methods

Approximately 90 million PC3 cells were re-suspended in 1mL of cultured in DMEM medium (Invitrogen, 3g/L glucose) supplemented with 10% fetal calf serum, 100 units/mL penicillin and 100 μg/mL streptomycin (Invitrogen). Cells were grown in T150-flasks (Fisher) and incubated at 37°C in a 95% air/5% CO_2 prior to bioreactor studies (§Chapter 2). 1mL of the suspension was mixed with 1mL of Matrigel™ (BD Biosciences). 1.5mL of the cell suspension in ECM was then loaded into the previously described cartridge (§3.1 and Appendix B) with 8 vertical 1.2mm HFs and one central 3mm HF in a cooled Erlenmeyer flask. The base of the Erlenmeyer flask was filled with dry ice to create a below room temperature environment for the Matrigel™ to not solidify. After the cartridge was loaded, it was interfaced with rest of the bioreactor unit (§2.3 and Appendix A) and perfused at a rate of 5mL/min.

Tissue Slice Study Methods

In this preliminary series of studies, human tissue slices were acquired from prostatectomy patients through collaboration with the Peehl Lab at Stanford University. Briefly, 3mm biopsy cores were taken from the removed prostate and sectioned to approximately 250µm using a tissue slicer. Slices were then suspended in media (§Appendix C) and kept on ice until inoculation in the bioreactor. The first tissue slice bioreactor studies were constructed using a single 3mm hollow fiber in the center of the bioreactor. Slices were delicately wrapped around the fiber and media was pumped through the cartridge at 7mL/min in conjunction with a previously described flow bioreactor system (§2.1).

NMR Methods for PC3 cells and Prostate Tissue Slice Studies

^{13}C and ^{31}P data were acquired on either an 11.7T or 14.1T Varian INOVA (125 or 150MHz ^{13}C and 220 or 242MHz ^{31}P, Varian Instruments) equipped with a 10mm triple-tune direct detect broadband probe at 37°C and 100G/cm three-dimensional gradient insert (for imaging). Non-localized ^{31}P time courses were acquired before and after hyperpolarized injections using a TR=2s, nt=2048 or 3000 and a 90° flip angle. ^{31}P spectra were zero filled to 40,000 points and line broadened 20Hz. Assessment of changes in the β-NTP resonances as a function of time was used to monitor tissue health through the progression of the bioreactor experiments *in vitro*. Diffusion-weighted images were acquired using a standard spin-echo based pulse sequence with a 35G/cm diffusion gradient (B_o=1200) with 4 averages, slice thickness of 0.5mm, matrix size of 256 x 256 and field of view (FOV) of 1.6 cm x 2.0 cm. Hyperpolarized ^{13}C dynamic spectra were acquired using a 5° flip angle, TR=3s and acquired for 300s. Axial hyperpolarized ^{13}C images were acquired using a frequency specific 2D EPI sequence. Images were acquired with a TR=0.2secs, 32 x 16 (RO x PE), slice thickness of 5mm, FOV 2 cm x 2cm and an increasing flip angle scheme every 5 seconds (10°, 20°, 30°, and 90°).

PC3 cells in the Cartridge

Similar to studies of encapsulated JM1 cells (§2.3), ^{31}P spectra of PC3 cells embedded in Matrigel® show viable cells after multiple hours of perfusion. **Figure 3.5** demonstrates a ^{31}P spectrum after 44 hours in the bioreactor. Analogous to the JM1 cells, βNTP is readily visible and demonstrates the presence of steady state NTPs. A doubling time of ~32 hours was estimated from the ^{31}P time courses and this is similar to previously reported doubling times for PC3 cells in 2D culture(Hanigan 1999). In comparison to JM1 cells, PC3 cells exhibit high levels of phosphocholine (PC) relative to glycerophosphocholine (GPC), which has been reported for other PC3 cells cultures(Narayan 1990; Macdonald 1993) as well as xenographs of PC3 cells(Kurhanewicz 1992). Resonances corresponding to phosphoethanolamine (PE), glycerophosphoethanolamine (GPE), the diphosphodiesters (DPDE) and specifically NAD(H) are also present.

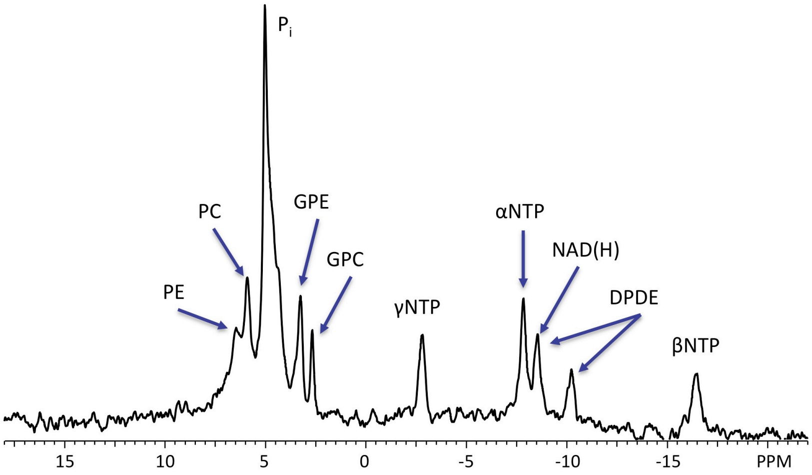

Figure 3.5. ^{31}P spectrum at 44 hours post-inoculation of 67.5 x 10^6 PC3 cells embedded in 1.5mL of Matrigel® mixed with medium. Resonances corresponding to the phosphomonoesters - PC and PE, phosphodiester – GPC and GPE, DPDEs, NTPs, NAD(H), and media and intracellular P*i* are readily visible, similar to previous cell line

Figure 3.6 demonstrates the generation of hyperpolarized [1-^{13}C] lactate after injection of 2.25mL of 30mM pyruvate, approximately 4 times the dose used in the JM1 cells (§2.4), at 4 hours post-inoculation in the bioreactor. This concentration is most likely well above that needed for V_{max}, but was used only to

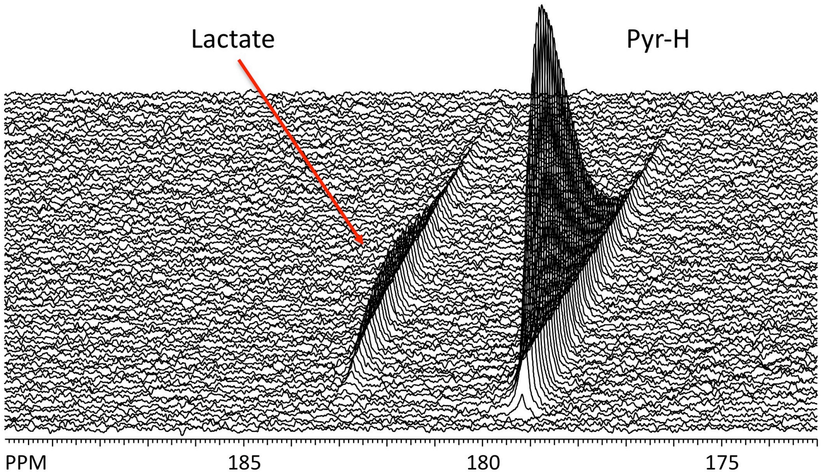

Figure 3.6. ^{13}C spectra demonstrating the generation of hyperpolarized lactate signal in time after injection of 30mM [1-^{13}C] pyruvate at 4 hours post-inoculation. Spectra are shown with a temporal resolution of 3 secs.

maximize the potential lactate signal generated. Lactate label is generated in real time evident from the peak area as a function of time, as compared to the pyruvate hydrate resonance, which decreases as a function of time and flow. Future studies of cells embedded in ECM will utilize much lower concentrations of pyruvate to explore the reaction kinetics of hyperpolarized pyruvate in PC3 cells.

A multipolarization of pyruvate and bicarbonate (§4.5) was also injected in the bioreactor at 25 hours post-inoculation, with concentrations of 10mM and 34mM respectively. At 21 secs post-injection (**Figure 3.7a**) the bicarbonate resonance can be observed along with CO_2, pyruvate and pyruvate hydrate. The calculated pH based on the Hendersen-Hasselbach equation is 7.4 (§4.5), which was similar to the pH calculated using the P_i resonance chemical shift (pH=7.45) as previously described(Seo 1983). There is a resonance on the shoulder of the P_i peak that corresponds to the intracellular Pi and is more acidic than the media (pH~7.05). After 30 scans lactate is visible on the order of pyruvate hydrate, 90 secs post-injection of the copolarization (**Figure 3.7b**), which

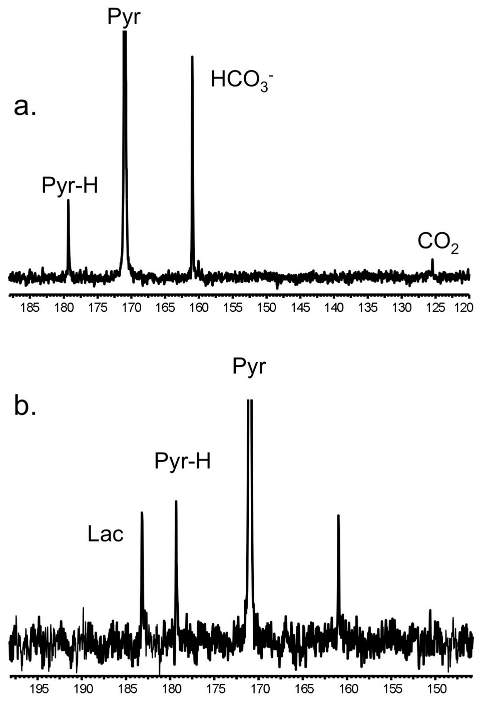

Figure 3.7. ^{13}C spectra demonstrating the copolarization of pyruvate and bicarbonate in the embedded cell bioreactor at 27 hours post-inoculation. (a) spectrum at 21 secs post-injection showing resonances corresponding to bicarbonate, pyruvate, pyruvate hydrate and CO_2 resulting in a pH of approximately 7.4. (b) a representative spectrum at 90 secs post-injection showing the generation of lactate similar to an injection 23 hours prior.

is similar to the pyruvate injection from the previous day. In comparison to JM1 cells in alginate encapsulates (§2.4), hyperpolarized alanine was not observed after injections of pyruvate, even at similar lactate levels. This is not surprising given the significantly higher activity of ALT in the liver, the origin of JM1 cells, as opposed to the prostate. Additionally similar amounts of lactate label were produced in the pyruvate only injection as compared to the copolarization, suggesting that simultaneous injection of bicarbonate has little or no effect on the flux of pyruvate to lactate via LDH.

A 1.5mL injection of 8mM hyperpolarized [2-^{13}C] fructose was also attempted (**Figure 3.8**) at 27 hours post-inoculation. The methods for polarization will be discussed in a future section (§4.2). The ratio of the 105.5ppm to the 102ppm resonances (predominantly β-fructopyranose) of 0.4 did not significantly change during the experiment. This is the ratio observed in polarized experiments of fructose alone and suggests that either metabolism is low or the excess of fructose in the media surrounding the tissue is swamping out any possible

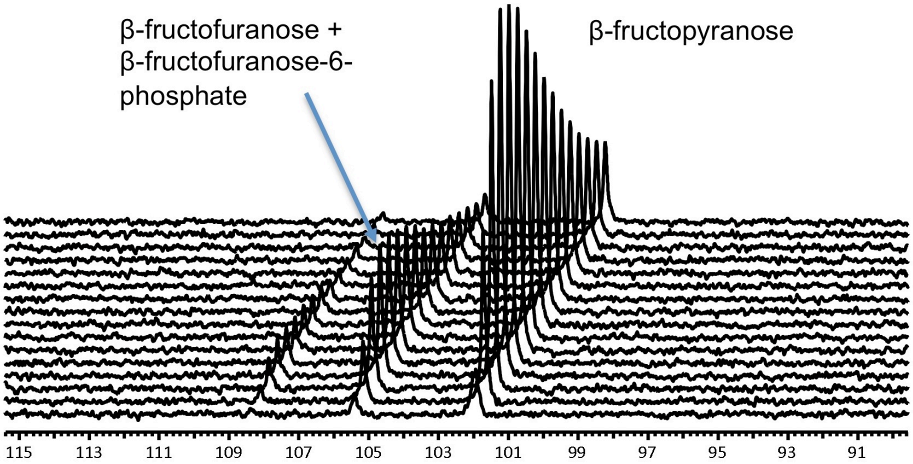

Figure 3.8. ^{13}C spectra demonstrating the injection of hyperpolarized [2-^{13}C] fructose at 27 hours post-inoculation. Resonances corresponding to the isomers of fructose are observed; the peak at 105.5ppm has been labeled as a composite of the fructose and phosphorylated fructose this is further described in §4.2.

observation of metabolism. Future studies of fructose in the bioreactor will require lower fructose doses and higher cell concentrations to observe these metabolic changes.

A recent mass spectrometry metabolomic study of samples from prostate cancer patients has implicated sarcosine (or n-methylglycine) as a potential biomarker of prostate cancer(Sreekumar 2009). In a later section [1-^{13}C] glycine was polarized to investigate mitochondrial activity (§4.4), but it could potentially be used to investigate the production of sarcosine via methylation of hyperpolarized [1-^{13}C] glycine. For this reason, 2mL of 13.3mM [1-^{13}C] glycine was injected into the bioreactor at 31 hours post-inoculation. **Figure 3.9** demonstrates the resulting hyperpolarized signal. No resonances corresponding to sarcosine were observed, most likely due to the relatively low PC3 cellularity and cellular concentration of sarcosine (Sreekumar 2009). Typical *in vivo* steady state concentrations were reported to be in the pico to nanomolar range and therefore below detection under current bioreactor conditions (Sreekumar 2009). Future bioreactor studies of

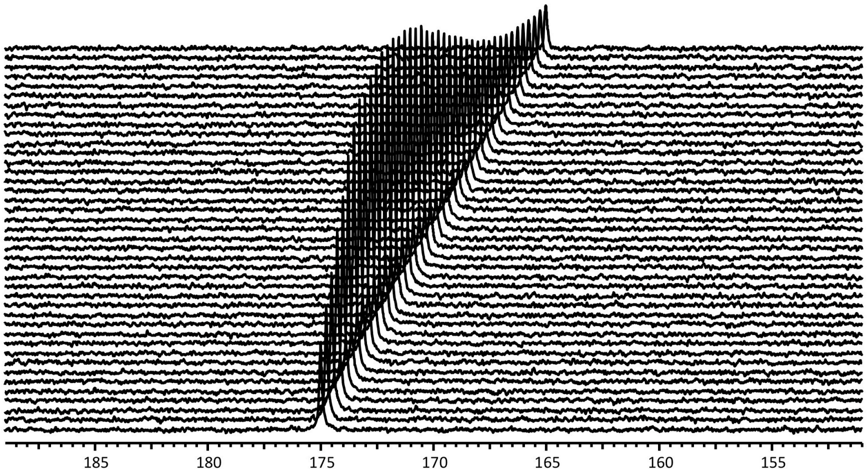

Figure 3.9. ^{13}C spectra demonstrating the 2mL injection of 13.3mM hyperpolarized [1-^{13}C] glycine at 31 hours post-inoculation. No other resonances are observed.

hyperpolarized [1-^{13}C] glycine will require higher cell densities to investigate the potential of observing hyperpolarized sarcosine.

In short, metabolism of PC3 cells was similar in the embedded gel cartridge bioreactor as previously reported for 2D cultures(Hanigan 1999; Chowdhury 2005) and perfused cell studies(Narayan 1990; Macdonald 1993). High levels of PC relative to GPC are indicative of fast rates of proliferation, which were observed in the bioreactor setting. Injection of hyperpolarized substrates into the bioreactor demonstrated adequate perfusion as well as enzymatic conversion, suggesting that the diffusion characteristics may be adequate for long-term cell culture. Further studies using this platform with different cell suspension to ECM ratios as well as hyperpolarized substrate concentrations will allow for a better characterization of *in vitro* real time metabolism.

Prostate Tissue Slice Studies in the Cartridge

Tissue slices were placed inside of a cartridge with a lone hollow fiber present at the center. The 250um slices were delicately wrapped around the fiber and surrounded by media and perfused at 7mL/min. In a first series of experiments, 36 slices (15 Gleason 3+4 cancer and 21 benign) were placed in the bioreactor in order to determine the duration of time that tissue slices could be maintained in a metabolically viable state. **Figure 3.10** demonstrates the ^{31}P time course of β-NTP over approximately 3 days. The β-NTP resonance stays constant for greater than 60 hours with a slight downward trend, which is expected for non-proliferating tissue.

A representative spectrum of ^{31}P at 63 hours from another tissue slice bioreactor is shown in **Figure 3.11**, demonstrating similar resonances to what was observed for both PC3 and JM1 cells (§2.2). Resonances corresponding to the phosphodiesters GPC and GPC were not observed and it appears that the ratio of the phosphomonesters PE and PC is dramatically different than for PC3 cells but more consistent with *ex vivo* human prostate tissue studies. In PC3 cell studies, PC is typically much higher than PE, but from studies of human tissue by HR-MAS(Swanson 2008), PE concentration has been shown to be significantly higher than PC concentrations. It is possible that the low levels of PC are representative of the percent of actively dividing cells in prostate cancer tissue. In most rapidly dividing cancers, such as brain and breast tumors, there are high proportions of cells in the S phase of growth and high concentrations of PC. In contrast, prostate cancer is typically considered a slow growing indolent disease and as such samples of prostate cancer tissue rarely stain greater than 10-15% for the Ki-67 protein (an antigen which stains for the cell nucleus in division)(Bruni 2004; Bullwinkel 2006).

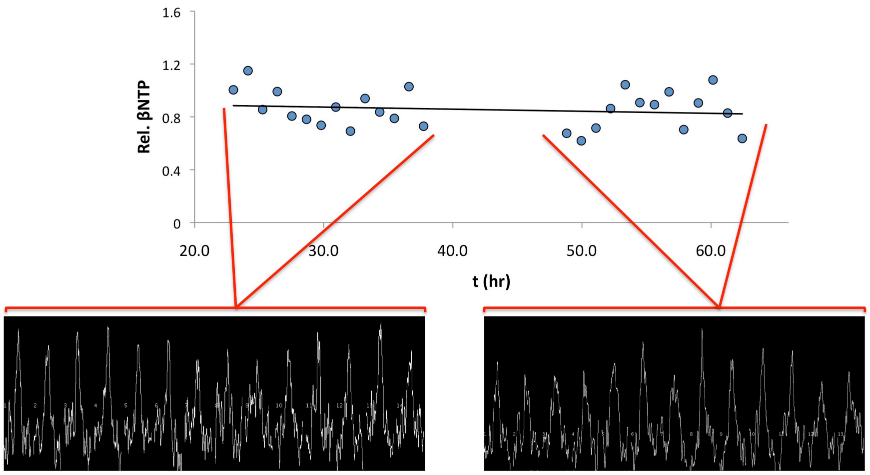

Figure 3.10. ^{31}P time course of a tissue slice bioreactor containing 36 slices (15 Gleason 3+4 cancer and 21 benign).

Though this bioreactor contained 33 slices of Gleason 3+4 cancer, the PC was still relatively low in comparison to PE, indicative of slow or non-dividing cells and similar to prior published human data.

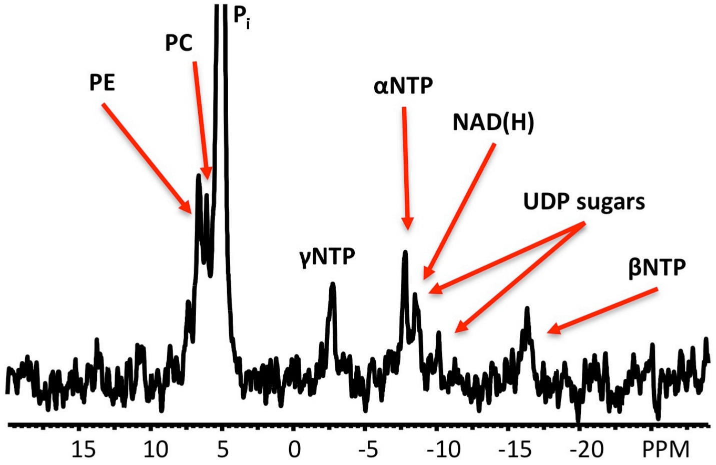

Figure 3.11. ^{31}P spectrum (nt=3000) at 63 hours post-inoculation of the bioreactor with 33 Gleason 3+4 slices. Resonances similar to those presented previously are observed.

In order to assess the distribution of slices in the bioreactor, diffusion weighted images were acquired through the center of the bioreactor. **Figure 3.12** shows 3 coronal slices through the bioreactor (separated by 0.5mm). The flowing media is clearly suppressed by the diffusion gradient and the 250μm tissue slices are readily visible. It is apparent that that the tissue slices are not moving enough to cause substantial blurring of the resulting images during the acquisition time (2 secs) of the imaging sequence used. 2mL of 20mM hyperpolarized [1-^{13}C] pyruvate was injected into the tissue slice bioreactor and generated a very small portion of labeled lactate. Five contiguous spectra of the dynamic stack taken every 3 secs were summed to generate the spectrum in **Figure 3.13**. Lactate is present, lower than expected, which is a function of the low tissue density, tissue metabolism as well as the real time non-optimized flow characteristics of this bioreactor.

It appears that in the case of a solo central fiber, the media flows in pseudo "cork screw" pattern thus instantaneous diffusion into the tissue may be limited relative to steady state diffusion. This can be seen (**Figure 3.14**) in axial chemical shift images of the pyruvate resonance taken every 5 secs as it flows through the bioreactor. This data suggests that the low levels of lactate signal produced is due to the pyruvate flowing past the tissue. In order to demonstrate that the tissue was viable and capable of producing lactate, 3mM u-^{13}C glucose was supplemented to the infusion media and ^{13}C spectra were acquired with 15 min temporal resolution. The production of lactate in time is demonstrated in **Figure 3.15**. The C_3 lactate resonance appears as a doublet, because of carbon coupling to the adjacent $^{13}C_2$.

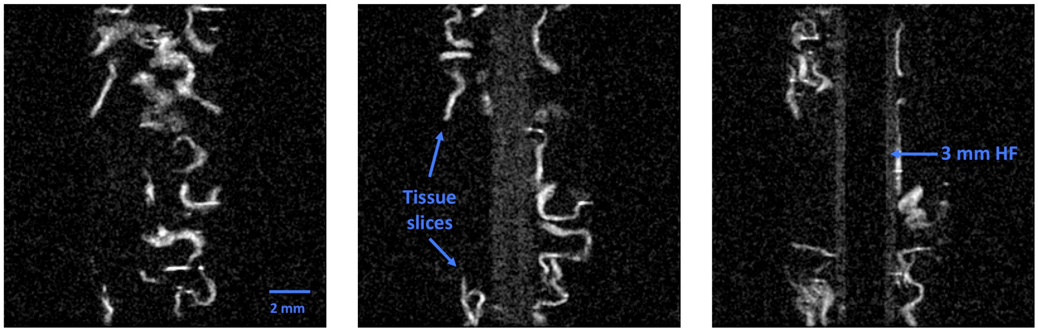

Figure 3.12. ^{1}H diffusion-weighted images show the 250µm tissue slices floating around the inner fiber.

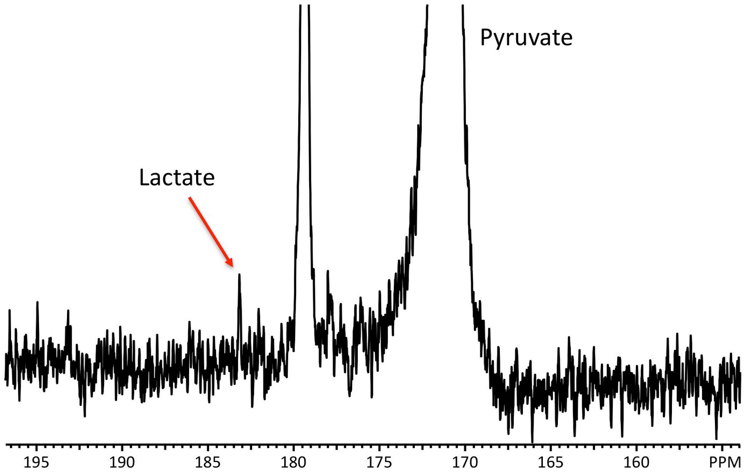

Figure 3.13. ^{13}C summed spectrum after 2mL injection of 20mM pyruvate into the bioreactor flow system. Spectra from 32 to 66 secs (in 3 sec increments) were summed to observe ^{13}C lactate.

The corresponding increase in lactate with time implies a production rate of 2 nmols/min, suggesting the tissue was viable and producing lactate on a level observable in hyperpolarized [1-^{13}C] pyruvate studies, though well below what was seen for JM1 cell experiments (§2.4). Future studies will focus on higher densities of tissue slices to increase overall signal-to-noise and imaging sequences to distinguish the spatial distribution of lactate production in tissue slices.

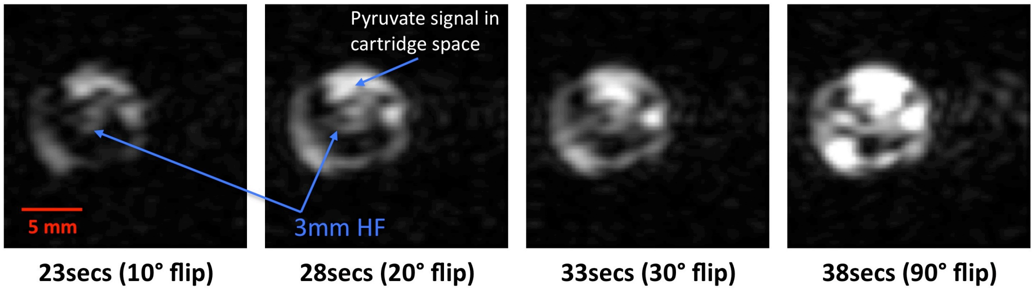

Figure 3.14. ^{13}C EPI images demonstrating the location of pyruvate spatially for these 4 images. Images were acquired after a 2mL infusion of 20mM hyperpolarized pyruvate with an acquisition time of 0.2 secs.

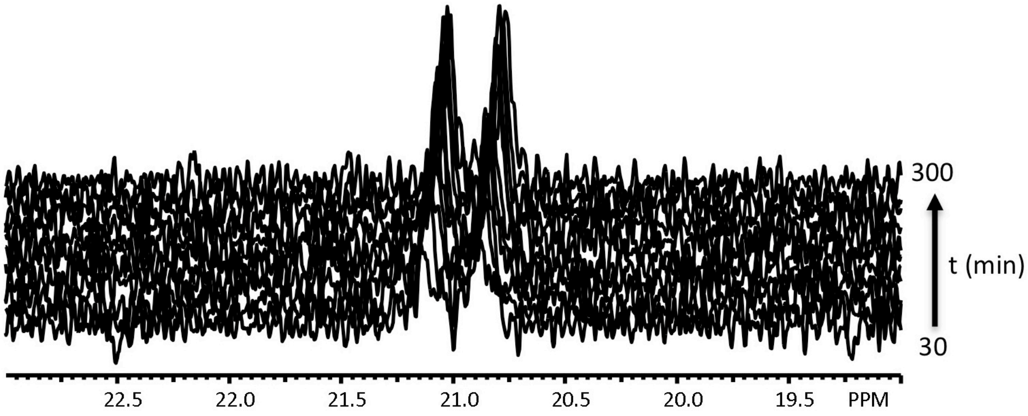

Figure 3.15. ^{13}C spectra acquired after infusion of 3mM u-^{13}C-glucose with 15 min temporal resolution. The C_3 of lactate is shown as it is produced (2nmols/min).

3.4 Prostate Cancer metabolism in Human Biopsies and comparison to Bioreactor Studies

The underlying metabolic state of prostate tissues has been correlated to not only prostate cancer, but also disease progression(Ackerstaff 2001; Albers 2008;

Sreekumar 2009). Prostate tissues, and specifically biopsies are very heterogeneous and metabolic assessments of these tissues results in an ensemble average of the tissue metabolism(Swanson 2003; Swanson 2008; Tessem 2008). This has been generalized for *in vivo* spectroscopic imaging as gross changes in choline containing compounds, polyamines and citrate(Kurhanewicz 1995; Kurhanewicz 2002). Recently, methods have been developed to acquire high-resolution NMR spectra from intact tissues using the high-resolution magic angle spinning (HR-MAS) technique(Swanson 2003; Keshari 2005; Keshari 2005; Keshari 2008; Swanson 2008; Tessem 2008; Albers 2009). This non-destructive approach allows for the metabolism to be assessed and compared to histopathology and genomics in the same piece of tissue(Santos in press). Historically, metabolomic studies of tissues have utilized extracted tissues, most often using Mass Spectrometry, which introduce losses and variability due to the extraction methods used. HR-MAS can address the impact of in vivo MR visibility and local chemical environment since the data is acquired on intact tissues rather than extracts. By comparing metabolite concentrations derived from HR-MAS to histopathology of the same tissue, the impact of tissue heterogeneity on metabolic profiles can be directly assessed.

Shannon's Mutual Information (MI)(Shannon 1948) is a measure of dependence that can outperform the classical and widely used linear measures such as Pearson Correlation (PC) in that it is not influenced by outliers and can detect nonlinear dependencies. Mutual Information has been used successfully for feature selection as a filter-method; that is, it is used for testing each variable to quantify its dependency with a target variable such as "cancer score"(Peng 2005). The purpose of this section is to investigate a non-linear method for clustering metabolites with the pathologic state of the tissue. Using this clustering, a relationship between these different tissue types and the changes in metabolic concentrations can be determined. This will be further compared to the metabolic state of prostate cancer cells (PC3) and tissue slices from patients discussed in the previous section (§3.3).

Human subjects and sample acquisition

This study was approved by our institutional review board (IRB) and informed consent was obtained from all patients. 126 TRUS-guided biopsies were acquired from 99 patients, 27 of which were cancer. Biopsies were acquired as previously described(Tessem 2008). Biopsies were placed in cryovials and snap-frozen on dry ice (<15 secs) immediately after removal from patients. These samples were stored at -80°C and analyzed within 2 weeks of sample acquisition.

HRMAS data acquisition

Prior to NMR studies, 1mm sections of both ends of the sample were removed to eliminate contamination from lipid associated with the longitudinal core through the prostate. Each sample was transferred to a 20μl zirconium rotor, 3.0μL of deuterium oxide and 0.75 wt% sodium-3-trimethylsilylpropionate-2,2,3,3-d_4 (D_2O + TSP) was added as a chemical shift reference, and the rotor was assembled and placed within the magnet. ^1H high-resolution magic angle spinning (HRMAS) spectroscopy was preformed on an 11.7T (500MHz ^1H) Varian INOVA spectrometer equipped with a 4mm gHX nanoprobe (Varian Inc., Palo Alto, CA). Samples were spun at 2250Hz and temperature controlled to 1°C. Fully relaxed spectra were acquired with a TR=4s, 40,000 points, 20,000 Hz spectral width, and 128 transients(Swanson 2003; Keshari 2005; Tessem 2008).

HR-QUEST Processing

Data were quantified using HR-QUEST, a custom version of QUEST(Ratiney 2005) adapted for analysis of short-echo time HRMAS spectra containing 40,000 points. Basis set spectra of metabolites were collected in solution and incorporated into the HR-QUEST fitting routine. Peaks from known macromolecules and unidentified compounds were also included as part of the basis set. HR-QUEST estimated the background signal using an HLSVD algorithm and iterated between fitting the metabolites and modeling the background K times. The concentrations of 17 metabolites were calculated using the ERETIC(Albers 2009) signal as a reference. The choline containing compounds and polyamines were summed to create the two derived variables, total choline and total polyamines, yielding a total of 19 metabolite concentrations.

Histopathology

Post-HRMAS, samples were embedded in Tissue-Tek® optimal cutting temperature (OCT) tissue embedding medium (Fisher, Pittsburg, PA), frozen on dry ice, and sectioned at 5-7μm thickness at -22°C on a Leica CM1850 Cryostat (Leica Microsystems, Wetzlar, Germany). These were then stained with hemotoxylin and eosin (H&E) and assessed by two pathologists. Sample pathology was denoted as percentages of benign glandular, benign stromal and cancer tissue. Samples that included greater than 10% of the core area as confounding pathologies (such as prostatic intraepithelial neoplasia (PIN), benign prostatic hyperplasia (BPH), necrosis, and atrophy) were excluded.

Data Analysis using Mutual Information and Spectral Clustering (Theory and application)

In this work, we measure the dependencies among the features using MI and then apply an appropriate clustering method such as Spectral Clustering(Shi 2000) for partitioning the features into related groups of variables. The use of such a clustering is to find groups that minimize the inter-cluster interactions (or dependencies) while maximizing intra-cluster dependencies.

The entropy(Shannon 1948) of a random variable *X*, denoted *H*(*X*), is a functional of the probability distribution function *P*(*X*), which does not depend on the actual values of *X* but only depends on *P*(*X*). Shannon's entropy is a measure of the uncertainty of a random variable *X* and thus, it quantifies how difficult to predict that variable.

The definition of Shannon's entropy can be written as an expectation:

$$H(X) = -E[\log P(X)] \models -\sum_{x} \left[p(x)\log(p(x)) \right], \qquad [3.19]$$

where *p*(*x*) = *P*(*X*=*x*) is the probability distribution function (more it is the precisely probability mass function for the discrete case but the results are generalizable) of *X*.

Hence the Shannon's entropy is the average amount of information contained in random variable *X*. In other words, it is the uncertainty removed after the actual outcome of *X* is revealed. Mutual Information (denoted as *I* in the formulae) is a measure of mutual dependence of the two variables based on the entropy:

$$I(X;Y) = H(X) + H(Y) - H(X,Y) = \sum_{x}\sum_{y}\left[p(x,y)\log(\frac{p(x,y)}{p(x)\cdot p(y)})\right] \qquad [3.20]$$

where $p(x,y) = P(X=x, Y=y)$.

In other words, $I(X; Y)$ is the expected number of extra bits that must be transmitted to identify *X* and *Y* if they are coded using only their marginal distributions instead of the joint distribution.

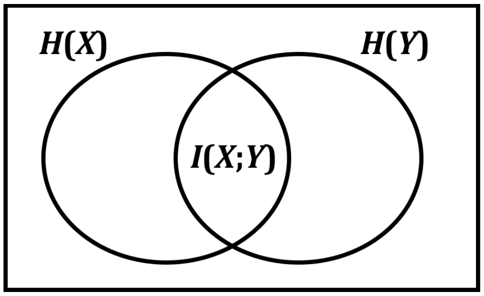

Figure 3.16. Visualization of mutual information with respect to entropy.

One problem with MI is that it is hard to interpret it because, unlike for example squared correlation coefficient, its value is nonzero but not necessarily between 0 and 1. In this work, we report the normalized values for MI as percentage of the entropy of the variables (also known as the coefficient of constraint C_{XY}) calculated simply by dividing the mutual information of variables *X* and *Y* by the entropy of *X*, as in [3.21], which gives the percentage of uncertainty removed about *X* by knowing the state of Y (**Figure 3.16**). Or, equivalently, it gives how much of the entropy (disorder or randomness) of *X* is constrained by fixing *Y*.

$$C_{XY} = \frac{I(X;Y)}{H(X)}. \qquad [3.21]$$

Spectral clustering is a very powerful technique that can be used to group data samples, which cluster in a complex nonlinear way in 2 dimensions(Shi 2000; Rahimi 2004; Filippone 2008). As demonstrated in **Figure 3.17**, data clusters which spiral around each other (left) or that have a circle around a core (right) can be clustered correctly (red and blue) as belonging to different classes. Linear methods such as principal component analysis (PCA) and partial least-squares (PLS) would be incapable of defining these clusters.

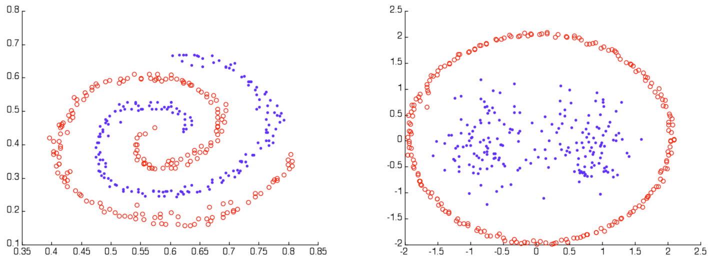

Figure 3.17. Power of spectral clustering. In each figure, the data is shown clustered in the appropriate group (red and blue) after application of the spectral clustering technique. The data (left) is spiraled upon itself or circular (right) and can still be easily distinguished.

Metabolite concentrations from HR-MAS quantification by HR-QUEST

Figure 3.18 demonstrates representative HR-MAS spectra for each of the studied prostate groups (predominantly glandular, stromal and cancer tissue). Typical metabolic signatures such as high levels of citrate (doublet of doublets at 2.62ppm) and polyamines (multiplets at 1.78, 2.10 and 3.11ppm) in the predominantly glandular and high levels of choline containing compounds (singlets choline 3.21ppm, phosphocholine – PC 3.23ppm and glycerophosphocholine – GPC 3.24ppm) in the cancer are readily observed(Ackerstaff 2003; Swanson 2003; Swanson 2008; Tessem 2008). Lactate (doublet, 1.33ppm) and alanine (doublet, 1.49ppm) are also elevated in the cancer sample (**Figure 3.18c**) similar to previously reported HR-MAS spectra of malignant prostate tissues(Tessem 2008).

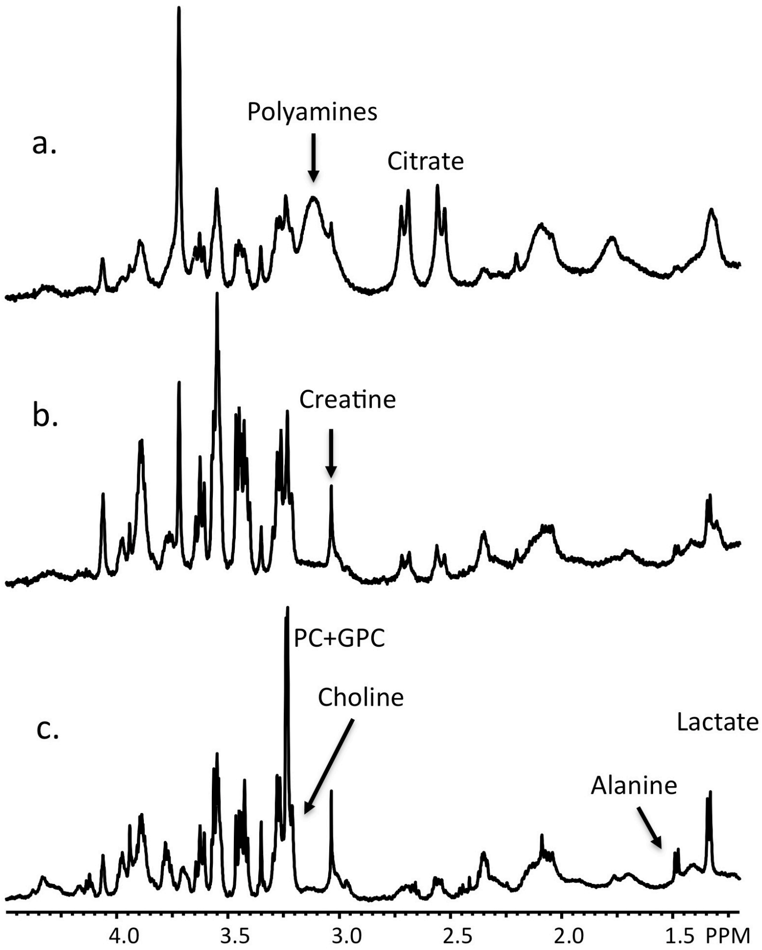

Figure 3.18. Representative ^{1}H HR-MAS spectra of human prostate biopsy samples. Spectra from (a) Predominantly benign glandular (67 yr, 45% glandular, 55% stromal, PSA 5.4ng/mL), (b) predominantly benign stromal (69 yr, 10% glandular, 90% stromal, PSA 3.7ng/mL), (c) cancer containing (71 yr, 3% glandular, 37% stromal, 60% 4+3 Cancer, PSA 6.61ng/mL) demonstrate typical metabolic signatures for each tissue.

For preliminary study, samples were grouped into predominantly glandular (>25% benign glandular), predominantly stromal (≥75% stromal) and cancer (≥5%). Of 126 samples, 99 were histopathologically benign and 27 contained prostate cancer. Benign glandular and stromal samples were on the average 33 ± 5% glandular (n=32) and 82 ± 7% stromal (n=71), respectively. For the 27 cancer samples, 29 ± 20% of the sample contained prostate cancer. For samples in each group, 19 metabolites were quantified as previously described and the distribution of average concentrations is shown in **Figure 3.19**. A Student T-Test was used to compare the cancer samples to the both benign glandular (with p-value P_G) and stromal (with p-value P_S) groups. Concentrations of choline ($P_G = 0.037$, $P_S = 0.042$), phosphocholine (PC, P_G and $P_S < 0.005$), glycerophosphocholine (GPC, P_G and $P_S < 0.005$), total choline (the sum of the choline containing compounds, P_G and $P_S < 0.005$), phosphoethanolamine (PE, $P_G < 0.005$, $P_S = 0.023$), lactate ($P_G = 0.025$), alanine ($P_G = 0.019$), creatine ($P_G = 0.038$), glutamate ($P_G = 0.05$), putrescine ($P_G = 0.05$), spermidine ($P_G = 0.037$) were found to be significantly different when compared to cancer. Interestingly, many metabolites were not significantly different in predominantly benign stromal tissue when compared to those containing cancer. This is potentially due to the heterogeneity of prostate samples; typically a high percentage of the sample contains benign stromal tissue. This

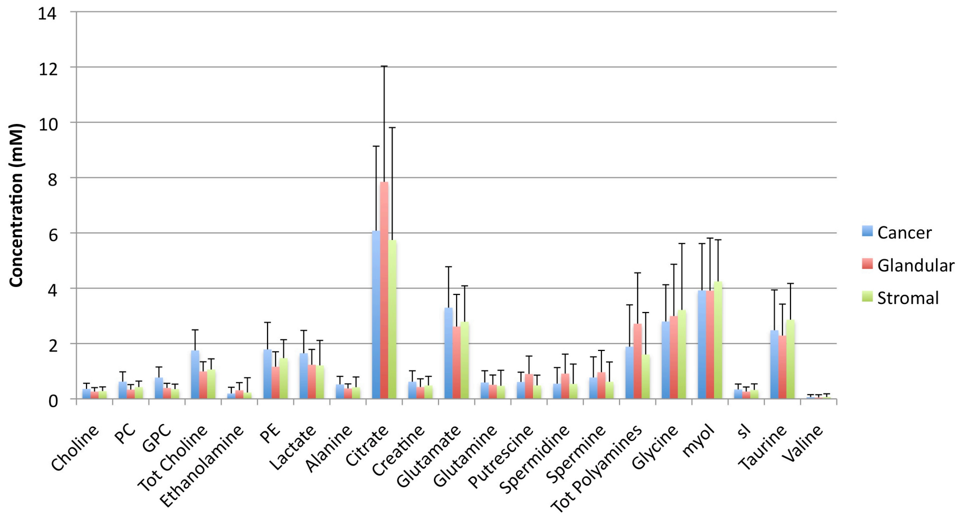

Figure 3.19. Metabolite concentrations for predominantly glandular, stromal and cancer groups.

heterogeneity makes it difficult to determine which metabolic components are specifically from the cancer tissue.

To address the difficulty in separating tissue types and overlapping histopathology, concentrations of each metabolite were treated as individual variables along with the percent of tissue for each pathology. More simply, each biopsy had 19 metabolite variables and 3 pathologic variables (% glandular, stromal and cancer), yielding a 22 variable vector. These vectors were then used as the inputs for the mutual information and spectral clustering algorithm. **Figure 3.20** demonstrates the output of the algorithm, with spatial arrangement as a function of correlation. The metabolites spermine, spermidine, total polyamines (a sum of all of the polyamines) and citrate are highly correlated with benign glandular tissue. This relationship between polyamines and citrate is a classic MR biomarker of benign

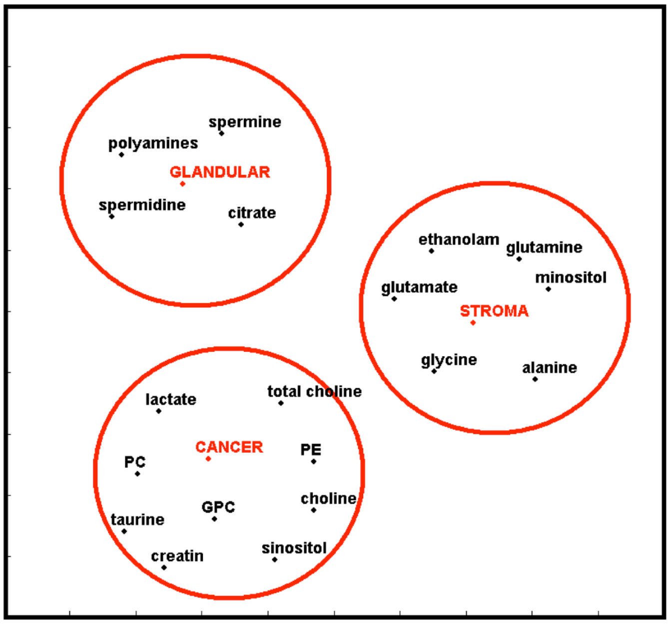

Figure 3.20. Spectral clustering of 126 biopsies. 22 variables (19 metabolites and 3 pathology scores) were used based on statistically significant pairwise mutual information ($P \leq 0.01$). 3 clusters are indicated by the red circles.

prostate metabolism(Kurhanewicz 1995; Kurhanewicz 2002; Costello 2005). Ethanolamine, glutamate, glutamine, *myo*-inositol, glycine and alanine cluster with stromal tissue. Both glutamate and glutamine cluster with stroma, which is in good agreement with the biochemistry. Typically glutamine is derived from glutamate and surrounding ammonia. Glutamate is also in equilibrium with α-ketoglutarate in the TCA cycle, and high concentrations are representative of high levels of aerobic metabolism in the mitochondria. In comparison to glandular tissue, which shunts TCA at citrate for the purposes of secreting high concentrations of citrate into the prostatic secretions, TCA metabolism is conserved and thus glutamate is resident at high steady state concentrations. It is possible that the correlation between *myo*-inositol and stromal tissue may be an indicator of stromal signaling. This has been a topic of investigation in prostate cell line studies, because benign epithelial cells tend to dedifferentiate back into a basal cell without the signaling of surrounding stromal tissue(Goo 2005). Correlation between stromal tissue and glycine and alanine are not as straightforward and require further investigation.

Interestingly, the cancer variable correlates to concentrations of choline, PC, GPC, total choline (the sum of all the choline containing compounds), PE, creatine, *scyllo*-inositol, taurine and lactate. The choline containing compounds are a hallmark of rapidly dividing cells and thus cancer(Ackerstaff 2003; Iorio 2005). Lactate has also been correlated to malignant prostate tissues in previous HR-MAS studies of human biopsy tissues (Tessem 2008), but this is the first objective classification. Moreover, lactate is very interesting because of its relationship to previously mentioned hyperpolarized carbon studies (§2.3 and 3.3) and those conducted *in vivo*(Chen 2007; Albers 2008; Chen 2008).

Hyperpolarized ^{13}C measurements made in prostate tissue slices as well as prostate cancer cell lines demonstrate high levels of real time LDH activity. The observed conversion of pyruvate label to lactate is a function of enzyme activity, isoenzyme pattern, concentration of substrate, availability as well as transport. It is possible that a combination of these changes leads to both differences in steady state concentration and real time measurements. Further investigation into the mechanism of these changes by proteomic methods would be needed to determine which variable is most responsible for the steady state and dynamic changes.

Chapter 4: Hyperpolarized Metabolic Tracer and Probe Development

4.1 Secondary labeling by Acetic Anhydride and extension to short peptides

Recent development of techniques to retain highly polarized spins in solution via dynamic nuclear polarization (DNP) has enabled ^{13}C NMR spectroscopy and MR spectroscopic imaging studies with very high signal to noise in short acquisition times(Ardenkjaer-Larsen 2003; Golman 2006). Generally, the technique requires polarization of a low molecular-weight ^{13}C labeled chemical probe in a highly concentrated sample, for example [1-^{13}C] pyruvic acid or ^{13}C-urea(Mayer 2006; Kohler 2007; Merritt 2007). For molecules having limited solubility, crystalline properties at low temperature, or high molecular weights, the hyperpolarization technique may not provide sufficient polarization for *in vitro* or *in vivo* applications. For molecules with limited solubility, the polarization rate can also be prohibitively long. To address this limitation, this study was designed to develop a method of "secondary hyperpolarization", whereby a reactive molecule that hyperpolarizes well could be used to chemically 'tag' biomolecules of interest. Recently, chemical derivatization of amines in biofluids with [1,1-^{13}C] acetic anhydride, and their 500 MHz ^{13}C NMR spectra was reported(Shanaiah 2007). In this project, the secondary hyperpolarization approach was applied using pre-polarized [1,1-^{13}C] acetic anhydride and rapid chemical reactions to provide high SNR NMR spectra of amino acid derivatives and other biomolecules.

This secondary hyperpolarization technique could be of great value to the emerging field of metabolomics or metabolic profiling, where molecular processes in the living cell are assessed, and the chemical content of biofluids resolved(Lindon 2004; Wang 2004; Bollard 2005). Currently, only a limited number of biomarkers are used in clinical practice. These biomarkers include the levels of an expressed protein in health or disease, for example CA-121 expressed in ovarian cancer, or of a given metabolite concentration in biofluids, for example catecholamines found in the urine of patients with pheochromocytoma(Bast 2005; Young 2007). Increasingly, medical diagnostics will incorporate fast methods of obtaining a patient's disease profile, through genomic, proteomic and metabolic evaluations. Effective screening methods could allow earlier disease identification and treatment and improve outcomes. The most established technologies in this field are NMR and mass spectroscopy, both of which have been used to identify errors in metabolism and the accumulation of specific metabolites in disease(Pauling 1971; Gartland 1991). Very recently, DNP NMR has been used to obtain metabolic data with very short acquisition times, in animal and cell culture models of human disease(Chen 2007; Day 2007; Albers 2008; Keshari 2008). Most importantly, this data can be acquired in seconds at high spatial resolution. This improved speed of acquisition is clearly of benefit in the development of medical diagnostics, with information often needed quickly in acutely ill patients.

The goal of this project was to combine the remarkable NMR signal enhancement provided by DNP with the reactivity and good polarization characteristics of [1,1-^{13}C] acetic anhydride to resolve a mixture of secondarily hyperpolarized N-acetylated amino acid adducts in aqueous solution in a matter of seconds. Additionally, the utility of this secondary hyperpolarization technique was explored in the context of other important biomolecules that may not be well polarized using direct DNP methods. These molecules can then be used *in vivo* to explore mechanisms that were previously inaccessible by conventional MR imaging modalities.

Polarization of [1,1-^{13}C]-Acetic anhydride

Neat samples containing 10μL of [1,1-^{13}C] acetic anhydride (1.06 x 10^{-4} mol) (Isotec, Miamisburg, OH) containing 15mM Finland trityl radical OX076 (Oxford Instruments, Abingdon, UK) were polarized at 94.106 MHz and 1.2-1.4°K), for 30 minutes and subsequently dissolved in 2.5mL of anhydrous 1,4 dioxane (Sigma-Aldrich) using a Hypersense DNP polarizer (Oxford Instrument, Abingdon, UK). The hyperpolarized [1,1-^{13}C] acetic anhydride/dioxane solution was subsequently injected from the DNP polarizer directly into the amino acid solutions (described in the following sections), manually mixed in a 500cc teardrop flask, and injected using a 5cc syringe into a previously shimmed 10mm NMR tube into at 37°C. This process required approximately 10 seconds. Percentage polarizations were quantified in solution by measuring the signal enhancement obtained by DNP polarization compared to the signal at thermal equilibrium(van de Ven 1995).

Secondary Hyperpolarization of amino-acid mixtures with hyperpolarized [1,1-^{13}C]-Acetic anhydride

Initial studies (N=3) involved mixing the dissolution solution containing dioxane and hyperpolarized [1,1-^{13}C]-acetic anhydride with 3 mL of a buffered (100mM phosphate, 0.3 mM EDTA pH = 7.8) solution of amino acids Glycine (Gly), Serine (1), Valine (Val), Leucine (Leu), and Alanine (Ala) at 3.5 mM each, or 17.5mM total amino acid concentration. A two-fold excess of acetic anhydride with respect to the total amino acid concentration was used in all labeling studies. The final pH of the resulting solutions was ≈ 5.5 (5.55, 5.54, and 5.61 respectively). To confirm the chemical shifts of each of the acetylated amino acids, the same hyperpolarized experiment was performed for each amino acid individually at a concentration of 17.5mM. To determine whether or not this technique could produce reasonable SNR for a solution containing amino acids at physiologic concentrations, a buffered, aqueous solution containing 70μM amino acids (Gly, Ser, Val, Leu, Ala) was acetylated under the same conditions used for the higher amino acid concentration studies. The peak area to noise for the acetyl carbon of the acetylated amino acids was measured in triplicate studies. The final pH of the reaction mixtures was higher (pH ≈ 7.33) than that observed for the higher concentration studies due to the lower concentration of hyperpolarized [1,1-^{13}C]-acetic anhydride used and subsequent lower production of acetic acid.

Secondary Polarizarion of glycine, diglycine, triglycine

A second set of labeling experiments (N=3) using hyperpolarized [1,1-^{13}C]-acetic anhydride was conducted with a chemically similar set of substrates, namely glycine (MW=75.07), diglycine (MW=132.12) and triglycine (MW=191.14). The reaction conditions in these studies were identical to those described for the labelling of the mixture of amino acids (17.5mM). The pH's of the resulting solutions were ≈ 5.5.

Secondary hyperpolarization of N-acetyl lysine, and C-terminus of α-melanocyte stimulating hormone (α-MSH)

The reaction conditions in these studies were identical to those described for the labeling of the mixture of amino acids, except for mixing a six fold excess of the hyperpolarized [1,1-^{13}C] acetic anhydride/dioxane solution with 5 mM N-acetyl lysine, and 5 mM α-melanocyte stimulating hormone (α-MSH), resulting in a final reaction solution pH of 6.0.

Secondary hyperpolarization of N-acetyl cysteine

20μL of [1,1-^{13}C] acetic anhydride (2.12 x 10^{-4} mol) were polarized using the HyperSense DNP polarizer at 94.106 MHz for 30 minutes. Five mL of the following dissolution media were used: 200 mM cysteine, 150 mM NaOH, 0.3 mM EDTA. The final concentration of cysteine using this volume corresponds to roughly 5-fold excess of cysteine with respect to acetic anhydride with a resulting pH of 6.8.

Secondary hyperpolarization of Arg-Gly-Asp (RGD)

6.2μL of [1,1-^{13}C] acetic anhydride preparation (2.12 x 10^{-4} mol) were polarized using the HyperSense DNP polarizer at 94.106 MHz for 1 hour. Five mL of the following dissolution media were used: 6.1μL of 10N NaOH, 21mg of RGD peptide (12mM), 0.3mM EDTA in H_2O. This resulted in equimolar concentrations of labeled acetic anhydride and RGD. In a second experiment with analogous parameters, 6.2μL of [d_6-1,1-^{13}C] acetic anhydride (2.12 x 10^{-4} mol) was polarized.

This preparation was then applied in a larger volume to murine model of prostate cancer (TRAMP) to assess the distribution of signal *in vivo*. In the murine case, 30μL of [d_6-1,1-^{13}C] acetic anhydride were polarized and reacted with 100mg of RGD peptide in a 4mL dissolution similar to *ex vivo* studies. 350μL of the dissolution was injected into a TRAMP mouse (72mM RGD) and 3D spectra was acquired using methods previously described(Albers 2008) on a 3T GE Signa™ scanner (GE Healthcare, Waukesha, WI) equipped with the MNS (multinuclear spectroscopy) hardware package.

Methods for ex vivo Hyperpolarized ^{13}C Spectroscopic Studies

All NMR studies were performed on a 11.7T Varian INOVA spectrometer (125MHz ^{13}C, Varian Instruments) using a 10mm ^{15}N/^{31}P/^{13}C triple-tuned direct detect probe. For the acquisition of hyperpolarized ^{13}C spectra of the hyperpolarized acetylated amino acids eighty proton-decoupled (WALTZ-16, 9000 Hz bandwidth, decoupling during acquisition only) pulse and acquire hyperpolarized ^{13}C NMR spectra (1 average, spectral window = 4000 Hz, number of points= 16000, TR=3.5s, acq time= 2s, total acq time = 2 min 55s) were acquired every 3 sec using a 5° pulse. For the low concentration amino acid secondary hyperpolarization study, a single 90° pulse was used to acquired the hyperpolarized ^{13}C Spectrum. Spin-lattice (T_1) relaxation times were determined by performing a mono-exponential fit to the signal decay curve of the hyperpolarized compounds. In all cases the r^2 value for the fit was > 0.997 where r = the Pearson product moment correlation coefficient. All spectral measurements were collected at ≈ 37°C.

Following each hyperpolarized experiment; a small quantity of Magnevist Gd-chelate (Bayer Healthcare Pharmaceuticals, Inc.) was added to the reaction solution, resulting a final Magnevist concentration of 5mM. A proton decoupled ^{13}C thermal spectrum was acquired using the same acquisition parameters used for the hyperpolarized studies except for a 90° pulse and obtaining 256 averages in order to calculate signal enhancements and reaction yields. A repetition time of 3 seconds was > 3 T_1's since the T_1 of acetic acid and the acetyl-amino acids were determined to be less than 1s after addition of 5mM Magnevist. Signal enhancements due to hyperpolarization were calculated by integrating acetyl-amino acid peaks in the first spectrum of the hyperpolarized dynamic experiment, and comparing these to the corresponding peaks in the thermal spectrum, accounting for differences in gain, tip angle, and the number of transients obtained. Since the reaction goes to completion (all of the acetic anhydride was converted to either acetic acid or the acetylated amino acids), yields were calculated using the acetic acid peak in fully relaxed thermal spectra as an internal standard.

Secondary hyperpolarization of amino-acid mixtures with hyperpolarized [1,1-13C]-Acetic anhydride

[1,1-^{13}C] acetic anhydride is a good substrate for DNP hyperpolarization since it is a liquid at room temperature that dissolves the trityl radical, forms a glass at 1.4°K, and reaches a maximum solution state polarization in 30 minutes yielding 5.9% polarization. To avoid premature reaction of the hyperpolarized acetic anhydride during dissolution, initial studies used 1,4 dioxane as the dissolution media. Acetic anhydride was stable to dissolution conditions in this solvent, with only the hyperpolarized acetyl carbonyls observed in the ^{13}C spectrum. At 11.7T and 37°C, the calculated T_1 for hyperpolarized carbonyl of [1,1-^{13}C] acetic anhydride in dioxane was 33.9 sec.

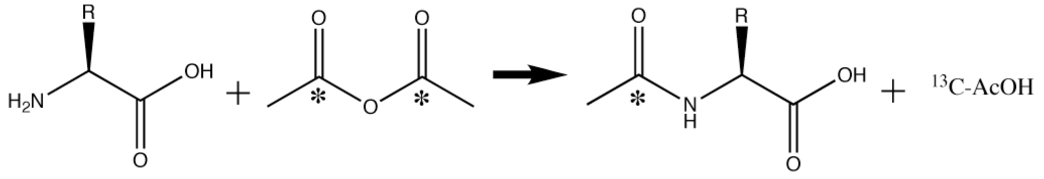

Figure 4.1. General strategy for secondary hyperpolarization of amino acids using pre-polarized [1,1-^{13}C] acetic anhydride.

In a mixed dioxane/aqueous solvent, derivatization of amines with hyperpolarized [1,1-^{13}C] acetic anhydride takes place rapidly, prior to acquisition of the first hyperpolarized spectrum, to form the corresponding acetylated products as shown in **Figure 4.1**. This method takes advantage of the preferential reaction of acetic anhydride with amine nucleophiles, which occurs much more rapidly than hydrolysis. In triplicate studies, it was also determined that a mixture of hyperpolarized [1-^{13}C] N-acetylated Gly, Ser, Val, Leu, and Ala could be well resolved with excellent signal-to-noise, in a single acquisition (**Figure 4.2**). The ability to obtain sufficient spectral resolution to resolve the amino acid mixture required stabilizing the reaction solution temperature and pre-shimming the 10mm NMR probe using the same mixture of amino acids prior to acquiring the hyperpolarized

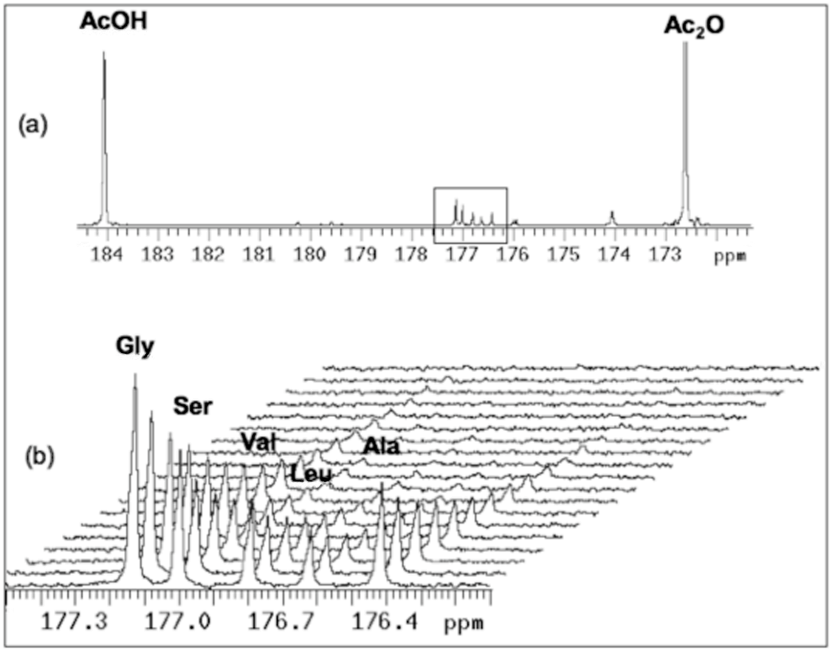

Figure 4.2. Hyperpolarized spectrum obtained when a buffered solution (100mM phosphate, pH=7.8) containing the amino acids gly, ser, val, leu, ala (3.5 mM/ amino acid) is reacted with a two-fold excess of hyperpolarized acetic anhydride. (a) Full spectrum (t=0) including large peaks corresponding to unreacted acetic anhydride and hydrolysis product acetic acid, as well as acetylated amino acid products (outlined). (b) Dynamic hyperpolarized spectrum with resolved acetylated amino acid products.

^{13}C data. By the time of the first hyperpolarized spectrum (≈11 sec after mixing), the acetylation reaction had already gone to completion, since the hyperpolarized [1-^{13}C] N-acetylated amino acid peak areas were at a maximum at t_0 and decayed due to T_1 relaxation (**Figure 4.2b**). The calculated T_1's for the acetylated amino acids correlated with their corresponding molecular weights with glycine and alanine having the longest T_1 (14.7 ± 0.4s) and leucine having the shortest T_1 (8.9± 0.6 s, **Table 4.1**).

Since there was a two-fold excess of acetic anhydride relative to the amino acids, there was a large residual acetic anhydride peak in the hyperpolarized ^{13}C spectra as well as a large acetic acid peak due to hydrolysis. There was an additional doublet upfield from acetyl-alanine, at 176.0ppm, that was present in control experiments using only an aqueous buffered solution, without any amine nucleophiles present. Therefore this additional doublet most likely represents a breakdown product of the hyperpolarized [1,1-^{13}C] acetic anhydride in aqueous solution.

Table 4.1. Secondarily Acetylated Amino Acids

Product	Chemical Shift (ppm)	T_1 (s)	Yield (%)	Enhancement
n-acteyl-glycine	177.13	14.7 ± 0.4	91.7 ± 4.5	1391 ± 220
n-acetyl-serine	177.00	10.9 ± 0.2	97.0 ± 3.0	775 ± 86
n-acteyl-valine	176.79	10.0 ± 0.2	93.3 ± 2.3	551 ± 43
n-acetyl-leucine	176.62	8.9 ± 0.6	85.0 ± 4.6	412 ± 70
n-acetyl-alanine	176.41	14.7 ± 0.4	82.0 ± 3.6	654 ± 96

Table X. Chemical shifts, spin-lattice relaxation constants (T_1), %yield, and hyperpolarized signal enhancement for amino acid mixture data (3.5mM/ amino acid). Data was obtained in triplicate, with averages reported and the corresponding standard deviations indicated. Chemical shifts were referenced to acetic anhydride (172.60 ppm).

A representative fully relaxed thermal spectrum used to calculate the hyperpolarized signal enhancement factors is shown in **Figure 4.3**. Unlike the hyperpolarized acetylated amino acid spectra, in which different amino acids had significantly different peak areas (**Figure 4.2b**), all the amino acids had approximately equal peak areas in the fully-relaxed thermal spectra. Signal enhancement in the first hyperpolarized spectrum reflected differences in T_1 signal decay during the approximately 11 seconds required for mixing, temperature equilibration and insertion into the NMR tube. N-acetyl glycine, with the longest T_1 demonstrated the largest signal enhancement (1.4×10^3) and leucine, with the shortest T_1, demonstrated the smallest enhancement (4.1×10^2). Acetyl-alanine was slightly anomalous in this respect demonstrating a lower peak area in the dynamic hyperpolarized spectrum despite its longer measured T_1.

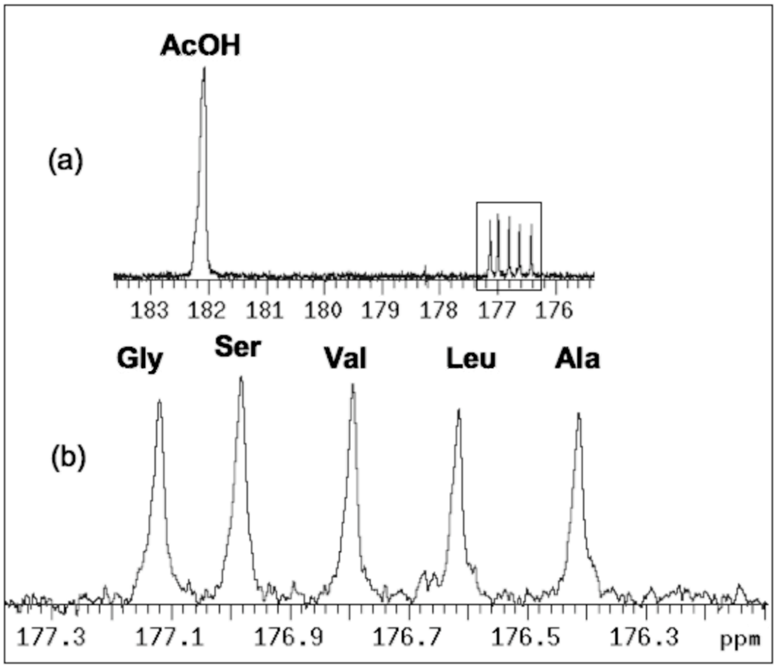

Figure 4.3. Thermal spectrum corresponding to the hyperpolarized data presented in Figure X. (a) After addition of Magnevist Gd-chelate to a final concentration of 5 mM, the only peaks observed correspond to [1-^{13}C]-AcOH and the previously observed acetylated amino acid products (outlined). (b) Expanded region of interest in the ^{13}C spectrum.

As anticipated, the yields for the acetylation reaction were high, ranging from 82 to 97 percent with excellent reproducibility between the replicate studies (**Table 4.1**), and were similar to those published previously for the reaction of amino acids and acetic anhydride in aqueous media(Shanaiah 2007).

Even at physiologic concentrations of amino acids (70μM) excellent signal to noise hyperpolarized ^{13}C spectra can be acquire in a single acquistion. Specifically, the acetyl carbonyl of acetylated- glycine, serine, valine, leucine, and alanine had a peak area to noise of 43.1 ± 8.5, 27.8 ± 5.9, 16.0 ± 4.6, 9.1 ± 3.8, and 13.5 ± 3.1, respectively. The relative peak areas in the hyperpolarized spectrum were the same as in the higher amino acid concentration study (**Figure 4.2b**), i.e. scaled by their T_1 relaxation rates, however the chemical shifts were slightly different due to the higher pH of the reaction solution due less acetic acid being produced.

Secondary Hyperpolarization of glycine, diglycine, triglycine

A second set of experiments focused on a chemically similar set of substrates of increasing molecular weight, namely glycine, diglycine and triglycine in order to assess the effect of molecular size on T_1. A representative data set is depicted in **Figure 4.4**, which demonstrates peaks corresponding to [1-^{13}C]-acetic acid, ^{13}C-acetylglycine, and [1,1-^{13}C] acetic anhydride. The data for glycine confirmed that the calculated T_1 value correlated well with that seen in the previous, mixed amino-acid experiment. The T_1 relaxation time for diglycine was 35% less than glycine and the T_1 triglycine was 9% less than the diglycine. Results of this are summarized in **Table 4.2**.

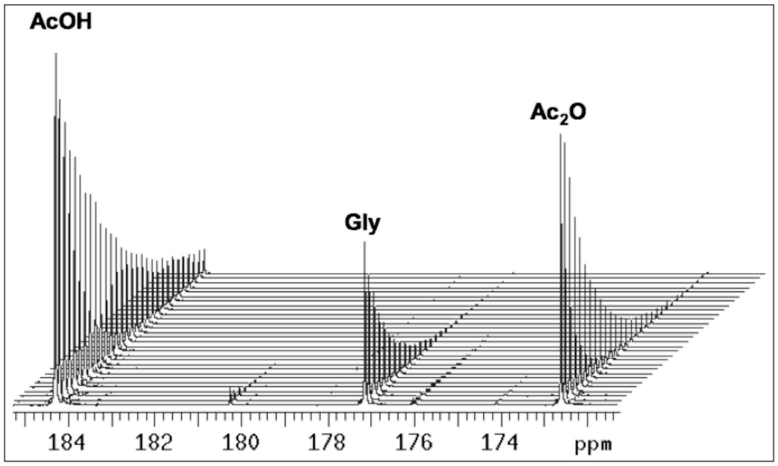

Figure 4.4. Sample dynamic data set for reaction of hyperpolarized (1,1-13C) acetic anhydride with glycine

Table 4.2. Secondarily Acetylated Glycine, Diglycine and Triglycine

Product	Chemical Shift (ppm)	T_1 (s)
n-acteyl-glycine	177.13	15.0 ± 0.5
n-acetyl-diglycine	178.05	9.8 ± 1.2
n-acteyl-triglycine	178.25	8.5 ± 0.2

Table 4.2. Chemical shifts and spin-lattice relaxation constants for glycine peptides. In each case the average T_1 is reported with the standard deviation. For all experiments, a twofold excess of hyperpolarized [1,1-^{13}C] acetic anhydride was applied to a buffered solution (100mM phosphate, pH=7.8) of the corresponding glycine peptide at 17.5 mM.

Secondary hyperpolarization of N-acetyl lysine and C-terminus of α-melanocyte stimulating hormone (α-MSH)

Peptides bearing lysine side-chains represent an excellent opportunity to label larger macromolecular structures. To investigate this application, we used hyperpolarized [1,1-^{13}C] acetic anhydride to label an N-acetylated version of lysine, with its nucleophilic side-chain amine, as well as a short peptide corresponding to the C-terminus of α-melanocyte stimulating hormone (α-MSH). N-acetyl lysine and N-acetyl(Wang 2004; Bast 2005) α-MSH have molecular weights of 188.23g/mol and 383.5 g/mol respectively. The structure of this tripeptide is shown in **Figure 4.5**. Following secondary labeling via the hyperpolarized anhydride, the acetyl carbonyl of both compounds were found to have the same chemical shift (177.11ppm), and the T_1's of the acetyl carbonyls scaled with molecular weight, with N-acetyl lysine having and N-acetyl(Wang 2004; Bast 2005) α-MSH having T_1's of 12.2 and 9.5 seconds.

Secondary hyperpolarization of N-acetylcysteine

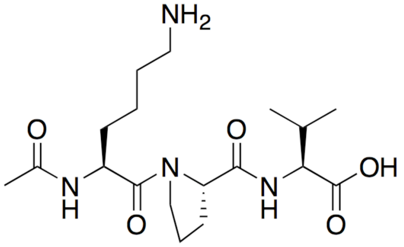

Figure 4.5. Chemical structure of N-acetyl MSH, a short peptide corresponding to the C-terminus of a-MSH. Only the lysine side-chain is available for acetylation

For *in vivo* applications it will be necessary to demonstrate that a hyperpolarized, anhydride-depleted, aqueous solution of a molecule of interest could be generated using this technique. Instead of using toxic dioxane as a dissolution media, a basic solution of cysteine was used in order to generate N-acetyl cysteine during the dissolution process. **Figure 4.6** demonstrates successful secondary labeling of this small molecular weight drug. This experiment also demonstrated the ability to perform the secondary hyperpolarization in aqueous solution during dissolution in the Hypersense® DNP polarizer. Moreover, the reaction went to completion as evidenced by the presence of N-acetylcysteine (172.6ppm) and acetic acid, and absence of acetic anhydride in the hyperpolarized ^{13}C spectrum. In the process of acetylation of the amine, the reaction also yielded acetylation of the cysteine thiol at 202ppm (**Figure 4.6**). This was minor in comparison to the amine and likely a result of the changing pH with generation of acetic acid. As acetic acid is generated and the pH changes, the thiol becomes a better nucleophile and thus is acetylated.

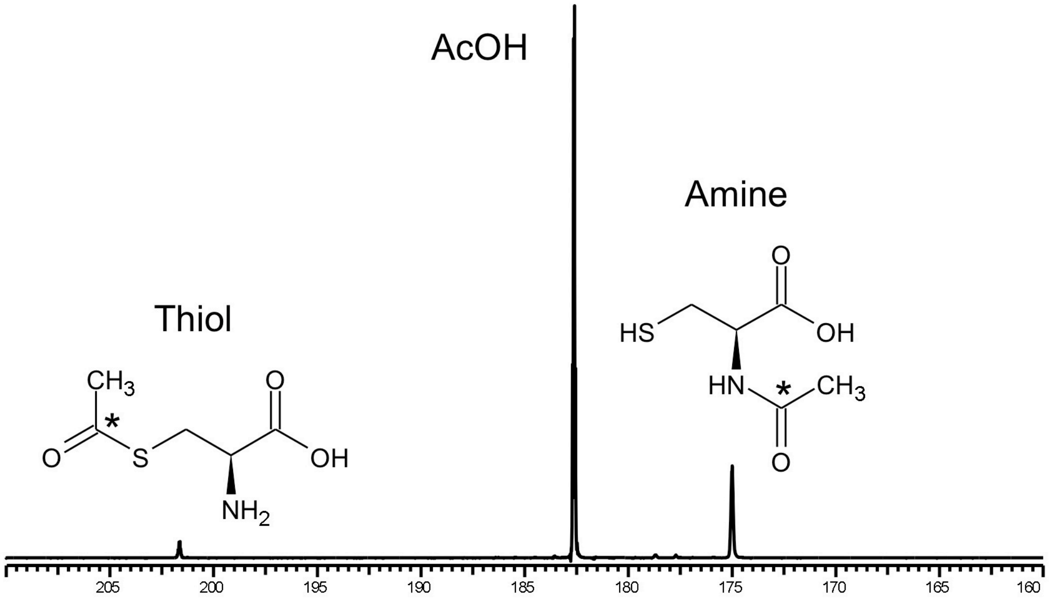

Figure 4.6. Generation of hyperpolarized acetylcysteine by secondary labeling. Note the total absence of Ac_2O at 172.6 ppm, indicating that the reaction has been successfully driven to completion. This also yeiled the acetylation of the thiol at 202ppm. Integration of these resonances yields a relative acetylation of ~5:1 for the amine:thiol.

Secondary polarization of Arg-Gly-Asp (RGD) ex vivo and in vivo

As was shown in studies of n-acteyl lysine, cysteine and α-MSH small molecules and peptides can be labeled via [1,1-^{13}C] acetic anhydride. These molecules can also be labeled close to chemical completion, making them applicable as *in vivo* probes. The tripeptide Arginine-Glycine-Aspartate (RGD, MW 346.34) is another such peptide with a important *in vivo* application, binding cell surface integrins(Ruoslahti 1996) which has been shown to upregulated in cancer (Edick 2007; Goel 2008). The structure, shown in **Figure 4.7a**, demonstrates the primary amine of Arginine as the site for acetylation. Acetylation of RGD was accomplished in a basic solution containing the peptide during dissolution of the hyperpolarized acetic anhydride. The first pulse of the experiment (**Figure 4.7c**) demonstrates the signal of the acetylated RGD at 11.7T, with T_1 of ~7s. In an attempt to increase the T_1 of acetylated RGD, the aceytlation was carried out using per-deuterated [d_6-1,1-

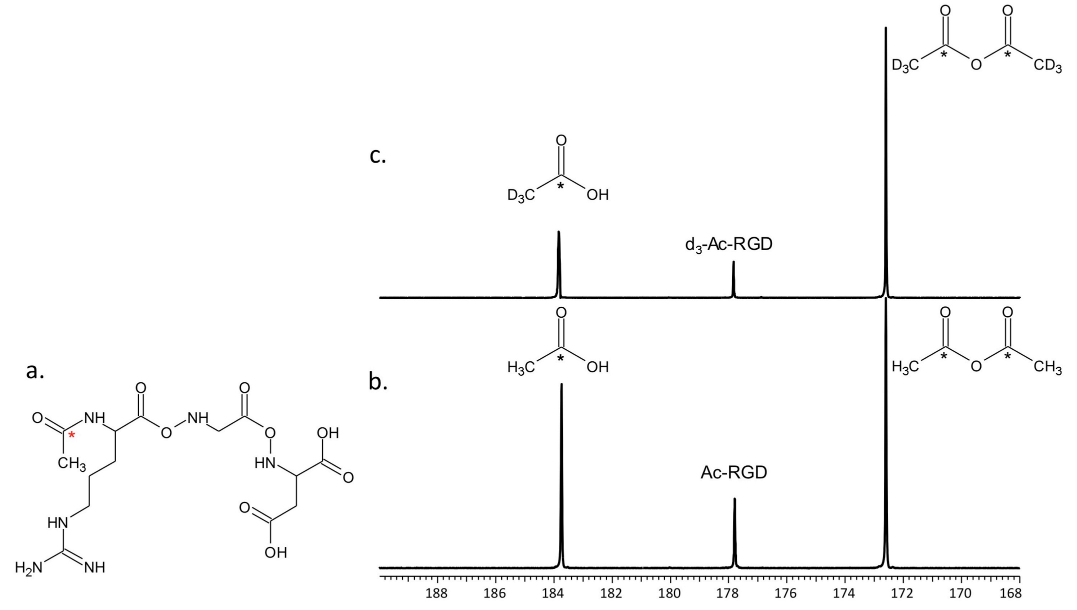

Figure 4.7. (a) Structure of Arg-Gly-Asp demonstrating the site of acetylation. Generation of hyperpolarized Ac-RGD (b) and d_3-Ac-RGD (c).

^{13}C] acetic anhydride (**Figure 4.7b**). This yielded a T_1 of ~8s, only slightly longer than the protonated version. However, at 3T, deuteration significantly lengthens the acetylated RGD as compared to the protonated compound (to 30 secs). In the presence of 1.1 equivalents of base, only the primary amine was acetylated. When the base concentration was increased (2 equivalents) the side-chain amine of arginine was also acetylated, therefore 1.1 equivalents of base is necessary for single acetylation. [d_6-1,1-^{13}C] acetic anhydride was then used to acetylate RGD and 350μL of dissolution was injected into a transgenic murine model of prostate cancer (TRAMP) mouse (**Figure 4.8**). Spectra from a representative axial slices (**Figure 4.8b**) and corresponding axial T_2-weighted image (**Figure 4.8a**) through the TRAMP tumor and surrounding benign tissues demonstrated the bio-distribution of signal for the RGD peptide. There was some overlap of [1-^{13}C] lactate (183ppm) and

^{13}C-urea (normally 163ppm, but here wrapped to the position 178ppm) from the syringe phantoms with the large [1-^{13}C] acetate resonance generated in the acetylation reaction. However, a dramatic loss of signal from the acetylated RGD peptide in tumor voxels as compared to voxels containing benign tissue was clearly observed.

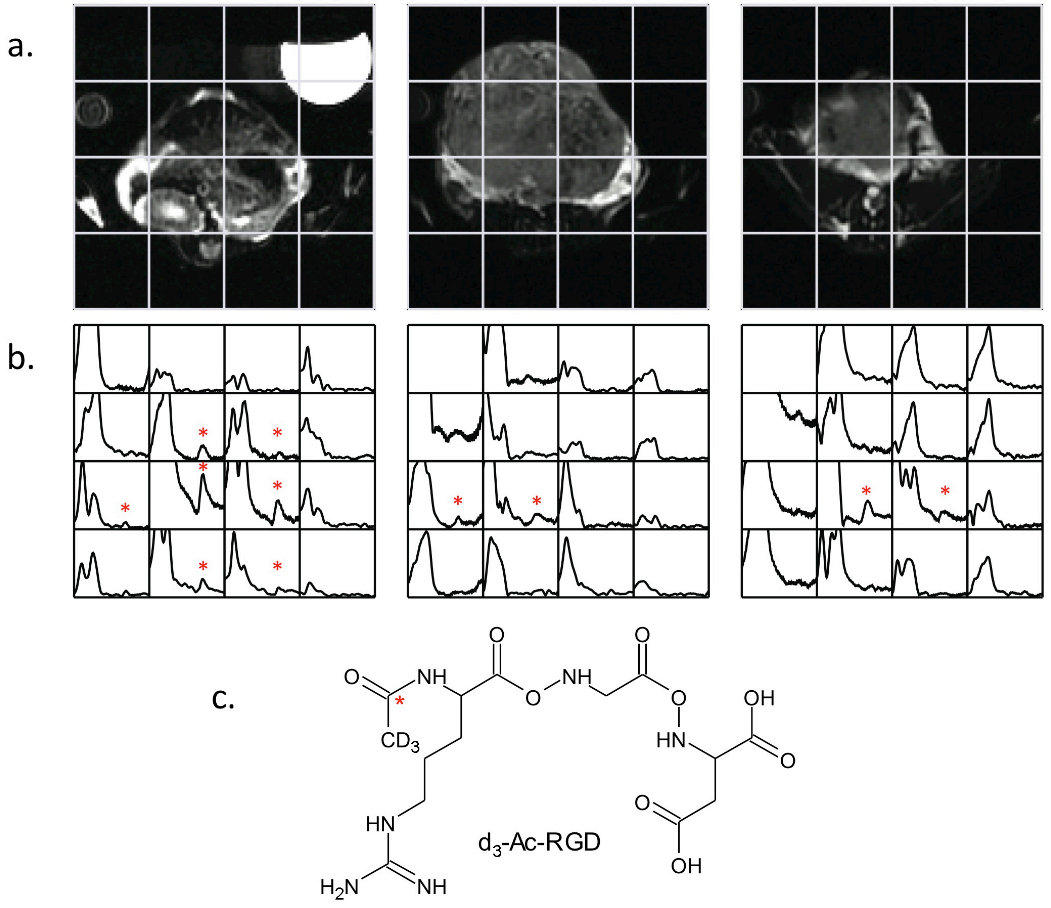

Figure 4.8. (a) T_2-weighted images of a TRAMP mouse and corresponding spectra (b) demonstrating the in vivo resonance of d_3-Ac-RGD. The structure of the d_3-Ac-RGD (c) is also shown for reference.

These studies demonstrated the feasibility of a "secondary hyperpolarization" approach combining the remarkable NMR signal enhancement provided by DNP with the high reactivity of [1,1-^{13}C] acetic anhydride with amino acids to perform rapid metabolic analyses of amino acid mixtures and to hyperpolarize biomolecules of interest. [1,1-^{13}C] acetic anhydride is an excellent substrate for DNP hyperpolarization since it is well polarized (5.9%) in 30 minutes and has a relatively long T_1 relaxation time (33.9 sec at 11.7T and 37°C). This approach also takes advantage of the preferential reaction of acetic anhydride with amine nucleophiles, which occurs much more rapidly than hydrolysis, as was evidenced by the reaction being complete by the first hyperpolarized ^{13}C spectra acquired 11 seconds after mixing the reactants.

This study demonstrated that this secondary hyperpolarization approach could be used to reproducibly and near-quantitatively resolve a mixture of amino acids at physiologic concentrations in a single acquisition. The amino acid acetyl carbonyl resonances demonstrated excellent signal-to-noise ratios (SNR) ranging 43 to 9. This difference in SNR was due to T_1 relaxation during the 11 second delay between the mixing of the reactants and the NMR experiment. This delay was required to mix the reactants outside of the spectrometer in order to minimize air bubbles and allow for temperature equilibration, as well as obtain sufficient magnetic field homogeneity to resolve the N-acetyl carbonyls of the amino acids that had very similar chemical shifts. The secondary hyperpolarization approach also allows the calculation of the T_1 relaxation of the products providing a means to correct for T_1 necessary for quantification of the spectral results.

A recent study demonstrated that using high pressure liquid chromatography techniques, the hyperpolarized solution can be injected directly into the NMR spectrometer with good magnetic field homogeneity allowing for good quality spectra to be obtained seconds after injection(Bowen 2008). This study suggests that in the near future, the mixing of reactants involved in a secondary hyperpolarization could be performed directly in the NMR spectrometer. This would provide a way to capitalize on the full signal-to-noise enhancement provided by DNP and negate the need for T_1 corrections.

The secondary hyperpolarization approach also benefits the study of biologically interesting compounds that either hyperpolarize poorly or have such short T_1's that they need to be polarized and immediately studied within the NMR spectrometer. Several findings from this study support the feasibility of accomplishing this. Specifically, it was possible to secondarily polarize polymers of glycine (N-acetyl di-and tri-glycine) as well as three small peptides N-acetyl lysine, N-acetyl α-MSH, and N-acetyl RGD. Although, in general the T_1 of the acetyl carbonyl decreased with increasing molecular weight of the biomolecule, the T_1's were on the order of ten seconds, and the correlation of T_1 with molecular weight was not exact. This was exemplified by the fact that N-acetyl α-MSH with a molecular weight that was 2 times larger than N-acetyl diglycine, had the same T_1. The ability to acetylate peptides with lysine side-chains also provides an excellent opportunity to label a number of important biomolecules, such as ubiquitin, which was previously done(Macdonald 2000). In fact, the T_1s values of the [1-^{13}C] acetyl adducts were 0.9 to 1.2 s based on saturation factors (SF) of 0.59-0.64 using a recycle time of 0.9 s(Macdonald 1999). Although likely too short, ubiquitin is about 100 μM in cells, the highest concentration of any protein, and free versus bound ubiquitin can be diagnostic of cancer(Ande 2009; Vlachostergios 2009; Vlachostergios 2009). If not useful clinically due to the short T_1 values, it certainly would be useful in structural NMR studies and investigating mechanism of protein adduct formation.

For *in vivo* applications, excess acetic anhydride and dioxanes cannot be used for reactions involved in secondary hyperpolarization due to their toxic effects. In the current study, it was possible to generate hyperpolarized N-acetyl cysteine in aqueous solution during the dissolution process within the hyperpolarizer. N-acetylcysteine is a drug administered IV to treat Tylenol overdose, so this method could be employed to investigate the biodistribution and metabolism of this drug in *ex vivo* and *in vivo* models of disease. It was also demonstrated for N-acetyl RGD using the perdeuterated acetic anhydride. The biodistriubution of this molecule, known to recognize and bind integrins(Ruoslahti 1996) which have been shown to be related to malignant phenotypes(Edick 2007; Goel 2008), shows a decrease in signal relative to surrounding benign tissues. This loss of signal is most likely a result of binding and this will be discussed in the following section (§4.3).

This secondary hyperpolarization approach has not been reported previously in the DNP literature. However, similar strategies have been used in the field of positron emission tomography (PET), which often involve incorporation of a radioactive nucleus into a ligand of interest shortly before administration to a patient. For example, biological peptides of interest bearing artificial amino acid side-chains as chelating groups can be "tagged" with positron-emitting isotopes such as technecium-99 and delivered to a patient(Bakker 1991; Van de Wiele 2001). These labeled tracers can then be assessed in vivo using a gamma camera. Potential advantages of hyperpolarized NMR over this technique include direct spectroscopic evidence of both uptake and metabolism, lack of ionizing radiation dose, short acquisition times, and direct correlation with MR images with superior soft-tissue contrast. However, evaluation of hyperpolarized ^{13}C substrates *in vivo* will be limited by relatively short ^{13}C T_1's of very large biomolecules, which can be quite short (on the order of seconds) for carbon atoms of interest in large proteins and drugs. The next step involves determining if secondary hyperpolarization approach can be used to analyze amino acid levels in human biofluids and used to characterization the biodistribution and metabolism of a small molecular weight drugs such as N-acetylcysteine and N-acetyl-RGD *in vivo*.

4.2 Polarization of Hexoses: Fructose

The *in vivo* metabolism of [1-^{13}C]-pyruvate and its metabolic products, [1-^{13}C]-lactate, [1-^{13}C]-alanine and ^{13}C bicarbonate, have been shown to correlate with disease progression(Albers 2008) and response to therapy(Day 2007) in animal models by DNP mediated hyperpolarized NMR. DNP substrates require a long T_1 relaxation to facilitate efficient spin diffusion during the process of hyperpolarization(Borghini 1968; Abragam 1978). Carbonyl carbons, which lack attached protons and limit the relaxation as a result of dipolar cross relaxation, have been the standard species to label and polarize with T_1's on the order of 40-60 seconds, depending on the field strength(Chen 2007; Merritt 2007; Wilson 2009).

Although a number of molecules of interest have been polarized and observed through their carbonyl carbons(Ardenkjaer-Larsen 2003; Albers 2008; Schroeder 2009; Warren 2009; Wilson 2009), a great number of important metabolic intermediates do not contain a carbonyl. Specifically, changes in carbohydrate metabolism occur with the evolution and progression of cancer(Denko 2008; Ganapathy 2008; Kroemer 2008) as well as a number of other human diseases such as non-alcoholic fatty liver disease(Farrell 2006; Douard 2008; Huynh 2008). Glucose carbons have very short T_1s (< 1 sec) and therefore uniformly ^{13}C labeled glucose, a mainstay of current metabolic studies(Antoniewicz 2006; Lane 2009), cannot be used as an *in vivo* hyperpolarized metabolic probe of glycolysis.

Fructose, occurring as an isomeric mixture of five and six membered rings, has as its most stable isomer β-fructopyranose with a hemiketal in the C_2 position. Fructose can enter glycolyis via hexokinase or fructokinase(Bais 1985; Skoog 1988; Petersen 1992; Funari 2005). The one-step metabolism via hexokinase to the phosphorylated fructose-6-phosphate is analogous to the first step of glycolysis, in which glucose is phosphorylated to glucose-6-phosphate. The metabolic flux to fructose-6-phosphate in the cell is related to the downstream glycolytic metabolic events as well as activity of the pentose phosphate pathway (PPP) (Voet 2004; Tong 2009; Vizán 2009). The pentose phosphate pathway is responsible for the predominant amount of nucleotide synthesis (which is increased at high turnover rates) and has been postulated to be a source of regeneration of NADPH in cancer cells(Kroemer 2008) making them more resistant to oxidative stress and allowing them to replenish glutathione.

Furthermore, metabolism of fructose is implicated in non-alcoholic steatohepatitis (NASH)(Farrell 2006), and in the pathogenesis of specific types of cancer. Fructose can also be metabolized to the fructose-1-phosphate via fructokinase, a reaction that takes place primarily in the liver(Bais 1985). Hepatic uptake via the GLUT5 transporter demonstrates relative specificity for fructose. Expression of this transporter may be an important biomarker for disease in extrahepatic tissues. For example, the human fructose transporter, GLUT5 (as shown in **Figure 4.9**), is highly expressed in breast cancer cell lines but not by normal breast tissue(Zamora-León 1996). A recent study of metabolites in the prostate gland has also shown a relationship between fructose and benign versus cancer tissues(Sreekumar 2009). Thus the goal of this series of studies was to investigate a new non-carbonyl hyperpolarized ^{13}C probe, [2-^{13}C]-fructose for the study of metabolism *in vivo*.

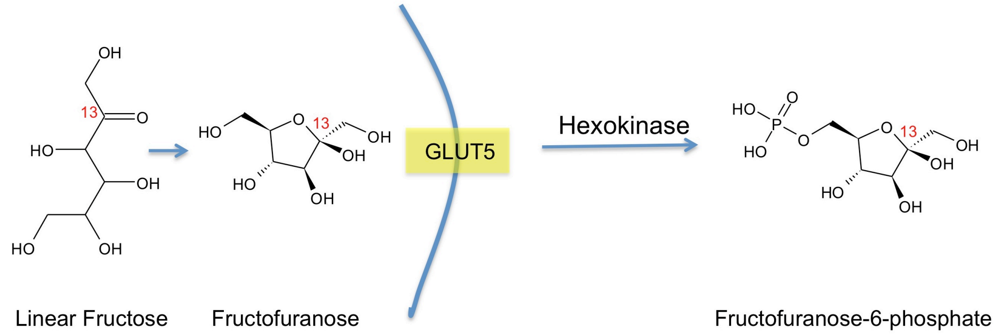

Figure 4.9. The mechanism for transport by GLUT5 and the first step of metabolism of fructose to fructofuranose-6-phosphate by hexokinase

Hyperpolarized [2-^{13}C]-Fructose Preparation

A 4.0M solution of [2-^{13}C]-fructose (Isotec, Miamisburg, OH) in water containing 15mM OX063 trityl radical (Oxford Instruments) was hyperpolarized on a Hypersense instrument (Oxford Instruments) as previously described(Ardenkjaer-Larsen 2003). The frozen sample was dissolved in 1X phosphate buffered saline (PBS), with a resultant pH of 7.6, and transferred immediately to a 10mm NMR tube.

11.7T NMR Studies of [2-^{13}C]-Fructose

NMR studies were performed on an 11.7T Varian INOVA spectrometer (125MHz ^{13}C, Varian Instruments) using a 10mm ^{15}N/^{31}P/^{13}C broadband direct detect probe and temperature controlled at 37°C. Initially, a thermal spectrum was acquired for a natural abundance fructose sample in 1X PBS buffer at 37°C (nt=9000, sw=30000, np=30000, TR=3.5s, acq time= 0.5s) using a 45° pulse. **Figure 4.10** demonstrates the natural abundance and hyperpolarized of ^{13}C spectra of fructose. The C$_2$ carbon resonances are denoted by the blue brackets and correspond to the isomeric distribution of the two ring forms (pyranose and

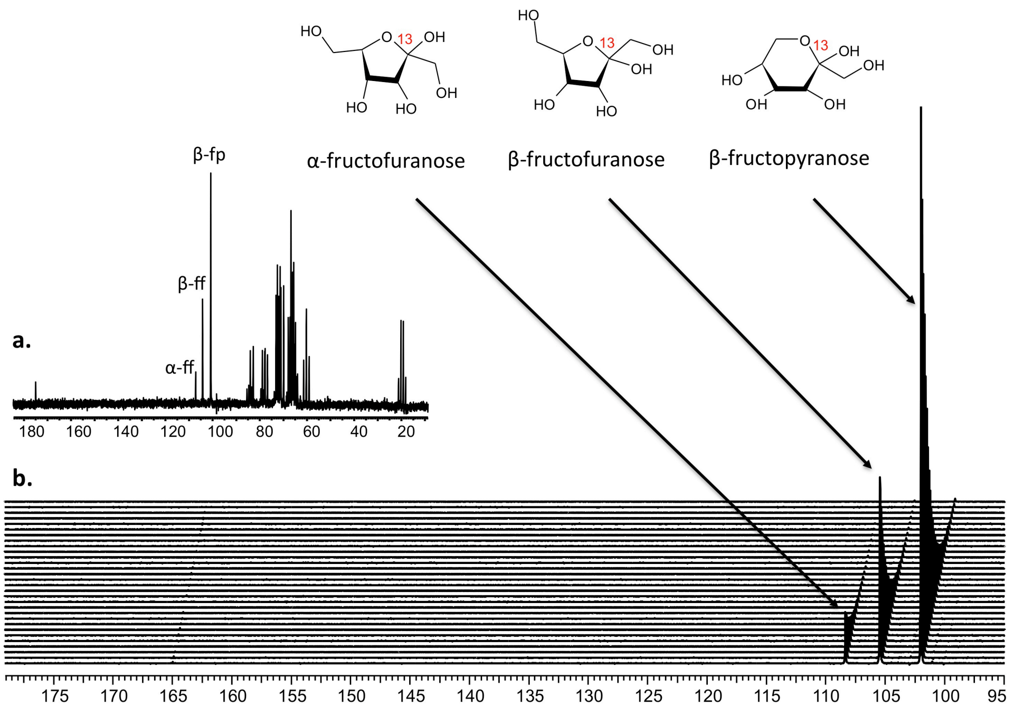

Figure 4.10. The natural abundance spectrum of fructose (a) and DNP spectrum of [2-^{13}C]-fructose (b). The linear form is present in the DNP spectrum, but at a very low level analogous to the thermal spectrum. (Top) Structures of each of the isomers are shown with their analogous resonance.

furanose forms) of the fructose molecule. For the acquisition of hyperpolarized ^{13}C spectra eighty pulse and acquire hyperpolarized ^{13}C NMR spectra (1 scan, spectral window = 20000 Hz, number of points= 40000, TR=3s, total acquisition time = 2 min 55s) were acquired using a 5° pulse and proton decoupled using a waltz-16 decoupling scheme. Hyperpolarized studies were followed by acquisition of thermal data with nearly identical parameters, using a 90° flip angle and a repetition time of greater than four T_1's (TR=300s, nt=16). For T_1 measurements hyperpolarized solution was placed into a NMR tube pre-heated to 37°C and this temperature is maintained using the variable temperature unit of the NMR spectrometer. T_1's were determined by collecting a series of spectra with 3 sec temporal resolution, starting 12 secs after dissolution. These spectra were then fit to a mono-exponential function to determine the spin-lattice relaxation time as previously described(Golman 2003; Gallagher 2008; Wilson 2009). Percent polarization in solution was calculated by comparing the first hyperpolarized spectrum acquired with its thermal spectrum, correcting for differences in tip angle (5° versus 90°), and the number of transients (1 versus 16) obtained. Solution state polarizations were calculated by correcting the enhancement for the T_1 relaxation during the transfer time (12 secs) from the polarizer to the spectrometer, and the thermal polarization at 11.7T (9.6ppm).

For NMR studies of the enzymatic conversion of Fructose to fructose-6-phosphate, hyperpolarized [2-^{13}C]-fructose was reacted with 400U of hexokinase (Sigma Aldrich) in the presence of 15mM ATP, 50mM TRIS and 13mM $MgCl_2$. The labeling and mechanism for transport and metabolism is shown in **Figure 4.9**, though in this enzymatic study the transport element has been removed and the enzyme activity was independently measured. Peaks corresponding to fructose-6-phosphate were identified using a natural abundance carbon spectrum, using a similar set of experimental parameters.

3T Studies of [2-^{13}C]-Fructose

T_1 studies were performed using a 3T GE Signa™ scanner (GE Healthcare, Waukesha, WI) equipped with the MNS (multinuclear spectroscopy) hardware package similar to studies at 11.7T, with temperature maintained using a heating pad calibrated to 37°C. Solution spectra were acquired using a 5° non-localized pulse, TR=3s and fit to a mono-exponential. The RF coil used in these experiments was a dual-tuned ^{1}H-^{13}C coil with a quadrature ^{13}C channel and linear ^{1}H channel construction based on an earlier design and also used in ^{13}C-pyruvate mouse imaging studies. For animal studies, T_2-weighted fast spin echo images were acquired prior to MRSI studies to denote anatomy and place voxels on the region of interest. *In vivo* MRSI studies were carried out using a compressed sensing double spin 3D MRSI acquisition scheme as previously published(Hu 2008) with a TE = 140ms, TR=215ms, FOV = 8cm x 8cm, and 16 x 8 resolution. 500μl of 80mM [2-^{13}C]-fructose (0.0013mmols/kg) was injected similar to previously described methods for [1-^{13}C]-pyruvate in a transgenic model of prostate cancer (TRAMP)(Albers 2008). High dose infusions of fructose (0.5g/kg) can lead to hyperuricemia(Wang 1981), but this is well above the dose given in these studies (0.24mg/kg). These injections were compared to the standard [1-^{13}C]-pyruvate injection for the same voxel in a tumor region of interest. Maps of resonance distributions were generated from the peak heights in each voxel and overlaid on the corresponding T_2-weighted image.

[2-^{13}C]-Fructose in vivo and ex vivo

Calculated T_1's for the C_2 fructose carbon are tabulated in **Table 4.3** for the cyclic isomers of fructose (β-fructofuranose, β-fructopyranose, α-fructofuranose) at both 11.7T and 3T, the field strengths of the *ex vivo* and *in vivo* hyperpolarized studies. The open chain (linear) isomer of fructose is present in very small amounts (0.4%)(Goux 1985; Skoog 1988) and not observed in the hyperpolarized NMR spectra. There was no significant difference in the C_2 T_1 between the cyclic isomers of fructose, most likely due to the fast chemical of the isomeric forms(Goux 1985). There was a small decrease in T_1 relaxation (≈2 sec) of the C_2 carbon with decreasing magnetic field strength from 11.7T to 3T (**Table 4.3**). To date, hyperpolarized ^{13}C agents have involved labeling at carbonyl positions, such as the C_1 position of pyruvate, due to their relatively long T_1's(Ardenkjaer-Larsen 2003; Golman 2003; Gallagher 2008; Gallagher 2008; Wilson 2009). In contrast to the

Table 4.3. T_1 relaxation times at 11.7T and 3T and percent polarization for each fructose isomer.

Isomer	T_1 sec (11.7T)	T_1 sec (3T)	%pol (corrected)
β-fructopyranose	16.3 ± 0.5	14.5 ± 0.3	12.0 ± 2.2
β-fructofuranose	15.8 ± 0.5	13.4 ± 0.5	11.6 ± 2.5
α-fructofuranose	15.8 ± 0.5	13.4 ± 0.4	11.8 ± 2.0

T_1 relaxation times at 11.7T and 3T (N=3 for both, ± s.d.) are shown for each of the isomers as well as percent polarization (N=3), which have been corrected for the time from dissolution to measurement. All studies were conducted at 37°C.

quaternary hemiketal carbon of the fructose isomers, carbonyl carbons decrease in T_1 with increasing field strengths(van de Ven 1995). This difference is predominantly due to chemical shift anisotropy dominating the T_1 relaxation of carbonyl carbons at higher field strengths(van de Ven 1995). This does not hold for the hemiketal of fructose, leading to the typical lengthening of T_1 with increasing field strength. Percent polarizations (**Table 4.3**) show similar values for the isomers of fructose with an average solution state polarization at 37°C of 12%. These polarization values are comparable, although somewhat lower, than those reported for other compounds of interest(Ardenkjaer-Larsen 2003; Kohler 2007; Merritt 2007) such as pyruvate, which has been reported to be polarized from 21-30% (Albers 2008; Schroeder 2008). There was no T_1 dependence on pH observed for pH ranges 5.9-7.8 for the fructose isomers.

The polarization levels were calculated relative to thermal signals from the same sample. The DNP polarizer sits in the fringe field of the 11.7T spectrometer in order to eliminate the possibility of passing the hyperpolarized sample through a zero field and loosing all polarization. For carbonyls such as the C_1 of pyruvate, we know that the T_1 increases at lower magnetic field strengths, and that the T_1 in the fringe field of the magnet should be longer, on the order of 80 secs as compared to 52 secs at 11.7T. This is due to the relationship between CSA and field strength ($CSA \propto B_o 2$), which dominates the carbonyl T_1 at high field strengths 36. However, as demonstrated in this publication, the T_1 of the quaternary C2 carbon of fructose is only slightly longer at higher field strengths (**Table 4.3**). Therefore the T_1 in the fringe field should be slightly shorter than 3T, which would result in a small underestimation of the percent polarization at time zero.

The reaction of hyperpolarized [2-^{13}C]-fructose with hexokinase after addition of fructose to the hexokinase in buffer within the NMR yields the phosphorylated pentose within 5 seconds (**Figure 4.11**). An expansion of the downfield region of the spectrum (**Figure 4.11a**) shows the split in the 105.5ppm resonance, which is a combination of both the β-fructofuranose and the β-fructofuranose-6-phosphate (the predominant isomeric form of fructose-6-phosphate). **Figure 4.11** also compares the first scan of the hyperpolarized acquisition (**Figure 4.11b**) versus the thermal spectrum acquired over 85 minutes post DNP (**Figure 4.11c**). It is apparent that the enzyme has now fully converted the fructose to fructose-6-phosphate and there is no longer a resonance corresponding to β-fructopyranose.

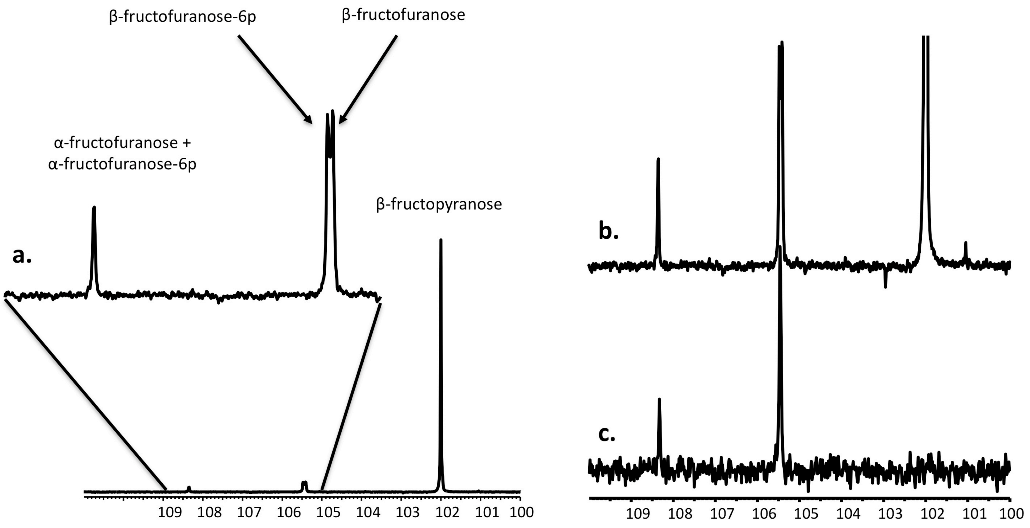

Figure 4.11. (a) Spectrum of fructose reacted with 400U of hexokinase, the zoomed in region demonstrates the resonances corresponding to the fructose and fructose-6-phosphate. (b) The dynamic spectrum after 5 secs of reaction with hexokinase. (c) The thermal spectrum of same solution with hexokinase averaged 85 min post DNP.

Figure 4.12 demonstrates the metabolism following separate injections of 80mM hyperpolarized fructose (**Figure 4.12d**) and pyruvate (**Figure 4.12e**) in the same TRAMP mouse. As previously published(Albers 2008), the primary TRAMP tumor demonstrates high levels of hyperpolarized lactate, as well good signal to noise spectra of hyperpolarized fructose and it's metabolite β-fructofuranose-6-phosphate. Injections of 80mM hyperpolarized fructose yielded an average total signal-to-noise ratio of 21.0 ± 2.1 in tumor slices (an average of 70 voxels in 2 slices was used for N=3 TRAMP mice). Because the isomeric ratio of the fructose pyranose

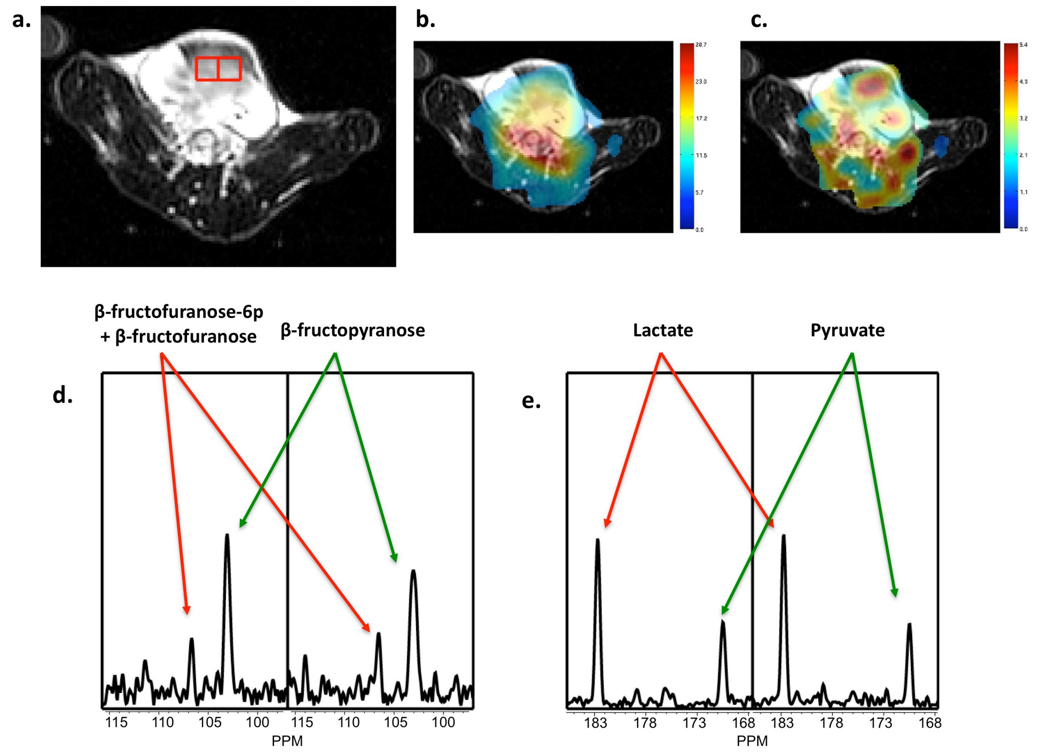

Figure 4.12. (**a**) T_2-weighted image of a moderate to late stage TRAMP mouse prostate tumor. Metabolite image overlays of the resonances corresponding to total hyperpolarized fructose (**b**) and composite β-fructofuranose-6-phosphate and β-fructofuranose (**c**) obtained after injection of 80mM [2-^{13}C] fructose demonstrate spatial differences in total fructose versus the composite β-fructofuranose-6-phosphate resonance. Spectra corresponding to the two red voxels (**d**) in the tumor demonstrate the resonances corresponding to β-fructopyranose and the composite β-fructofuranose-6-phosphate and β-fructofuranose. Pyruvate and lactate resonances are shown from the same locations (**e**) obtained after an injection of 80mM hyperpolarized pyruvate in the same mouse.

to furanose in solution is approximately 77/23(Skoog 1988) the *in vivo* peak at 105.5ppm (and if visible the downstream 108.25ppm resonance) is not solely due to β-fructofuranose-6-phosphate but also has a small contribution from β-fructofuranose. In this relatively large TRAMP tumor, both high levels of LDH activity and hexokinase activity were observed 15 secs post-injection in the same 0.035cc voxels. **Figure 4.12b** demonstrates the distribution of the total fructose signal throughout the slice, a measure of combined delivery and uptake of hyperpolarized fructose. Slightly higher levels of total hyperpolarized fructose were observed in the tumor region relative to surrounding muscle in the same slice. In comparison, **Figure 4.12c** demonstrates the distribution of the resonance at 105.5ppm, which includes the metabolite β-fructofuranose-6-phosphate. Importantly, this resonance has a good signal-to-noise (≈ 5:1) and is co-localized in regions of high lactate within the tumor (**Figures 4.12d and 4.12e**).

Figure 4.13 demonstrates a case where there was tumor only in the left side of the murine prostate, providing a direct comparison of hyperpolarized fructose uptake/ delivery and metabolism between benign and malignant prostate tissues. The MRSI data demonstrated that the resonance corresponding to the composite β-fructofuranose and β-fructofuranose-6-phosphate were higher in the regions of tumor as compared to the benign prostate tissues (**Figure 4.13d**). Interestingly, there is no difference in total hyperpolarized fructose in regions of malignant versus benign prostate tissue. However, the composite β-fructofuranose and β-fructofuranose-6-phosphate resonance (**Figure 4.13c**) was dramatically higher in malignant left lobe of the prostate as compared to the benign right side (**Figure 4.13c and 4.13d**).

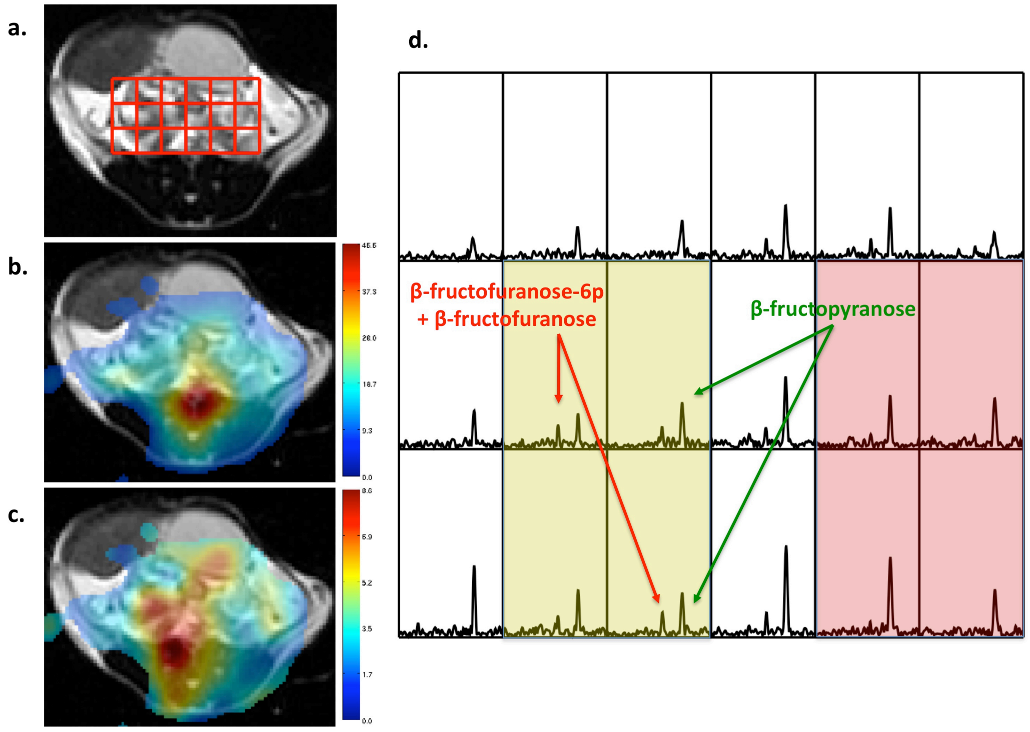

Figure 4.13. (a) T2-weighted image of a TRAMP mouse with tumor only on the right side of the prostate. Metabolic images of total hyperpolarized [2-^{13}C]-fructose resonances (b) and the composite β-fructofuranose-6-phosphate and β-fructofuranose (c) are shown overlaid on the T_2-weighted image. Resonances corresponding to the β-fructopyranose and composite β-fructofuranose-6-phosphate and β-fructofuranose are shown in the corresponding spectral array (d). The yellow area demonstrates a region of tumor, compared to a region of benign prostate tissue in red. An unassigned spurious, low signal-to-noise resonance appears at 115 ppm.

In this study, [2-^{13}C]-fructose was hyperpolarized using the DNP method and shown to have sufficiently long T_1's and polarizations sufficient for hyperpolarized ^{13}C NMR spectroscopic and MRSI studies. The hemiketal C_2 of fructose demonstrates the first non-carbonyl to be hyperpolarized for use as a metabolic probe and suggests the potential of using other hyperpolarized probes involving quaternary carbons even those in ring structure. Enzymatic conversion of hyperpolarized [2-^{13}C]-fructose, to fructose-6-phosphate has been demonstrated in vitro and in vivo. This new hyperpolarized probe is exciting from the standpoint that malignant tissue was discriminated from benign prostate and surrounding tissues based on the detection of hyperpolarized β-fructofuranose-6-phosphate. The enzymatic conversion of hyperpolarized fructose allows the probing of important changes in glycolytic metabolism upstream of pyruvate, including upregulated hexose uptake(Zamora-León 1996), hexokinase activity and changes in flux through the pentose phosphate pathway(Kroemer 2008). Although, this study was focused on prostate cancer models, upstream glyolytic processes have been the basis of a number of cancer studies including the HIF-1 and PI3K related processes(Kroemer 2008). Therefore changes in fructose metabolism may be important in the assessment of therapies that target these pathways. A potential link between fructose metabolism and non-alcoholic fatty liver disease has also been demonstrated(Donnelly 2005) and thus hyperpolarized fructose could become a valuable metabolic imaging agent to study this and other diseases both *ex vivo* and *in vivo*. Moreover, the dose of fructose given in this murine study translates into a very safe patient dose.

4.3 Binding by DNP

It is still unclear what information is present in the changes of hyperpolarized signal as a function of its nuclear environment. The dominant force associated with decay of the hyperpolarized signal is spin-lattice relaxation (or T_1). Long T_1 carbons have hyperpolarized signals that last longer and the life-time of the polarized state can be furthered preserved by generating a spin state where relaxation is quantum mechanically disallowed(Warren 2009). Typically the solution state T_1 relaxation time has been used as a parameter for determining what spins to label and observe in most DNP work. The goal of this study was to use T_1 relaxation to understand the how binding of the hyperpolarized probe impacts life-time of the polarized state, a critical question for *in vivo* imaging studies of hyperpolarized probes.

It is well known that in fast exchange systems, changes in parameters such as observed magnetization, chemical shift, and spin relaxation rates (T_1, T_2, $T_{1\rho}$ etc…) can be used to estimate equilibrium constants such as the binding constant in a ligand-host system(Fielding 2007). One such well-characterized system is that of benzoic acid (ligand) and β-cyclodextrin (host)(Rekharsky 1998; Schneider 1998). In the presence of β-cyclodextrin, the aromatic ring of benzoic acid preferentially inserts itself into the inner-core of the cyclodextrin molecule by hydrophobic interactions(Aree 2003).

To explore this system, samples of benzoic acid were dissolved in dimethylacetamide (DMA) to a concentration of 3.6M. 2mg of the Finland radical(Reddy 2002; Dhimitruka 2007) per 100mg of benzoic acid was used as the organic free radical. Prepared samples were polarized for approximately 1 hour (at 94.094 Ghz) in a Hypersense® (Oxford Instruments, Oxford UK) and dissolved in 5mL of 100 mM phosphate buffer (pH=7.8). For assessment of binding, the hyperpolarized benzoic acid solution was mixed with 0.5mM β-cyclodextrin in the same 100mM phosphate buffer. All NMR studies were conducted at 310°K in a 10mm broadband probe on a 500Mhz (125Mhz for ^{13}C) Varian INOVA NMR spectrometer. All data were acquired using a 5° flip angle, 3s repetition time and 1 transient. Apparent T_1 relaxation times were fit to a mono-exponential equation in Matlab (Mathworks) as previously described(Deichmann 1999; Wilson 2009).

As shown in **Figure 4.14**, all carbons of unlabeled benzoic acid were hyperpolarized, observed and resolved in one 5° degree pulse at a concentration of 36.4mM. Hyperpolarized benzoic acid was then mixed in increasing concentrations

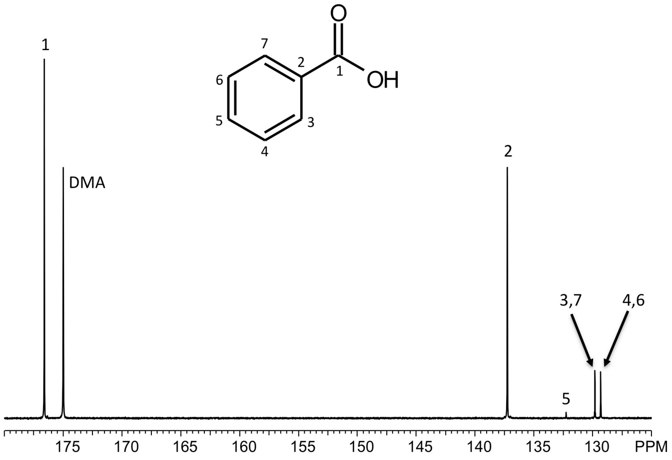

Figure 4.14. Single 5° pulse spectrum of 36.4mM natural abundance benzoic acid (310K, pH=7.8). All carbons are observed: C1 – 176.6 ppm, C2 – 137.3 ppm, C3,C7 – 129.8 ppm, C4, C6 – 129.3 ppm and C5 – 132.2 ppm.

relative to 0.5 mM β-cyclodextrin to assess the changes in T_1. **Figure 4.15** demonstrates the change in hyperpolarized signal with time for a solution of benzoic acid (**Figure 4.15a**) and benzoic acid with the addition of 0.5mM β-cyclodextrin. Overall signal decreased more rapidly in time as a result of the interaction of the benzoic acid carbons and β-cyclodextrin. The apparent T_1 relaxation time in **Figure 4.15** decreased from 34.9 secs and 19 secs (**Figure 4.15a**) to 28.8 secs and 16.4 secs (**Figure 4.15b**) for the C_1 and C_2 carbons of benzoic acid respectively.

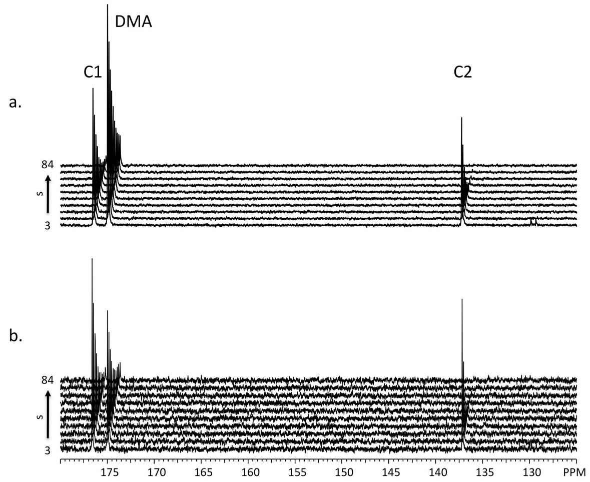

Figure 4.15. (a) Hyperpolarized benzoic acid and (b) benzoic acid with the addition of 0.5mM β-cyclodextrin are shown. Every third spectrum of the array is shown (a temporal resolution of 9 secs).

Increasing concentrations of benzoic acid relative to a constant β-cyclodextrin were used to generate **Figure 4.16**, where ΔObs is defined as 1/T1obs-1/T1free. The y-intercept of the linear fit can be used to determine the log binding constant (log K) as a result of changes in the observed T_1 for the C_1 and C_2 (Fielding 2007). The log K derived from the fits of the C_1 and C_2 changes were 1.74 and 1.68 respectively. These constants were within the range of reported log K measurements of benzoic acid (1.5-2.2) interacting with β-cyclodextrin(Rekharsky 1998). Hyperpolarized signal for the other benzoic acid carbons was so greatly reduced that T_1 measurements were not reliable, though this reduction in signal relative to the free benzoic acid exemplifies the effect of binding on hyperpolarized signal.

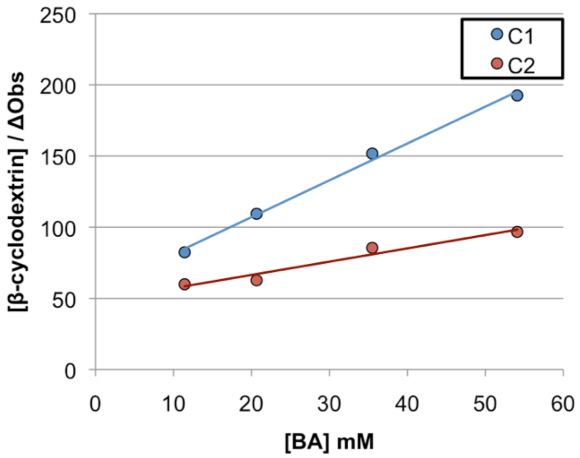

Figure 4.16. Plot of [β-cyclodextrin]/ΔObs in as a function of increased benzoic acid [BA] concentration. The R^2 of the C_1 and C_2 fits were 0.995 and 0.953 respectively.

To further demonstrate the influence of binding on changes in observed T_1 and thus hyperpolarized signal decay, naproxen was hyperpolarized in DMA similar to benzoic acid. Naproxen, an over the counter pain reliever, has a structure similar to benzoic acid, which leads to similar inclusion in the cyclodextrin structure. As shown in **Figure 4.17,** five carbons of naproxen are readily hyperpolarized and observed. To demonstrate the effect of binding on this drug's hyperpolarized signal decay and the utility of polarizing a native ligand, 6.5mM hyperpolarized naproxen was mixed with 0.5 mM β-cyclodextrin. The T_1 relaxation time of the free naproxen C_1 was 14.8 ± 0.3 secs (n=3) and in the presence of the host was reduced ~30% to 10.6 secs (n=3). Similar to the benzoic acid experiments, the other observable carbons were decreased below reliable T_1 quantification.

Typically in drug discovery experiments, the question of binding of the drug to its target of interest is of great importance. NMR studies of these compounds at low concentrations in solution can require long experiment times and complicated mechanisms. In this experimental setup, with knowledge of the carbon's T_1, binding can be assessed in a single experiment within minutes. This information also lends itself to further understanding of the nature of hyperpolarized signals as a result of metabolism *in vivo*. For example, in studies of hyperpolarized [1-^{13}C] pyruvate in a perfused Langendorff heart model(Merritt 2007; Schroeder 2008) as well as *in vivo* studies of tissues in murine models(Albers 2008) signals are generated from metabolism of pyruvate through the first step of the Kreb's cycle that leads to the generation of CO_2 (via pyruvate dehydrogenase) and bicarbonate (facilitated by carbonic anhydrase). These signals appear lower than what would be expected in highly oxidative tissues. It is possible that a percentage of the signal that is not observed is a result of a T_1 loss associated with the enzyme-substrate interactions and the mechanism of enzymatic conversion, impacting assessment of relative metabolic fluxes.

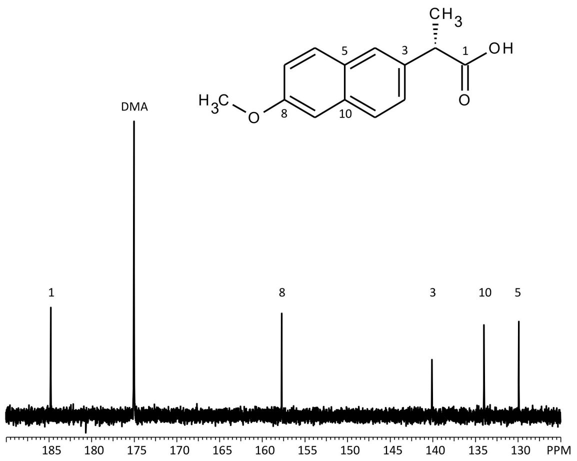

Figure 4.17. Single 5° pulse spectrum of 18mM hyperpolarized natural abundance naproxen demonstrating the polarization of 5 carbons.

Though the effect of binding on T_1 relaxation is a well understood, the impact of this on the T_1s of new hyperpolarized probes is a critical question in assessing the utility of the new probe as a *in vivo* imaging agent, and for accureatly determining metabolic fluxes using these probes.

4.4 Other Novel Compounds

Studies of hyperpolarized [1-^{13}C] pyruvate(Chen 2007; Day 2007; Kohler 2007; Merritt 2007; Albers 2008; Keshari 2008; Schroeder 2008) as well as the previously mentioned compounds (§4.1 and 4.2) have provided interesting preliminary results both *in vivo* and *ex vivo*. Additionally, hyperpolarized probes have been secondarily labeled (§4.1), used for observing glycolytic metabolism (§4.2), and to determine binding constants (§4.3). Although in theory the method of hyperpolarization is generally applicable, the development of new probes is not a trivial. The purpose of this section is to delve deeper into more novel hyperpolarized probes, which are still in developmental stages.

[1-^{13}C]-glycine: as a marker of mitochondrial activity

Isotopomer studies of [2-^{13}C] glycine have been developed and used to assess mitochondrial activity by exploiting the one carbon cellular metabolism pathway(Cowin 1996) as shown in **Figure 4.18**. **Figure 4.18** is a schematic representation of the synthesis of serine in the cytosol and the

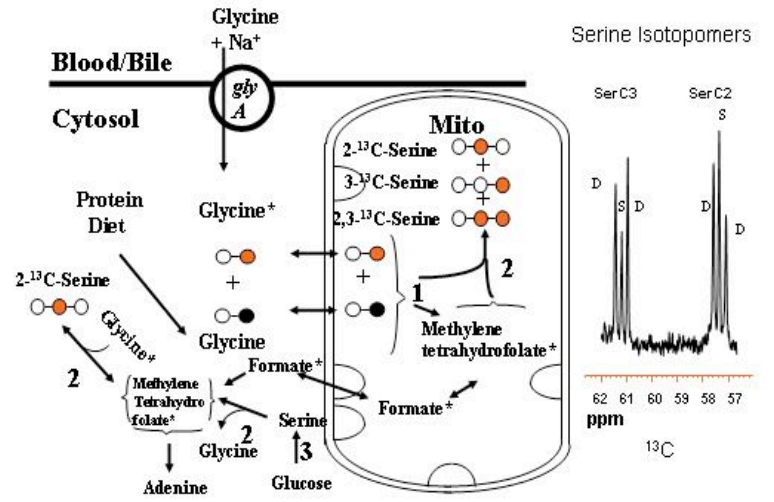

Figure 4.18: Compartmentation of serine synthesis and the use of isotopomeric analysis and ^{13}C MRS to determine biochemistry and to monitor mitochondrial function.

mitochondria of the cell and the different isotopomers that are formed in these two cellular compartments. On the right side of **Figure 4.18** is a portion of a representative ^{13}C NMR spectrum of PCA extract of rat infused for three hours with [2-^{13}C]-glycine, demonstrating the various peaks corresponding to the three serine isotopomers that are formed. The methyl donor in serine synthesis depends on substrate used (Pasternack 1994), and glycine is the major methyl donor in the mammalian mitochondria(Cowin 1996; Cowin 1996). The cytosolic methylating agent, S-adenosylmethionine, was unlabeled in the study shown in figure 4.18, therefore, the peak pattern at the C_2 and C_3 of serine should be the same, however, the singlet C_2 peak, representing [2-^{13}C]-serine isotopomer, is larger than the singlet C_3 peak, representing the [3-^{13}C]-serine isotopomer. The additional C_2 singlet signal represents 20% of the total serine C_2 and C_3 peak area, indicating that 20% and 80% of the serine was formed in the cytosol and mitochondria, respectively. In mammals there is both a cytosolic (cSHMT) and mitochondrial (mSHMT) that serine hydroxylmethyl transferase that can reversibly convert glycine to serine(Cowin 1996). The isotopomer analysis presented relies on the label scrambling in the mitochondria and the generation of differentially labeled serine to determine mitochondrial activity.

Typically the C_1 carbon is not used in traditional ^{13}C NMR experiments due to its long T_1 relaxation time, which requires long scan times for data acquisition. In the case of DNP, the long T_1 is an advantage, allowing the hyperpolarized signal to propogate for longer periods of time. When glycine is labeled in the C_1 position, the label will follow a similar progression as the C_2 shown in **Figure 4.19**. In the cytosol it will become C_1 labeled serine, but in the mitochondria it will be cleaved by the glycine decarboxylase complex and form $^{13}CO_2$ (**Figure 4.19**). When hyperpolarized the conversion of glycine to CO_2 and serine in real time can yield comparable information to the previously mentioned isotope method.

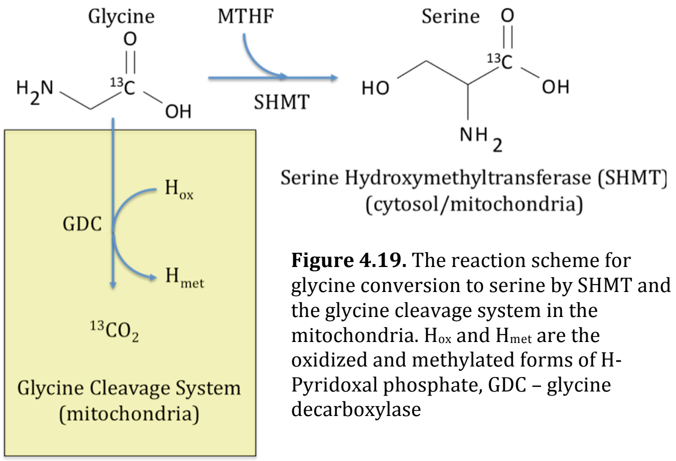

Figure 4.19. The reaction scheme for glycine conversion to serine by SHMT and the glycine cleavage system in the mitochondria. H_{ox} and H_{met} are the oxidized and methylated forms of H-Pyridoxal phosphate, GDC – glycine decarboxylase

To investigate this potential mechanism, a high concentration glycine preparation was designed with concentrated base. 100mg of [1-^{13}C]-glycine was dissolved in 70μL of 19N NaOH, 30μL of dimethylsulfoxide (DMSO) and 3.8mg of the OX63 radical, yielding a final concentration of approximately 6.7M. **Figure 4.20** is a dynamic acquisition of 10uL of the glycine preparation dissolved in 5.3mL of pH=7 40mM TRIS buffer with 0.3mM EDTA, final concentration of 12.6mM. The measured

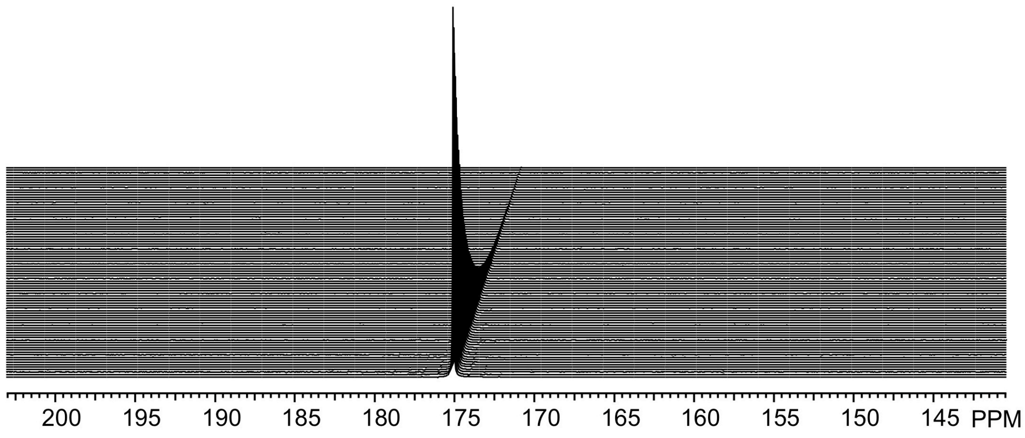

Figure 4.20. Dynamic experiment of 12.6mM [1-13C]-glycine. The first 86 scans (TR=3 secs) are shown.

T_1 of glycine was 38.8 secs, slightly shorter than the T_1's for the C-1 carbonyl of pyruvic acid (48.3 secs) at 11.7T. Injection of glycine into a bioreactor containing JM1 cell encapsulates did not yield any additional resonances, and in cases, the apparent T_1 of the hyperpolarized glycine resonance appeared to be dramatically shortened. This may be a result of binding effecting the T_1 of the carbon and thus facilitating the loss of hyperpolarized signal.

[guanidino-^{13}C]-creatine: as a marker of cellular energetics

Cells, particularly skeletal muscle and the brain cells, use phosphocreatine (PCr) as an energy store(Saks 2007). Creatine is reversibly phosphorylated by creatine kinase, one of the fastest endogenous enzymes known. In the presence of excess ATP, phosphate is stored in the cell as PCr(Schlattner 2006). The activity of creatine kinase can also be used as an indicator of changes in creatine uptake, which is potentially linked to changes in cancer resistance to chemotherapy. To access this fast reaction, creatine can be ^{13}C labeled in the guanidino position (**Figure 4.21**) and hyperpolarized (**Figure 4.22**). The T_1 of hyperpolarized [guanidino-^{13}C] creatine was measured to be 14 secs (**Figure 4.22)**. When creatine is phosphorylated to phophocreatine, there was a shift of the labeled carbon from 160.9ppm (creatine) to 162.8ppm (PCr), providing sufficient resolution to observe both hyperpolarized Cr and PCr and the PCr/Cr in real time. An acid based preparation for creatine was

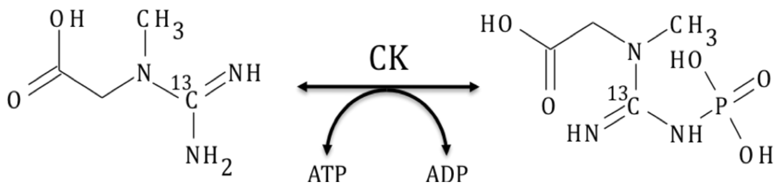

Figure 4.21. The reversible reaction mechanism for creatine kinase, converting the [guanidino-^{13}C]-creatine

designed to explore this enzymatic conversion. 100 mg of [guanidino-^{13}C] creatine was dissolved in 70µL of 12N HCL, 50µL of dimethylacetamide (DMA), and 4.5 mg OX63, yielding a concentration of approximately 3.5M. The T_1 was measured to be 22 secs. When reacted with creatine kinase, the signal disappeared entirely. Similar to glycine, it is possible that the loss in hyperpolarized singal is due to a tight binding of creatine with creatine kinase resulting in a dramatic shortening of the T_1 of the ^{13}C labeled carbon. Further studies would be required to characterize this loss.

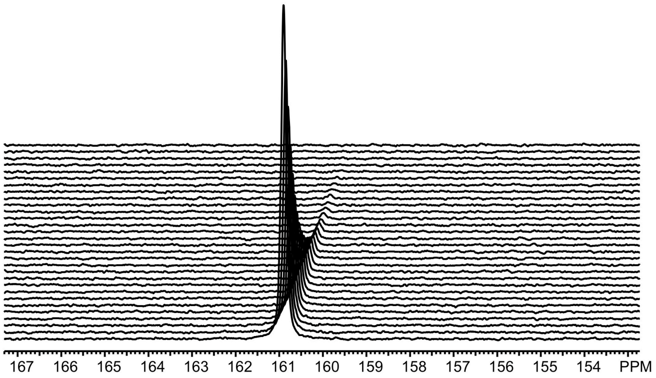

Figure 4.22. Dynamic experiment of hyperpolarized ^{13}C creatine, the resonance at 106.9ppm corresponds to the guanidino carbon.

[7-^{13}C]-nicotinamide: a biomarker of cellular redox

The balance of reducing and oxidizing molecules governs many important cellular pathways. Cofactors such as NAD(H) and NADP(H) play an important role in the ability to deal with toxins as well as limiting in metabolic schemes related to cancer. Labeling of the pathway associated with nicotinamide metabolism has been shown by ^{13}C NMR in both Saccharomyces cerevisiae and Escherichia coli(Unkefer 1984). Due to the large separation in chemical shift of the C_2 (δ=1.5ppm) and C_5 (δ=23ppm) positions of nicotinate, in ^{13}C labeling studies, Unkefer et al. were able to separate reduced and oxidized forms of nicotinamide derivatives and measure redox ratios. Due to overlap between the C_7 of nicotinate and NADH, it was not useful in the previous study, but in humans nicotinamide is typically phosphorylated and is not metabolized through nicotinic acid (**Figure 4.23**). The C_7 of nicotinamide (170.8 ppm) provides a good separation between the original DNP molecule and the metabolic reduced (173.6 ppm) and oxidized (166.2 ppm) forms.

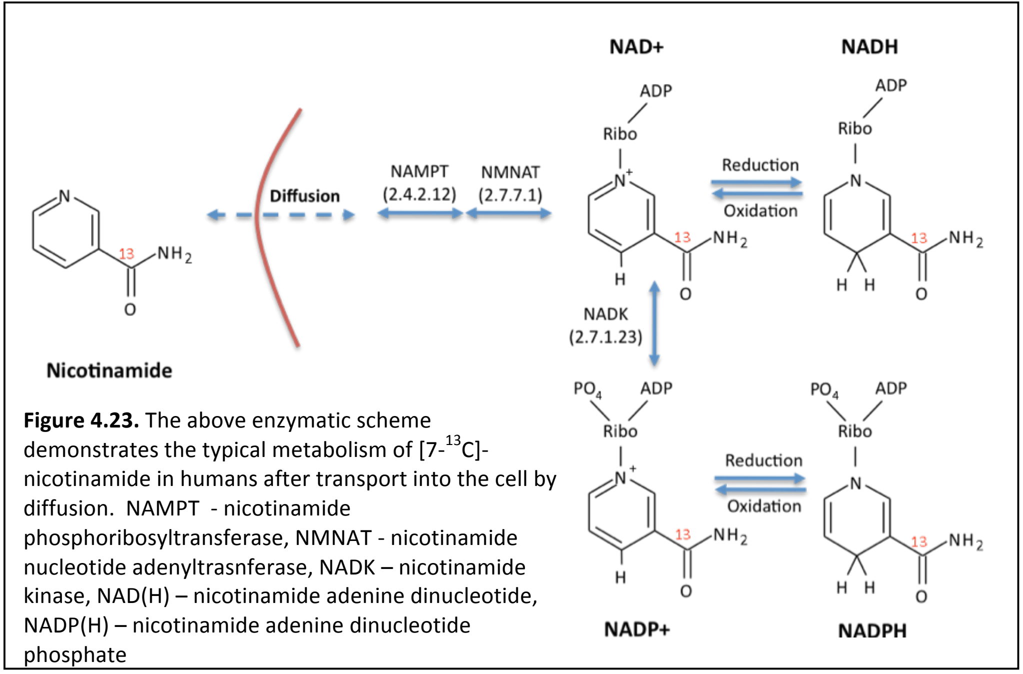

Figure 4.23. The above enzymatic scheme demonstrates the typical metabolism of [7-^{13}C]-nicotinamide in humans after transport into the cell by diffusion. NAMPT - nicotinamide phosphoribosyltransferase, NMNAT - nicotinamide nucleotide adenyltrasnferase, NADK – nicotinamide kinase, NAD(H) – nicotinamide adenine dinucleotide, NADP(H) – nicotinamide adenine dinucleotide phosphate

The uptake of the nicotinamide has been shown to be mediated by free diffusion(Lan 1968), thus allowing for potentially fast metabolism to the products of interest and the T_1 of the C_7 carbon is adequately long for hyperpolarization. As a result of the high cost of the compound, a first step was taken to synthesize the [7-^{13}C] nicotinamide using a previously published reaction scheme(Yang 2004). The reaction scheme in **Figure 4.24** was used to attempt the labeling of [7-^{13}C] nicotinamide. The first step of the reaction was done over 17 hours at 80°C. Thin layer chromatography showed a separation of the labeled compound, though purification became a major hindrance. Future experiments will focus on this synthesized compound and its polarization for *in vitro* application.

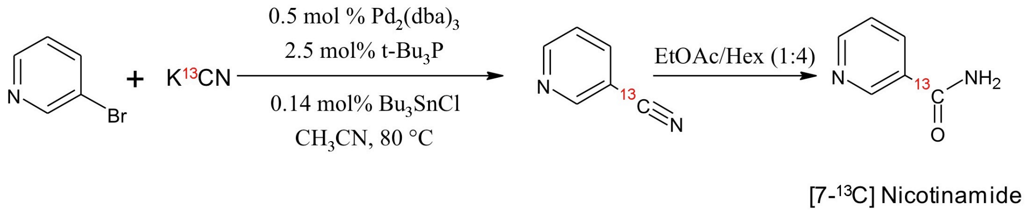

Figure 4.24. Reaction scheme for synthesis of [7-^{13}C] nicotinamide.

Hyperpolarized ^{31}P-Phosphoric acid

In most bioreactor studies, ^{31}P spectra are acquired to determine the viability of cells or tissues during the time course of the experiment (Daly 1988; Narayan 1990; Masson 1992; Macdonald 1993; Gillies 1994; Farghali 1996). Depending on the cell density, ^{31}P scans can take 1000s of averages. Traditional media such as DMEM and RPMI are supplemented with sodium phosphate, which plays an important role in cellular energy metabolism (i.e. incorporation in the NTP's, etc.). With the potential dramatic increases afforded by hyperpolarization, phosphoric acid was chosen as a candidate for polarization, in order to assess cellular energy metabolism.

433μL of phoshphoric acid was mixed with 10mg of OX63 radical (final concentration of phosphoric acid - 17M) and polarized using a Hypersense® polarizer for 1 hour. In order to observe the resonance as it was building up, a nearby Varian spectrometer was used to pulse on the coil inside the polarizer at the frequency for ^{31}P at 3.35T. Dissolution of hyperpolarized phosphoric acid in water is shown in **Figure 4.25** at 11.7T. A fit to the decay yields a T_1 of approximately 8 secs and a back calculated enhancement of approximately 100. This is well below polarizations obtained for hyperpolarized ^{13}C labeled carbonyls and the other ^{13}C-labeled probes discussed above. However, optimization of the polarization protocol could yield improved signal enhancements. It is possible that the acidity effected the polarization on dissolution, causing it to relax faster. Generally compounds retain their polarization under more basic conditions and if the phosphoric acid was neutralized in dissolution, it could have yielded higher polarizations. Future studies of hyperpolarized phosphoric acid will require the optimization of the sample preparation and dissolution process, but could yield appreciable enhancements of ^{31}P spectra in bioreactor studies.

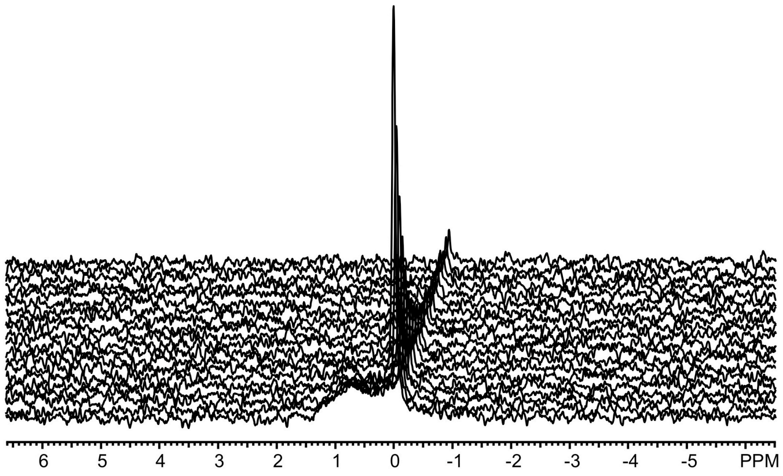

Figure 4.25. Dynamic experiment of hyperpolarized ^{31}P Phosphoric acid. The T_1 decay is on the order of 8 secs and shows a moderate enhancement (approximately 10^2 at dissolution).

4.5 Multipolarization

A significant advantage of hyperpolarized MR metabolic imaging using dynamic nuclear polarization (DNP) is the ability to probe metabolic fluxes in real time, at high signal to noise(Ardenkjaer-Larsen 2003). *In vivo* hyperpolarized MR is unprecedented in its ability to characterize specific enzymatic pathways(Golman 2003; Golman 2006). Most studies to date have focused on the last step of glycolysis in which [1-^{13}C] pyruvate is enzymatically converted to a number of products, including [1-^{13}C] lactate mediated by the activity of lactate dehydrogenase (LDH)(Golman 2003; Golman 2006; Kohler 2007; Merritt 2007; Albers 2008). This pathway is associated with the Warburg effect, which postulates enhanced aerobic glycolysis to lactate in tumour cells relative to normal tissue(Warburg 1956). More recently, a number of additional pathways have been probed, for example the conversion of bicarbonate to CO_2 as mediated by carbonic anhydrase(Gallagher 2008), and the conversion of glutamine to glutamate catalyzed by glutaminase(Gallagher 2008). Investigation of these processes by hyperpolarized NMR has allowed mapping of pH *in vivo* and assessment of glutaminase activity in hepatic tumour cells. Additional agents showing promise in animals or perfused heart models include [2-^{13}C] pyruvate(Schroeder 2009) and [1-^{13}C] lactate(Chen 2008). As the number of useful DNP agents continues to expand, the ability to probe multiple pathways and mechanisms simultaneously may provide valuable metabolic "signatures" associated with specific types of tumour and other diseased tissue. ^{1}H MRS is well established as a means to establish metabolic profiles in diseased tissue *in vivo* (Dillon 1999; Kurhanewicz 2002), but hyperpolarized MR has the additional capacity to provide kinetic information. A particular conversion pattern observed in diseased tissue may aid in targeting regions of pathology for biopsy or focal therapy, and/or better characterize the extent or aggressiveness of disease present prior to or after treatment.

In addition to providing real-time information about *in vivo* metabolism, the agents used in hyperpolarized ^{13}C MRI have other important advantages over contrast agents currently in clinical use. Since endogenous molecules are utilized, these agents are expected to have little or no toxicity in humans, even at relatively high concentrations. This feature is particularly appealing given recent concerns about contrast nephropathy associated with iodinated CT contrast, as well as nephrogenic systemic fibrosis (NSF) seen in patients receiving gadolinium chelates for MR(From 2008; Thomsen 2008). While many new ^{13}C labeled agents may be appropriate for metabolic imaging in humans, ^{13}C sodium bicarbonate has special promise due to its well-demonstrated lack of toxicity and ability to probe physiological pH. In addition, a broad number of pathologic processes demonstrate alterations in pH, including neoplastic, ischemic, and inflammatory conditions(Syrota 1985; Hohn-Berlage 1989; Schindler 1996; Ciriolo 1997).

The dynamic nuclear polarization process requires the ^{13}C labeled probe compound to be in an amorphous (glassy) solid state with the appropriate free radical concentration at low temperatures (~1.2°K)(Ardenkjaer-Larsen 2003). To accomplish an optimal preparation of a new probe, the highest possible concentrations of the desired agent, solvent/glassing agent(s), presence, concentration and type of a gadolinium agent, and the concentration and type of free radical must all be optimized. In addition, appropriate dissolution media must be prepared for each agent in order to ensure physiological pH, osmolarity, and to preserve the longest possible T_1. In this section, a method for direct polarization of ^{13}C sodium bicarbonate is reported, that is suitable for use in humans. This method has been combined with a co-polarization technique that allows simultaneous polarization of ^{13}C-bicarbonate and [1-^{13}C]-pyruvate, to perform both pH and metabolic mapping in vivo using a single intravenous bolus. The technique was subsequently extended to polarize four ^{13}C labeled substrates providing information on pH, metabolism, necrosis and perfusion, namely [1-^{13}C]-pyruvic acid, ^{13}C-sodium bicarbonate, [1,4-^{13}C]-fumaric acid, and ^{13}C-urea, in a single imaging experiment.

Hyperpolarized Sample preparation

In all cases the ^{13}C compounds were purchased from Isotec (Miamisburg,OH) and used without further purification. All natural abundance chemicals and solvents were obtained from Aldrich (Miamisburg,OH). *^{13}C-sodium bicarbonate*:

135mg of ^{13}C-sodium bicarbonate were dissolved in 1099mg of glycerol, in a sealed flask while heating with a heat-gun. The hot solution was then passed through a 0.45µm Millipore MCE Membrane filter (Fisher Scientific), and OX63 radical (Oxford Instruments, Abingdon, UK) was then dissolved to a final concentration of 20mM. *^{13}C-pyruvic acid*: To a neat sample of [1-^{13}C]-pyruvic acid was added OX63 radical to a final concentration of 15mM. *^{13}C-fumaric acid*: 350 mg of [1,4-^{13}C]-fumaric acid were mixed with 500µL of dimethyl sulfoxide (DMSO) and OX63 was added to a final concentration of 15mM. *^{13}C-urea*: 390mg of ^{13}C-urea were dissolved in 895mg of glycerol (Aldrich), and OX63 was added to a final concentration of 15mM.

Co-polarization of ^{13}C-Sodium Bicarbonate with [1-^{13}C]-Pyruvic Acid

For studies at 11.7T, 125mg of the ^{13}C-sodium bicarbonate preparation were placed in a sample cup and frozen in liquid nitrogen, followed by addition of 2.2µL of pyruvic acid preparation. The sample was rapidly frozen to avoid mixing of the materials, and polarized at 94.074 GHz and 1.2-1.4°K for 3.5h using a Hypersense® DNP polarizer (Oxford Instruments, Abingdon, UK). This microwave frequency corresponded to the optimum microwave frequency for the ^{13}C sodium bicarbonate sample, which was approximately 10 MHz lower than the optimum frequency observed for [1-^{13}C]-pyruvic acid. The solid state polarization build-up curve was fit to the equation:

$$P(t) = P_{eq}\left(1 - \exp\left(\frac{-t}{T_{buildup}}\right)\right) + baseline \qquad [4.1]$$

Where P_{eq} is the equilibrium polarization achieved for the sample and $T_{buildup}$ is the polarization build-up time constant.

The resulting time constant was on the order of 3500s, similar to that observed for the ^{13}C bicarbonate preparation alone. The sample was subsequently dissolved in 6.3mL of water containing 0.3mM ethylenediaminetetraacetic acid (EDTA). The solution was mixed manually in a teardrop flask, and injected using a 5cc syringe into a previously shimmed 10mm NMR tube at 37°C. This process required approximately 15 seconds. Percentage polarizations were quantified in solution by measuring the signal enhancement obtained by DNP polarization compared to the signal at thermal equilibrium. For studies at 3T, an identical polarization procedure was used except 250mg of the sodium bicarbonate solution were used, combined with 4.5μL of pyruvic acid and dissolved using 6.3 mL of water/ EDTA.

Multi-compound polarization of ^{13}C sodium bicarbonate, pyruvic acid, urea and fumaric acid

For studies at 11.7T, the following sample preparations (described above) were placed in a sample cup and frozen in liquid nitrogen: 30.0 μL sodium bicarbonate, 1.0μL pyruvic acid, 6.0μL urea 3.0μL fumaric acid. The compounds were polarized at 94.080 GHz and 1.2-1.4°K for 2h and subsequently dissolved in 5.0mL of 100mM phosphate buffer (pH=7.8). Following dissolution, the sample was treated as above. In a separate set of experiments, identical quantities of these ^{13}C

compounds were individually polarized by the usual method and dissolved using the same buffer.

Hyperpolarized ^{13}C Spectroscopic Studies

All high magnetic field NMR studies were performed on a 11.7T Varian INOVA spectrometer (125MHz ^{13}C, Varian Instruments) using a 10mm $^{15}N/^{31}P/^{13}C$ triple-tuned direct detect probe. For the acquisition of hyperpolarized ^{13}C spectra of bicarbonate and pyruvate eighty proton-decoupled (WALTZ-16, 9000 Hz bandwidth, decoupling during acquisition only) pulse and acquire hyperpolarized ^{13}C NMR spectra (1 average, spectral window = 4000 Hz, number of points= 16000, TR=3.0s, acq time= 500ms, total acq time = 300s) were acquired every 3 sec using a 5° pulse. Spin-lattice (T_1) relaxation times were determined by performing a mono-exponential fit to the signal decay curve of the hyperpolarized compounds. In all cases the r^2 value for the fit was > 0.999 where r = the Pearson product moment correlation coefficient. All spectral measurements were collected at ≈ 37°C. Signal enhancements due to hyperpolarization were calculated by integrating bicarbonate and pyruvate peaks in the first spectrum of the hyperpolarized dynamic experiment, and comparing these to the corresponding peaks in the thermal spectrum, accounting for differences in tip angle and the number of transients obtained.

3T T_1 measurements

All studies were performed using a 3T GE Signa™ scanner (GE Healthcare, Waukesha, WI) equipped with the MNS (multinuclear spectroscopy) hardware package. The RF coil used was a dual-tuned ^{1}H-^{13}C coil used in prior hyperpolarized ^{13}C pyruvate mouse imaging studies(Kohler 2007). For the T_1 measurement experiments, a half-echo FID sequence was used (5° non-selective RF excitation, spectral window of 5 kHz with 2048 points, TR = 3.0s, 64 acquisitions, total acquisition time = 194s). Magnitude spectra were used for data processing, and magnitude decay curves were obtained for pyruvate, pyruvate-hydrate, bicarbonate and CO_2, from which the T_1's were fit to a mono-exponential decay function.

Murine study design

Five mice were imaged: a B6SJL male wild-type mouse (normal), and 4 Transgenic Adenocarcinoma of Mouse Prostate (TRAMP) mice. The coil setup was the same as described above for the T_1 measurements. T_2-weighted ^{1}H images were acquired in three planes using a fast spin-echo (FSE) sequence for anatomical reference. ^{13}C spectroscopic imaging was acquired immediately upon completion of a 15s, 350μL injection of the dissolved co-polarized solution. These used a half-echo FID acquisition, 8x8 matrix size, TR = 130ms (wild-type) or 230ms (TRAMP), TE = 5ms, 10mm slice, 10x10mm in-plane resolution for 1.0cc voxels, and a spectral window of 5000Hz with 512 points (wild-type) or 1024 points (TRAMP). The k-space data was acquired concentrically, with a progressive RF flip angle scheme to utilize all available magnetization. This resulted in a total acquisition time of 8s (wild-type) or 15s (TRAMP). A tube with 8M 13C urea inserted alongside the mouse was used for RF pulse calibration.

Co-polarization of ^{13}C-Sodium Bicarbonate with [1-^{13}C] Pyruvic Acid and T_1 measurements

A preparation method for ^{13}C sodium bicarbonate in glycerol was developed, allowing for reasonable ^{13}C sodium bicarbonate concentrations in the preparation (1.8M ≈ half that achieved previously for cesium bicarbonate(Gallagher 2008)) and a high solution state polarization (12.7 ± 1.9%). Multi-compound polarization of ^{13}C-sodium bicarbonate (1.8M) in glycerol and neat [1-^{13}C] pyruvic acid (14.2M) was performed by freezing the ^{13}C preparations separately within the same sample cup, prior to placement in the polarizer. For both 11.7T (N=3) and 3T experiments (N=3), polarization of samples containing both ^{13}C sodium bicarbonate and ^{13}C pyruvate resulted in a build-up time constant of approximately 3500s, with greater than 95% polarization of the sample achieved at 3.5 hours. This polarization build-up time is longer than the polarization build-up time for ^{13}C pyruvate alone (build-up time constant ≈ 900s) but is comparable to the polarization build-up time of ^{13}C sodium bicarbonate alone. Following dissolution using EDTA/H_2O, the

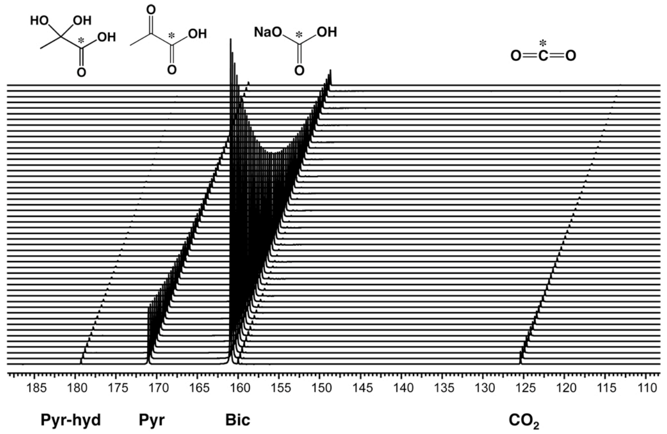

Figure 4.26. Dynamic hyperpolarized spectrum for a co-polarized solution of [1-13C] pyruvate and 13C sodium bicarbonate, with data collected at 11.7T. The final solution pH was 7.8-7.9. The mono-exponential decay for bicarbonate and pyruvate peaks were used to calculate the T1's.

concentrations of ^{13}C bicarbonate and [1-^{13}C] pyruvate were 28.4mM and 5.2mM, respectively, with an average pH of 7.8. The average solution state polarization was 15.7 ± 1.2% for bicarbonate and 17.6 ± 0.9% for pyruvate, which was not significantly different from the percent polarization obtained for each compound alone (**Table 4.4**). Representative data are shown in **Figure 4.26**, which demonstrate large signal enhancements, and mono-exponential decay for [1-^{13}C] pyruvate (171ppm), [1-^{13}C] pyruvate hydrate (179ppm), 13C bicarbonate (161ppm) and ^{13}C carbon dioxide (125ppm), with no significant impurities noted in the hyperpolarized dynamic spectrum.

The carbon dioxide resonance was ≈ 22 fold smaller than the bicarbonate resonance. Calculated mean T_1's at 11.7T were 46.7 ± 0.6 s for bicarbonate, and 47.7 ± 1.1 s for pyruvate. At 3T the mean T_1 values were significantly longer for pyruvate 67.3 ± 2.5 s than at 11.7T. The bicarbonate T_1 was also longer (49.7 ± 2.9 s) at 3T, but this difference was not significant. The measured T_1 of carbon dioxide at 11.7T (44.7 ± 0.6 s) was not significantly less than that of sodium bicarbonate.

Murine Co-polarization Studies

Co-polarized ^{13}C bicarbonate and [1-^{13}C] pyruvate was injected into 1 normal and 4 tumor-bearing TRAMP mice in order to determine whether images of pyruvate metabolism and pH could be simultaneously obtained and that the presence of the ^{13}C bicarbonate did not affect pyruvate metabolism. For animal studies, a larger sample containing both ^{13}C bicarbonate and [1-^{13}C] pyruvate was used, corresponding to injected concentrations of 55mM and 10mM, respectively. As shown in **Figures 4.27 and 4.28**, well resolved hyperpolarized ^{13}C resonances for the labelled carbonyls of [1-^{13}C] pyruvate, [1-^{13}C] pyruvate hydrate, [1-^{13}C] lactate, ^{13}C bicarbonate and ^{13}C carbon dioxide could be observed in both normal mice (**Figure 4.27**) and in tumor containing TRAMP mice (**Figure 4.28**).

The chemical shifts of these compounds were not different from those observed in solution studies. Despite the significantly higher concentration of ^{13}C bicarbonate injected, and in contrast to what was observed in solution (**Figure 4.26**), the observed *in vivo* bicarbonate peak was lower than the pyruvate peak. The ^{13}C carbon dioxide peak observed was on average 22.4 fold lower than the ^{13}C bicarbonate peak.

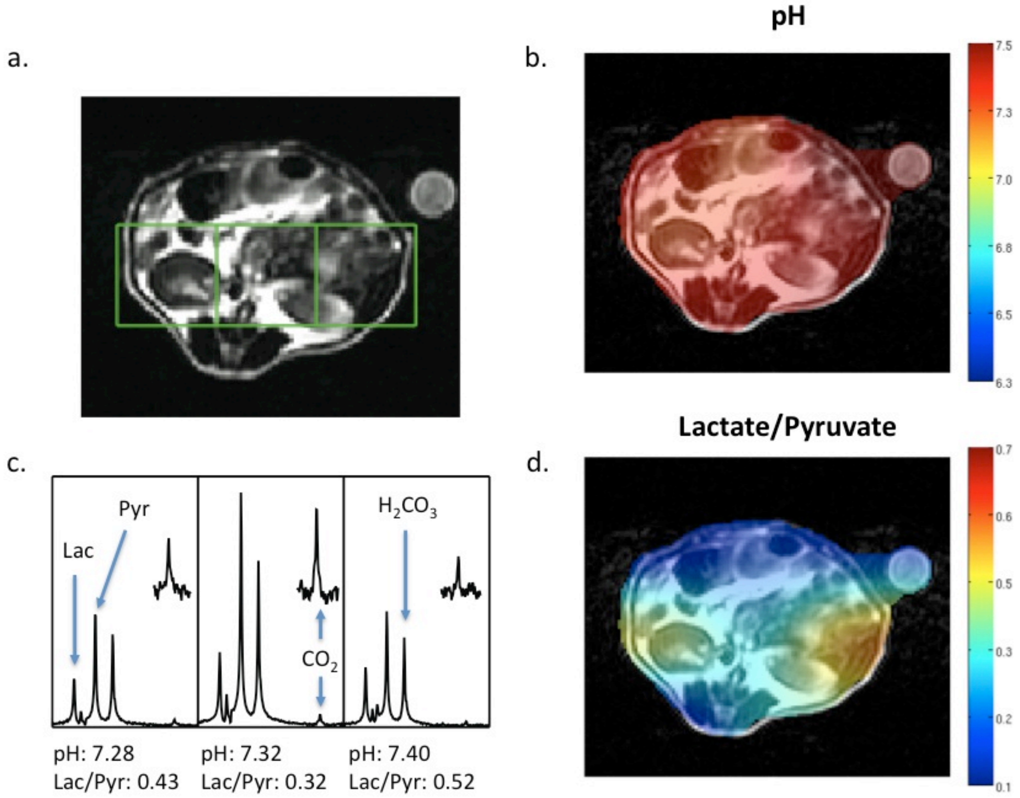

Figure 4.27. *In vivo* data collected at 3T. A T_2-weighted anatomic image (A), pH image of the same slice demonstrating the distribution of calculated pH (B), spectra for the corresponding voxels shown in the T_2-weighted image (C) and the Lactate/Pyruvate ratio image (D) are shown for a wildtype mouse. Following dissolution, 350 μL of a solution with 55mM pre-polarized ^{13}C bicarbonate and 10mM ^{13}C pyruvate were injected intravenously. Data was acquired with a resolution of 1 cm^3. The pH for individual voxels was calculated using the Henderson-Hasselbalch equation and pKa of 6.17 at 37°C. The peak ratios of observed ^{13}C lactate to ^{13}C pyruvate are shown beneath the corresponding spectra. Regions of the CO_2 resonance have been scaled up to demonstrate the signal-to-noise achieved in each voxel.

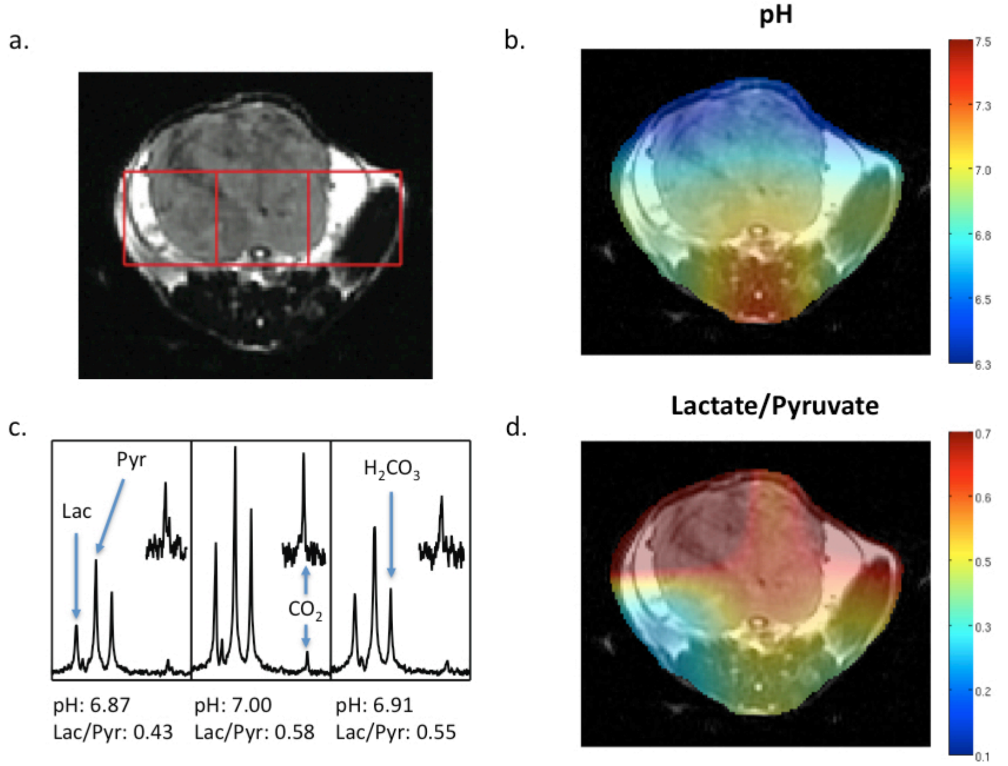

Figure 4.28. *In vivo* data collected at 3T. A T_2-weighted anatomic image (A), pH image of the same slice demonstrating the distribution of pH calculated (B), spectra for the corresponding voxels shown in the T_2-weighted image (C) and the Lactate/Pyruvate ratio image (D) are shown for a TRAMP tumor bearing mouse. The tumor is visible in the upper half of the slice. Following dissolution, 350μL of a solution 55mM in pre-polarized ^{13}C bicarbonate and 10 mM in ^{13}C pyruvate were injected intravenously. Data was acquired with a resolution of 1 cm^3. The pH for individual voxels was calculated using the Henderson-Hasselbalch equation and pKa of 6.17 at 37°C. The peak ratios of observed ^{13}C lactate to ^{13}C pyruvate are also shown beneath the corresponding spectra. Regions of the CO_2 resonance have been scaled up to demonstrate the signal-to-noise achieved in each voxel.

Multi-compound polarization

In order to demonstrate that more than two compounds could be polarized in the same sample without significant loss of T_1 or enhancement, four substrates of metabolic and physiologic interest were polarized: [1-^{13}C] pyruvic acid, ^{13}C sodium bicarbonate, [1,4-^{13}C] fumaric acid, and [1-^{13}C] urea. Again, these compounds were frozen separately in a Hypersense® polarizer sample cup and polarized at a microwave frequency of 94.080 GHz. Since not every compound could be polarized at its ideal frequency, a compromise value was chosen to provide the best simultaneous polarization of the mixture. The multi-polarization had a build-up time constant of approximately 3500s, with greater than 95% polarization of the sample achieved at 3.5 hours identical to the co-polarization, indicating the polarization time was dominated by the slower polarization of ^{13}C sodium bicarbonate. On dissolution using EDTA/H2O, the concentrations of ^{13}C

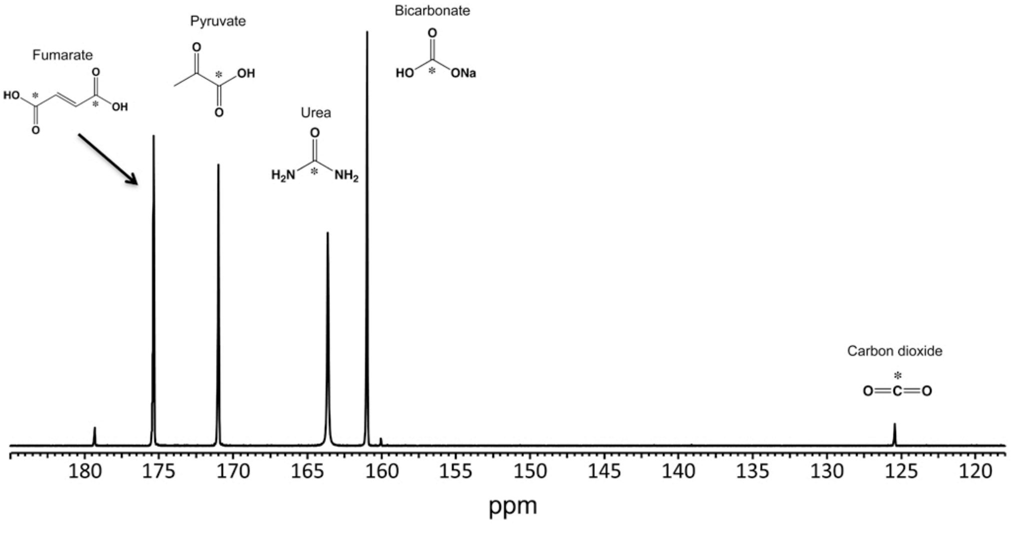

Figure 4.29. Multi-compound polarization of four ^{13}C biomolecules of interest: fumarate, pyruvate, urea, and bicarbonate. These data were obtained 60s following dissolution. Levels of polarization achieved were similar to that obtained for the individual compounds, performed using an optimized microwave frequency. T_1's in solution were similar to those obtained for the separate species. Standard deviations are reported (N=3).

bicarbonate, [1-^{13}C] pyruvate, [1,4-^{13}C] fumaric acid, and [1-^{13}C] urea were 10.8mM, 2.8mM, 2.5mM and 7.8mM respectively, with a measured pH of 7.8-7.9. A representative resulting hyperpolarized spectrum (t=60s) is presented in **Figure 4.29**, with calculated T_1's, and enhancements presented in **Table 4.4**.

Figure 4.29 demonstrates well-resolved resonances for all of the ^{13}C labeled carbonyls; [1-^{13}C] pyruvate (171ppm), [1-^{13}C] pyruvate hydrate (179ppm), ^{13}C bicarbonate (161ppm) and ^{13}C carbon dioxide (125ppm), [1-^{13}C] urea (164ppm) and [1,4-^{13}C] fumurate (175ppm) with one unknown small impurity at 160ppm. In a second set of experiments, the compounds were polarized separately under identical conditions, and dissolved in a high buffering-capacity buffer to ensure a similar pH (7.8) to that observed for the multi-metabolite case. In all cases the calculated T_1's and enhancements were similar, demonstrating that multi-compound polarization can be achieved with minimal if any loss of SNR (**Table 4.4**).

Table 4.4. Spin-lattice relaxation values, and % polarization achieved for multi-compound polarization at 11.7T. T1's and signal enhancements were similar to those observed when the individual compounds were polarized separately and dissolved in an identical 100mM pH 7.8 phosphate buffer.

Compound	T_1 (s) Multipol	T_1 (s) Alone	% polarization Multipol	% polarization Alone
13C bicarbonate	43.3 ± 1.2	48.7 ± 0.6	10.3 ± 1.8	12.7 ± 1.9
[1-13C] pyruvate	48.3 ± 1.5	48.3 ± 0.6	17.5 ± 3.4	17.4 ± 1.5
[1-13C] fumarate	29.0 ± 1.0	29.3 ± 0.6	15.6 ± 1.9	12.0 ± 0.7
[1-13C] urea	43.0 ± 1.0	44.0 ± 0.3	11.6 ± 2.5	12.4 ± 0.4

In this series of experiments, a method for direct polarization of ^{13}C sodium bicarbonate suitable for use in patients was developed, and the co-polarization of ^{13}C sodium bicarbonate and [1-^{13}C] pyruvate in a single intravenous bolus was achieved for the first time. The ^{13}C sodium bicarbonate preparation provided hyperpolarized bicarbonate concentrations that were approximately half (55mM) that previously reported for cesium bicarbonate (100mM), and similar solution state polarizations (≈16%) without the need for chromatography following dissolution to remove the cesium(Gallagher 2008). Consistent with chemical shift anisotropy dominating the T_1 relaxation of carbonyls, the T_1's of ^{13}C bicarbonate and [1-^{13}C] pyruvate were even longer at 3T (49.7s and 67.3s, respectively) as compared to 11.7T(Blicharski 1972; Anet 1992). As predicted by the Henderson-Hasselbalch equation ($pH = pKa + \log_{10}([HCO_3]/[CO_2]$, $pKa = 6.17$)(Gallagher 2008) and the known pH and temperature of the solution, the carbon dioxide resonance was ≈22 fold less than the bicarbonate resonance. However, the co-polarization resulted in sufficiently high solution state polarizations and spin-lattice relaxation times of bicarbonate, carbon dioxide and pyruvate to acquire simultaneous *in vivo* images of interstitial pH and pyruvate metabolism in normal and tumor bearing mice.

Despite the significantly higher concentration of ^{13}C bicarbonate than [1-^{13}C] pyruvate injected in animal in vivo studies, and in contrast to what was observed in solution, the observed in vivo bicarbonate peak was much lower than the pyruvate peak. This reduction in hyperpolarized signal may be the result of ^{13}C carbon dioxide loss during the dissolution process, the much shorter in vivo T_1 of ^{13}C bicarbonate and carbon dioxide(Gallagher 2008), as well as loss of ^{13}C carbon dioxide in the lungs with ventilation. The in vivo T_1 of ^{13}C bicarbonate and carbon dioxide has been previously reported to be ≈10 seconds, much shorter than the ≈50 seconds reported in the solution studies described herein. Most important for *in vivo* measurements of pH is the fact that the T_1 of ^{13}C bicarbonate and carbon dioxide are similar as reported in the solution state in this paper and in vivo previously(Gallagher 2008). The equivalence of the T_1's is most likely due to the rapid inter-conversion of ^{13}C bicarbonate and carbon dioxide, since even in the absence of carbonic anhydrase the exchange is rapid ($\approx 0.1 s^{-1}$) and this exchange is further increased by the enzyme(Gallagher 2008). Moreover, sufficient S/N data were obtained for magnetic resonance spectroscopic imaging studies with a $1 cm^3$ spatial resolution. This relatively coarse spatial resolution was mandated by the roughly 20-fold reduction in ^{13}C CO_2 peak signal-to-noise relative to the ^{13}C bicarbonate peak for pH's in the physiologic range. However, this limitation in sensitivity can be over-come by increasing the amount of hyperpolarized ^{13}C bicarbonate infused. In the current set of studies, the bicarbonate preparation in glycerol was 1.8M, limiting the concentration of injected bicarbonate to 55mM using existing methods on the Oxford Hypersense® polarizer. In patient studies, the ^{13}C bicarbonate concentration should not be a problem since it is often infused in relatively high concentrations into patients, with standard doses being on the order of 150mM, and clinical DNP polarizers would have the ability to polarize and dissolve larger amounts of ^{13}C bicarbonate.

Similar to what has been previously reported for the injection of hyperpolarized [1-^{13}C] pyruvate alone in the normal and TRAMP mouse, the production of significantly higher levels of hyperpolarized [1-^{13}C] lactate were observed in the TRAMP tumor compared to benign tissues in the abdomen of the mouse after injection of co-polarized ^{13}C bicarbonate and [1-^{13}C] pyruvate(Albers 2008). Importantly, the presence of bicarbonate did not change the observed pyruvate metabolism with the same tumor hyperpolarized lactate/pyruvate ratios being obtained when pyruvate was administered alone or in combination with bicarbonate. Rapid equilibration of injected hyperpolarized ^{13}C sodium bicarbonate with ^{13}C CO_2 after injection in mice also allowed the calculation of pH on a voxel by voxel basis as previously described in a study of hyperpolarized ^{13}C cesium bicarbonate in a murine lymphoma model(Gallagher 2008). The TRAMP prostate tumor demonstrated a low pH (pH = 6.87 to 7.00) similar to what has been previously reported for the pH of the EL4 tumor (pH = 6.71 ± 0.14)(Gallagher 2008). Our initial data suggested that the more acidic pH observed in cancerous tissue correlated with increased pyruvate to lactate conversion, supporting the hypothesis that the cellular evolution associated with carcinogenesis selects for lactate-producing glycolytic resulting in microenvironmental acidosis. It has been proposed that this microenvironmental acidosis enables the malignant cells to breakdown and invade neighboring tissue(Gatenby 2004; Gatenby 2006). However, additional studies need to be performed in order to verify the correlation between hyperpolarized lactate production and decreased interstitial pH, and whether decreased tumor pH correlates with increasing pathologic grade as previously shown for hyperpolarized lactate production(Albers 2008).

The co-polarization technique was extended to polarize four ^{13}C labeled substrates providing simultaneous information on pH, metabolism, necrosis and angiogenesis, namely [1-^{13}C] pyruvic acid, ^{13}C sodium bicarbonate, [1,4-^{13}C] fumaric acid, and [1-^{13}C] urea with high levels of solution state polarization (10-20%) and spin-lattice relaxation values (30-50s) similar to those obtained with polarization of the individual hyperpolarized probes. Hyperpolarized ^{13}C urea has already been employed as an intravascular angiographic agent, and could be used in the described agent combination to assess tissue perfusion(Ardenkjaer-Larsen 2003; Golman 2003). [1,4-^{13}C] fumarate represents a point of entry into the citric acid cycle and has recently been shown to be a marker of treatment response through increased production of hyperpolarized malate due to increased cellular necrosis after therapy(in't Zandt 2009). Simultaneous evaluation of enzymatic pathways and other physiologic properties is not easily achieved using other imaging methods including PET, optical imaging, or other targeted MR methods. In addition, concerns about toxicity have limited the proliferation of other intravenous imaging agents, while the endogenous ^{13}C agents included in this multi-polarization approach are anticipated to have minimal untoward effects in humans. As additional new hyperpolarized ^{13}C agents are developed, multi-compound polarization will be a powerful method of probing multiple metabolic pathways and other physiologic properties simultaneously, in a single MR scan lasting only seconds.

Chapter 5: Conclusions and Future Directions

Future work in the area of bioreactor and hyperpolarized NMR probe development will be needed to optimize these tools and provide a robust platform for the investigation of cellular metabolism. While both techniques have been refined for use independently, their combination will require further characterization before they are fully applicable to surrogate systems, such as bio-artificial organs, and quantitative assessment of metabolic processes. Most tissue culture perfusion systems used by cell biologists, have been 'home-built' and lack the sophistication necessary to remove system limitations as a confounding factor in data analysis. Analogously, most hyperpolarized NMR probes have been developed by chemists and physicists, who have greatly pushed the field of low temperature spin physics forward, but have not taken into account the biochemical significance of agents and their application. It was the goal of the studies in this dissertation to make a first attempt at addressing some of the design issues associated with NMR-compatible bioreactors as well as the application of novel hyperpolarized NMR probes.

5.1 Next Generation NMR-compatible Bioreactors

A major limitation of traditional NMR-compatible bioreactors is density of viable cells and tissue. This hindrance is a result of perfusion/diffusion distances inside of the unit. Optimal diffusion distances for O_2, the limiting biochemical substrate (§1.5), require high flow rates to establish axial diffusion at the penalty of shear force damage. This can be overcome by creating microspheres, which can allow for short diffusion distances, but are susceptible to compression and shear force when perfused. Moving spheres are also very difficult to image, limiting their utility for study beyond non-localized spectroscopy under flowing conditions. This becomes more complicated when intra- and extra- cellular compartmentation confounds the understanding of uptake, metabolism and the mathematical modeling of a system.

With these limitations in mind, the first generation cartridge bioreactor was designed to create a static perfused environment. In this system the greater amount of shear force is imposed inside of the hollow fibers, with axial diffusion providing sufficient O_2 and metabolic substrates to the cell mixture or tissue. In the case of embedded cells, by utilizing small diffusion distances, cells can be maintained at a high density to allow for adequate NMR signal. Static cultures also allow for imaging of the bioreactor, which can provide important information about not only the dynamics of the cell system versus the surrounding media, but also about the bioreactor itself. As can be seen in the first iteration of the cartridge bioreactor, there are some interesting flow characteristics that were not anticipated. By using flow imaging, these design issues can be addressed and applied to the study of cellular systems *in vitro*.

The best approach to future studies of bioreactors may be the use of more rigid constructs to allow for more stability and support for the embedded cells. New developments in 3D cell culture design maybe used to create an environment where cells and tissues preferentially grow in orientation and phenotype. Systems that also utilize oxygen carriers to enhance oxygen transport may overcome the diffusion distance minima, which limit bioreactor design. These methods, combined with hyperpolarized techniques to observe kinetics on the order of nanomoles, will greatly enhance the application of *in vitro* cell culture systems to the characterization of real time metabolism.

5.2 Future Development of Hyperpolarized Probes

Along with development of systems where cells and tissue can be maintained at physiologic levels, it is necessary to develop hyperpolarized probes which can provide more insight into the cellular and extracellular characteristics. As a result of the high sensitivity afforded by hyperpolarized NMR, spectroscopic imaging data can be acquired with high spatial and temporal resolution. New techniques have been outlined in this dissertation (§4) to probe different stages of metabolism as well as pH, necrosis, redox and perfusion. Also secondary polarization by chemical reactions such as acetic anhydride may provide the means of tagging peptides and small molecular weight drugs to observe interactions, which are indicative of other processes.

In order to develop new, as well as characterize existing probes, the mechanisms that govern hyperpolarization and the loss of signal must be better understood. Some progress has been made in this dissertation (§4.3) to understand the effect of binding on decrease of hyperpolarized signal, but other mechanisms such as interaction with iron in blood plasma may further decrease hyperpolarized signal. Also changes in relaxation at low field and through changing fields may play a role in the differences in hyperpolarized signal that is observed.

5.3 The "Proof is in the Pudding"

The most difficult aspect of this series of studies has not been the application of techniques, the development of biocompatible systems or the spin physics associated with hyperpolarized NMR. Surprisingly, the proof of utility has been the most elusive. Typical responses to publications lend themselves to comments such as "why do this if you can measure flux by traditional ^{13}C NMR" or "…this is a demonstration of something which can be done – but should not!". These comments arise from a lack of understanding of the potential of such novel techniques. The greater goal of future research must be a demonstration of the power of this combination of techniques, which is generally misunderstood.

"Sometimes you have tell them, tell them again, wait a couple of lines and then hit them over the head with it." With this in mind, future studies will require better visualization of these combined techniques as well as their comparison to traditional gold standards such as mass spectrometry and NMR for fluxomics as well as contrast enhanced MR and PET *in vivo*. It is difficult for the traditional researcher to hear that this technology will allow you to do “what a Biochemist does on an extracted sample in an afternoon, what a Spin physicist can do in an overnight of averaging, and what a Cell Biologist can in weeks of cell experiments” all *in vivo* in less than 1 min. Add in simultaneous measurements and you might as well give up (§4.5). Thus the data needs to be presented as what it is and in the future the power in application to both *in vitro* bioreactor and *in vivo* systems will become increasingly apparent. In conclusion, as one of my thesis committee members has reminded me, sometimes it doesn’t matter how you make it, at the end of the day the “Proof is in the Pudding”.

Appendix A: Fluidized Bioreactor

Drawings of machined bioreactor components are shown for the fluidized bioreactor design.

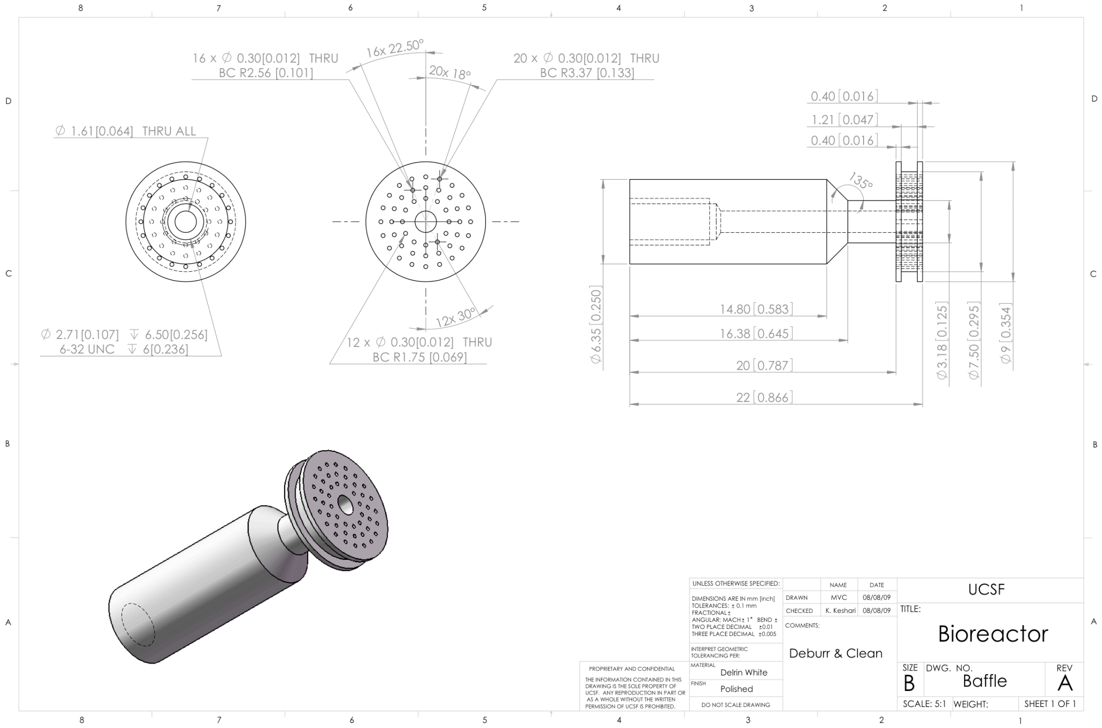

The Baffle was designed with 300um holes so as to keep 500um beads from moving past with perfusion. This was interfaced with a Delrin arm, which fits into the baffle.

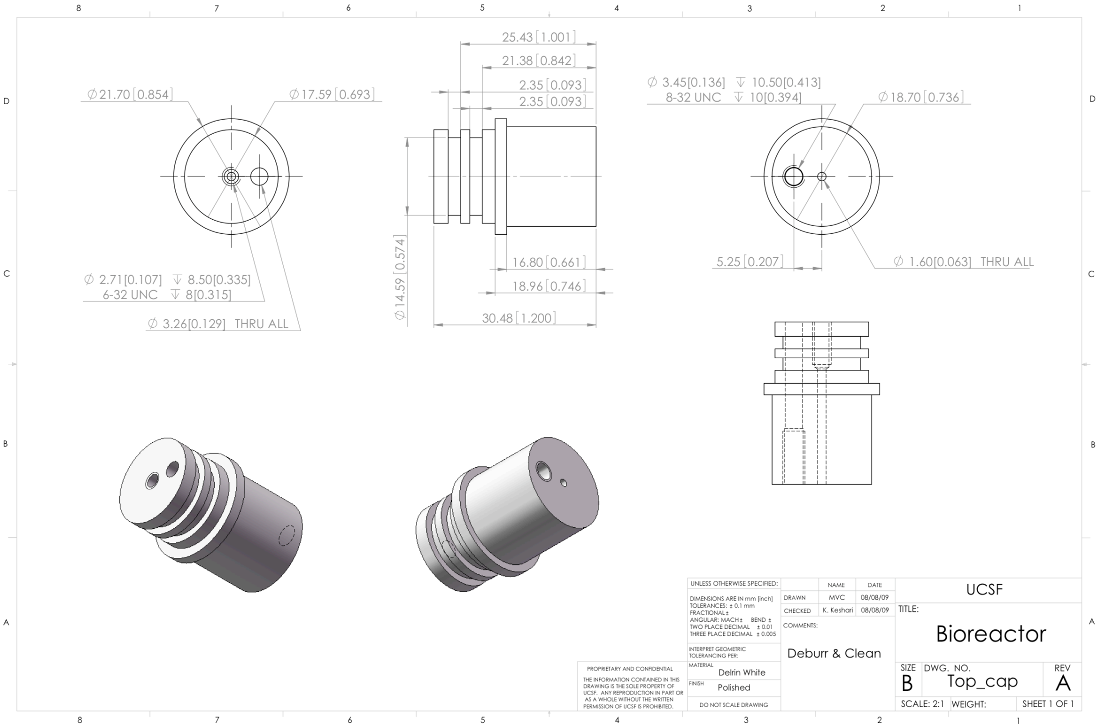

The top cap was designed to fit into the screw top of a standard 10mm wide mouth NMR tube. This part screws into the Delrin arm (as shown below) via a 8/32" plastic screw.

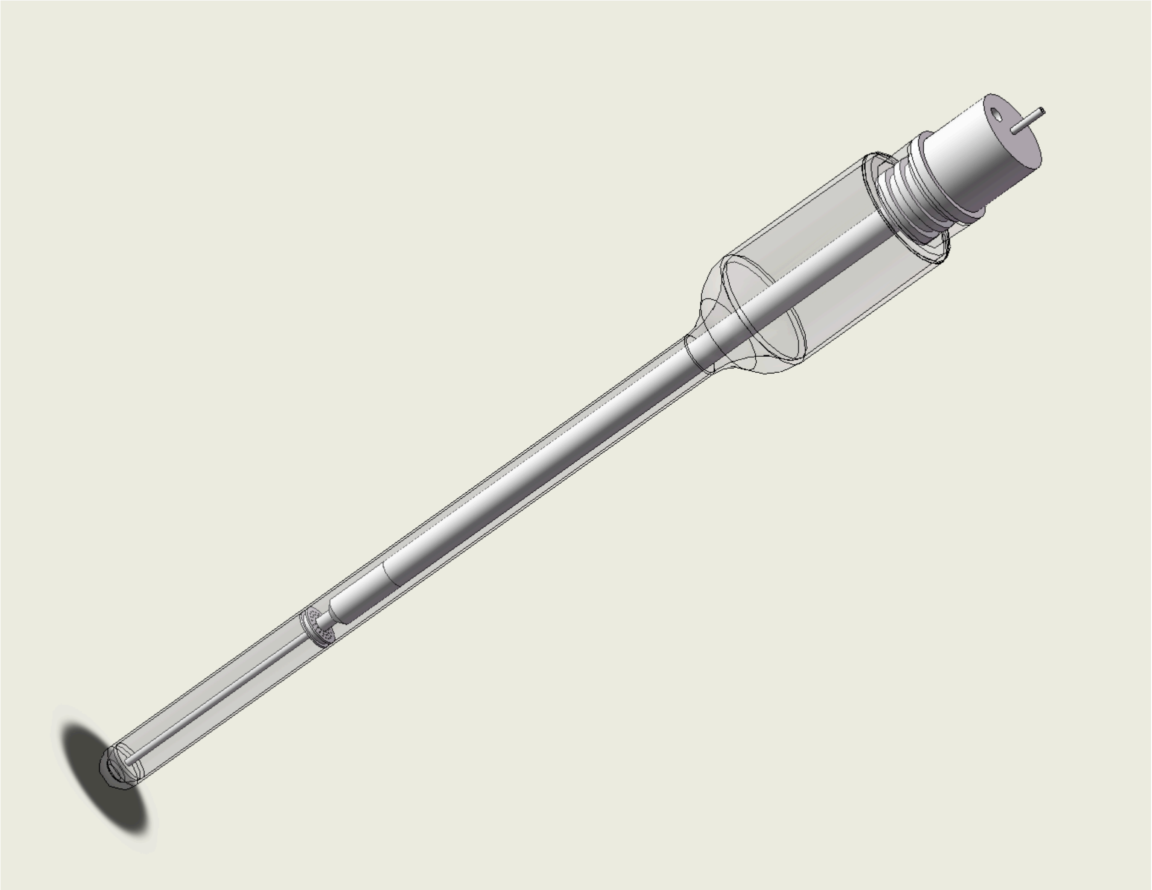

Appendix B: Cartridge Bioreactor

Drawings of machined bioreactor components for the cartridge bioreactor design.

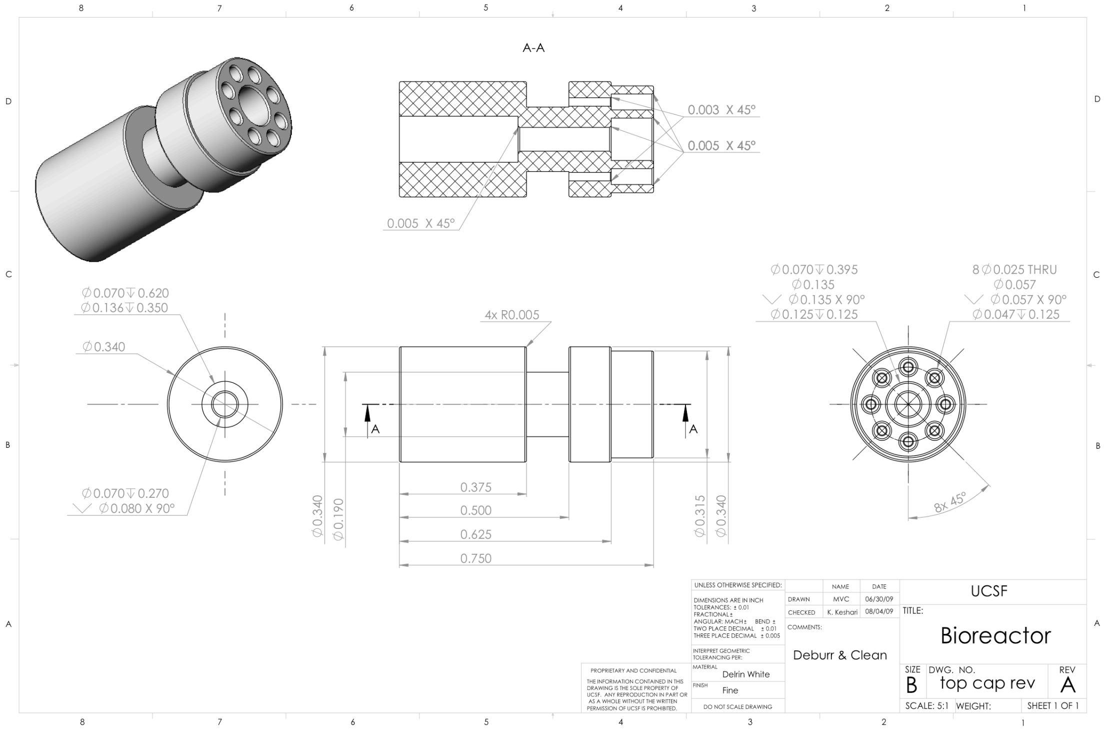

The top cap extrudes into the Ultem 1000 cylinder creating the enclosure for the bioreactor cartridge and support for the hollow fibers, which extrude into the cartridge.

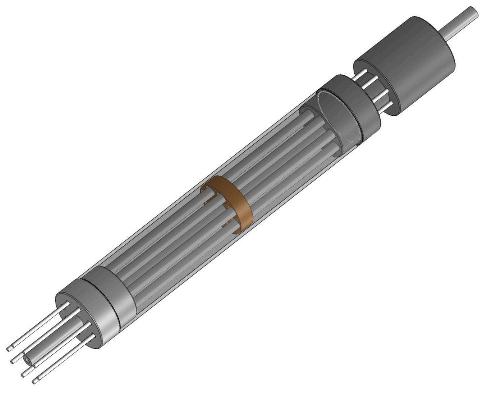

When assembeled, fibers are placed inside the cartridge supported by stainless steel pins. These are removed prior to insertion into the NMR tube shown below.

Appendix C: Culture Media

The culture medium used for the JM1 cell culture studies in Chapter 2 is tabulated below which is standard DMEM 3g/L glucose supplemented with 10% fetal calf serum (FCS) and 100 units/mL penicillin and 100 µg/mL streptomycin.

Compound	mg/L
Calcium cholride	200
Ferric nitrate	0.1
Magnesium sulfate	200
Potassium chloride	400
Sodium bicarbonate	3700
Sodium chloride	6400
Sodium phosphate	125
D-Glucose	3000
Phenol Red Na	15
Sodium pyruvate	110
L-Arginine hydrochloride	84
L-Cystine	48
L-Gluatmine	584
Glycine	30
L-Histidine hydrochloride	42
L-Isoleucine	105
L-Leucine	105
L-Lysine HCl	146
L-Methionine	30
L-Phenylalanine	66
L-Serine	42
L-Threonine	95
L-Tryptophan	16
L-Tyrosine	72
L-Valine	94
D-Calcium panthothenate	4
Choline chloride	4
i-Inositol	7.2
Nicotinamide	4
Pyridoxine hydrochloride	4

Thiamine hydrochloride	4
Folic acid	4
Riboflavin	0.4

The medium formulation used for human prostate tissue slice experiments is shown below, again a modified DMEM medium.

	MW	Conc.	Mass (mg)
1			
L-arginine ·Hcl	210.7	1×10^{-1} M	42.14
Choline chloride	139.6	5×10^{-3} M	1.4
L-histidine ·Hcl ·H_2O	209.6	1×10^{-2} M	4.19
L-isoleucine	131.2	3×10^{-2} M	7.87
L-leucine	131.2	1×10^{-1} M	26.24
L-lysine ·Hcl ·H_2O	182.7	2×10^{-2} M	7.31
L-methionine	149.2	3×10^{-2} M	8.95
L-phenylalnine	165.2	3×10^{-3} M	0.99
L-serine	105.1	1×10^{-2} M	2.1
L-threonine	119.1	1×10^{-1} M	23.82
L-tryptophan	204.2	1×10^{-3} M	0.41
L-valine	117.2	1×10^{-2} M	2.34
L-tyrosine	181.2	3×10^{-3} M	1.09
2			
biotin	244.3	3×10^{-5} M	0.007
Ca ·pantothenate	238.3	1×10^{-4} M	0.024
niacinamide	122.1	3×10^{-5} M	0.004
pyridoxine ·HCl	205.7	3×10^{-5} M	0.006
thiamine ·Hcl	337.5	1×10^{-4} M	0.034
Kcl	74.6	3.8×10^{-1} M	28.348
3			
$Na_2HPO_4 \cdot 7H_2O$	268.1	8.1×10^{-2} M	21.72
folic acid	441.4	3×10^{-4} M	0.13
4			
FeSO4 ·$7H_2O$	278	3×10^{-4} M	0.04
$MgCl_2 \cdot 6H_2O$	203.3	5.2×10^{-2} M	5.29
$MgSO_4 \cdot 7H_2O$	246.5	1.6×10^{-2} M	1.97
$CaCl_2 \cdot 2H_2O$	147	9.2×10^{-2} M	6.76
5			
phenol red · salt	376.4	5.9×10^{-3} M	0.22

6			
Sodium pyruvate	110	2 X 10^{-1} M	22
riboflavin	376.4	1 X 10^{-5} M	0.004
7			
L-cystine	240.3	1.5 X 10^{-2} M	0.72
L-asparagine	150.1	2 X 10^{-2} M	3
L-proline	115.1	6 X 10^{-2} M	6.91
putrescine ·2HCl	161.1	2 X 10^{-4} M	0.032
vitamin B12	1255.4	1 X 10^{-4} M	0.136
L-aspartate	133.1	2 X 10^{-2} M	2.66
L-glutamate	147.1	2 X 10^{-2} M	2.94
L-alanine	89.09	2 X 10^{-2} M	1.78
glycine	75.1	2 X 10^{-2} M	1.5
hypoxanthine	136.1	3 X 10^{-3} M	0.408
6,8 - thioctic acid	206.3	1 X 10^{-4} M	0.021
myo ·inositol	180.2	1 X 10^{-1} M	18.02
thymidine	242.2	3 X 10^{-3} M	0.73
$CuSO_4 \cdot 5H_2O$	249.7	1 X 10^{-6} M	0.00025

Stock	Concentration	Amount (ml)
1	50X	1200
2	100X	200
3	100X	200
5	1,000X	20
6	100X	400
7	100X	800

Additional Compounds	MW	Conc.	Mass (mg)
$ZnSO_4 \cdot 7H_2O$	287.5	5 X 10^{-4} M	0.014
glucose	180.2	7 X 10^{-3} M	25.23
NaCl	58.45	1 X 10^{-1} M	116.9
KH_2PO_4	136.1	4.3 X 10^{-4} M	1.17
L	242.2	2 X 10^{-2} M	58.44
$CuSO_4 \cdot 5H_2O$	238.3	3 X 10^{-2} M	142.98
$NaHCO_3$	84	1.4 X 10^{-2} M	23.52
PFMR-4A		*for 500 ml*	
CT	100 mg/ml	50 ml	10 ng/ml
EGF	100 mg/ml	50 ml	10 ng/ml
BPE	14 mg/ml	1.4 ml	40 mg/ml
PEA	0.1 M	500 ml	0.1 mM

HC	10 mg/ml	50 ml	1 mg/ml
SE	3×10^{-4} M	50 ml	3×10^{-8} M
GENT	40 mg/ml	1.25 ml	100 mg/ml
RA	0.1 mg/ml	50 ml	0.01 ng/ml
IN	4 mg/ml	500 ml	4 mg/ml
VIT E	2.3×10^{-2} M	50 ml	2.3×10^{-6} M

REFERENCES

Abragam A (1955). "Overhauser Effect in Nonmetals." *Phys. Rev.* **98**(6): 1729-1735.

Abragam A and Goldman M (1978). "Principles of dynamic nuclear polarisation." *Rep. Prog. Phys.* **41**.

Abragam A and Proctor WG (1958). *Phys Rev*(109): 1441.

Ackerstaff E, Glunde K and Bhujwalla ZM (2003). "Choline phospholipid metabolism: a target in cancer cells?" *J. Cell. Biochem.* **90**(3): 525-33.

Ackerstaff E, Pflug BR, Nelson JB and Bhujwalla ZM (2001). "Detection of increased choline compounds with proton nuclear magnetic resonance spectroscopy subsequent to malignant transformation of human prostatic epithelial cells." *Cancer Res.* **61**(9): 3599-603.

Albers MJ, Bok R, Chen AP, Cunningham CH, Zierhut ML, Zhang VY, Kohler SJ, Tropp J, Hurd RE, Yen Y-F, Nelson SJ, Vigneron DB and Kurhanewicz J (2008). "Hyperpolarized 13C lactate, pyruvate, and alanine: noninvasive biomarkers for prostate cancer detection and grading." *Cancer Res.* **68**(20): 8607-15.

Albers MJ, Butler TN, Rahwa I, Bao N, Keshari KR, Swanson MG and Kurhanewicz J (2009). "Evaluation of the ERETIC method as an improved quantitative reference for 1H HR-MAS spectroscopy of prostate tissue." *Magnetic resonance in medicine : official journal of the Society of Magnetic Resonance in Medicine / Society of Magnetic Resonance in Medicine* **61**(3): 525-32.

Ande SR, Chen J and Maddika S (2009). "The ubiquitin pathway: An emerging drug target in cancer therapy." *Eur J Pharmacol*.

Anet FAL and O'Leary DJ (1992). "The Shielding Tensor." *Concepts in Magnetic Resonance* **4**: 35-52.

Antoniewicz MR, Kelleher JK and Stephanopoulos G (2006). "Determination of confidence intervals of metabolic fluxes estimated from stable isotope measurements." *Metab Eng* **8**(4): 324-37.

Ardenkjaer-Larsen JH, Fridlund B, Gram A, Hansson G, Hansson L, Lerche MH, Servin R, Thaning M and Golman K (2003). "Increase in signal-to-noise ratio of > 10,000 times in liquid-state NMR." *Proc. Natl. Acad. Sci. U.S.A.* **100**(18): 10158-63.

Aree T and Chaichit N (2003). "Crystal structure of beta-cyclodextrin-benzoic acid inclusion complex." *Carbohydr. Res.* **338**(5): 439-46.

Bailey SM and Cunningham CC (1998). "Acute and chronic ethanol increases reactive oxygen species generation and decreases viability in fresh, isolated rat hepatocytes." *Hepatology* **28**(5): 1318-26.

Bais R, James HM, Rofe AM and Conyers RA (1985). "The purification and properties of human liver ketohexokinase. A role for ketohexokinase and fructose-bisphosphate aldolase in the metabolic production of oxalate from xylitol." *Biochem J* **230**(1): 53-60.

Bakker WH, Albert R, Bruns C, Breeman WA, Hofland LJ, Marbach P, Pless J, Pralet D, Stolz B, Koper JW and et al. (1991). "[111In-DTPA-D-Phe1]-octreotide, a potential radiopharmaceutical for imaging of somatostatin receptor-positive tumors: synthesis, radiolabeling and in vitro validation." *Life Sci* **49**(22): 1583-91.

Balendiran GK, Dabur R and Fraser D (2004). "The role of glutathione in cancer." *Cell Biochem Funct* **22**(6): 343-52.

Bast RC, Jr., Badgwell D, Lu Z, Marquez R, Rosen D, Liu J, Baggerly KA, Atkinson EN, Skates S, Zhang Z, Lokshin A, Menon U, Jacobs I and Lu K (2005). "New tumor markers: CA125 and beyond." *Int J Gynecol Cancer* **15 Suppl 3**: 274-81.

Beloueche-Babari M, Jackson LE, Al-Saffar NMS, Eccles SA, Raynaud FI, Workman P, Leach MO and Ronen SM (2006). "Identification of magnetic resonance detectable metabolic changes associated with inhibition of phosphoinositide 3-kinase signaling in human breast cancer cells." *Mol Cancer Ther* **5**(1): 187-96.

Benelli R and Albini A (1999). "In vitro models of angiogenesis: the use of Matrigel." *Int J Biol Markers* **14**(4): 243-6.

Bental M, Pick U, Avron M and Degani H (1990). "Metabolic studies with NMR spectroscopy of the alga Dunaliella salina trapped within agarose beads." *Eur J Biochem* **188**(1): 111-6.

Blicharski JS (1972). "Nuclear Magnetic Relaxation by Anisotropy of the Chemical Shift." *Z. Naturforsch* **A**(27): 1456-1458.

Bollard ME, Stanley EG, Lindon JC, Nicholson JK and Holmes E (2005). "NMR-based metabonomic approaches for evaluating physiological influences on biofluid composition." *NMR Biomed* **18**(3): 143-62.

Bonarius HP, Ozemre A, Timmerarends B, Skrabal P, Tramper J, Schmid G and Heinzle E (2001). "Metabolic-flux analysis of continuously cultured hybridoma cells using (13)CO(2) mass spectrometry in combination with (13)C-lactate nuclear magnetic resonance spectroscopy and metabolite balancing." *Biotechnol Bioeng* **74**(6): 528-38.

Borghini M (1968). "SPIN-TEMPERATURE MODEL OF NUCLEAR DYNAMIC POLARIZATION USING FREE RADICALS." *Physical Review Letters* **20**: 419-421.

Bowen S and Hilty C (2008). 49th Experimental NMR Conference, Sante Fe, New Mexico.

Bowers CR and Weitekamp DP (1987). "Parahydrogen and Synthesis Allow Dramatically Enhanced Nuclear Alignment " *J. Am. Chem. Soc.*(109): 5541-5542.

Bruni P, Conti C, Giorgini E, Pisani M, Rubini C and Tosi G (2004). "Histological and microscopy FT-IR imaging study on the proliferative activity and angiogenesis in head and neck tumours." *Faraday Discuss.* **126**: 19-26; discussion 77-92.

Bullwinkel J, Baron-Luhr B, Ludemann A, Wohlenberg C, Gerdes J and Scholzen T (2006). "Ki-67 protein is associated with ribosomal RNA transcription in quiescent and proliferating cells." *J Cell Physiol* **206**(3): 624-35.

Burgess SC, Weis B, Jones JG, Smith E, Merritt ME, Margolis D, Dean Sherry A and Malloy CR (2003). "Noninvasive evaluation of liver metabolism by 2H and 13C NMR isotopomer analysis of human urine." *Anal. Biochem.* **312**(2): 228-34.

Burgner JW, Ainslie GR, Cleland WW and Ray WJ (1978). "Bimodal substrate inhibition of lactate dehydrogenase. Factors affecting the enzyme in vivo." *Biochemistry* **17**(9): 1646-53.

Burgner JW and Ray WJ (1974). "A study of pyruvate-induced inhibition in the dogfish lactate dehydrogenase system. Mechanistic comparison with the iodination of pyruvate." *Biochemistry* **13**(20): 4229-37.

Busch J, Cruse A and Marquardt W (2007). "Modeling submerged hollow-fiber membrane filtration for wastewater treatment." *Journal of Membrane Science* **288**(1-2): 94-111.

Canet D, Aroulanda C, Mutzenhardt P, Aime S, Gobetto R and Reineri F (2006). "Para-hydrogen enrichment and hyperpolarization." *Concepts Magn. Reson.* **28A**(5): 321-330.

Chandrasekaran P, Seagle C, Rice L, Macdonald JM and Gerber DA (2006). "Functional analysis of encapsulated hepatic progenitor cells." *Tissue Eng* **12**(7): 2001-8.

Chen AP, Albers MJ, Cunningham CH, Kohler SJ, Yen YF, Hurd RE, Tropp J, Bok R, Pauly JM, Nelson SJ, Kurhanewicz J and Vigneron DB (2007). "Hyperpolarized C-13 spectroscopic imaging of the TRAMP mouse at 3T-initial experience." *Magn Reson Med* **58**(6): 1099-106.

Chen AP, Cunningham CH, Ozturk-Isik E, Xu D, Hurd RE, Kelley DAC, Pauly JM, Kurhanewicz J, Nelson SJ and Vigneron DB (2007). "High-speed 3T MR spectroscopic imaging of prostate with flyback echo-planar encoding." *Journal of magnetic resonance imaging : JMRI* **25**(6): 1288-92.

Chen AP, Kurhanewicz J, Bok R, Xu D, Joun D, Zhang V, Nelson SJ, Hurd RE and Vigneron DB (2008). "Feasibility of using hyperpolarized [1-13C]lactate as a substrate for in vivo metabolic 13C MRSI studies." *Magnetic resonance imaging* **26**(6): 721-6.

Chowdhury SKR, Gemin A and Singh G (2005). "High activity of mitochondrial glycerophosphate dehydrogenase and glycerophosphate-dependent ROS production in prostate cancer cell lines." *Biochem Biophys Res Commun* **333**(4): 1139-45.

Christofk HR, Vander Heiden MG, Harris MH, Ramanathan A, Gerszten RE, Wei R, Fleming MD, Schreiber SL and Cantley LC (2008). "The M2 splice isoform of pyruvate kinase is important for cancer metabolism and tumour growth." *Nature* **452**(7184): 230-3.

Ciriolo MR, Palamara AT, Incerpi S, Lafavia E, Bue MC, De Vito P, Garaci E and Rotilio G (1997). "Loss of GSH, oxidative stress, and decrease of intracellular pH as sequential steps in viral infection." *J Biol Chem* **272**(5): 2700-8.

Constantinidis I, Simpson NE, Grant SC, Blackband SJ, Long RC, Jr. and Sambanis A (2006). "Non-invasive monitoring of tissue-engineered pancreatic constructs by NMR techniques." *Adv Exp Med Biol* **585**: 261-76.

Cook PF and Cleland WW (2007). Enzyme kinetics and mechanism, Garland Science.

Costello LC and Franklin RB (2005). "'Why do tumour cells glycolyse?': from glycolysis through citrate to lipogenesis." *Mol Cell Biochem* **280**(1-2): 1-8.

Cowin GJ, Willgoss DA, Bartley J and Endre ZH (1996). "Serine isotopmer analysis by 13C-NMR defines glycine-serine interconversion in situ in the renal proximal tubule." *Biochim Biophys Acta* **1310**(1): 32-40.

Cowin GJ, Willgoss DA and Endre ZH (1996). "Modulation of glycine-serine interconversion by TCA and glycolytic intermediates in normoxic and hypoxic proximal tubules." *Biochim Biophys Acta* **1310**(1): 41-7.

Cunningham C, Chen A, Lustig M, Lupo J, Xu D, Kurhanewicz J, Hurd R, Pauly J, Nelson SJ and Vigneron DB (2008). "Pulse sequence for dynamic volumetric imaging of hyperpolarized metabolic products." *J Magn Reson*.

Daly PF, Lyon RC, Straka EJ and Cohen JS (1988). "31P-NMR spectroscopy of human cancer cells proliferating in a basement membrane gel." *FASEB J* **2**(10): 2596-604.

Day SE, Kettunen MI, Gallagher FA, Hu DE, Lerche M, Wolber J, Golman K, Ardenkjaer-Larsen JH and Brindle KM (2007). "Detecting tumor response to treatment using hyperpolarized 13C magnetic resonance imaging and spectroscopy." *Nat Med* **13**(11): 1382-7.

de Boer W, Borghini M, Morimoto K, Niinikoski TO and Udo F (1974). "Dynamic polarization of protons, deuterons, and carbon-13 nuclei: Thermal contact between nuclear spins and an electron spin-spin interaction reservoir." *Journal of Low Temperature Physics* **15**: 249-267.

De Graaf RA, Brown PB, Mason GF, Rothman DL and Behar KL (2003). "Detection of [1,6-13C2]-glucose metabolism in rat brain by in vivo 1H-[13C]-NMR spectroscopy." *Magnetic resonance in medicine : official journal of the Society of Magnetic Resonance in Medicine / Society of Magnetic Resonance in Medicine* **49**(1): 37-46.

DeBerardinis RJ, Lum JJ, Hatzivassiliou G and Thompson CB (2008). "The biology of cancer: metabolic reprogramming fuels cell growth and proliferation." *Cell Metab* **7**(1): 11-20.

DeBerardinis RJ, Mancuso A, Daikhin E, Nissim I, Yudkoff M, Wehrli S and Thompson CB (2007). "Beyond aerobic glycolysis: transformed cells can engage in glutamine metabolism that exceeds the requirement for protein and nucleotide synthesis." *Proc Natl Acad Sci USA* **104**(49): 19345-50.

Deichmann R, Hahn D and Haase A (1999). "Fast T-1 mapping on a whole-body scanner." *Magnetic Resonance in Medicine* **42**(1): 206-209.

Denko NC (2008). "Hypoxia, HIF1 and glucose metabolism in the solid tumour." *Nat Rev Cancer*.

Dhimitruka I, Velayutham M, Bobko AA, Khramtsov VV, Villamena FA, Hadad CM and Zweier JL (2007). "Large-scale synthesis of a persistent trityl radical for use in biomedical EPR applications and imaging." *Bioorg Med Chem Lett* **17**(24): 6801-5.

Dillon WP and Nelson S (1999). "What is the role of MR spectroscopy in the evaluation and treatment of brain neoplasms?" *AJNR Am J Neuroradiol* **20**(1): 2-3.

Donnelly KL, Smith CI, Schwarzenberg SJ, Jessurun J, Boldt MD and Parks EJ (2005). "Sources of fatty acids stored in liver and secreted via lipoproteins in patients with nonalcoholic fatty liver disease." *J. Clin. Invest.* **115**(5): 1343-51.

Douard V and Ferraris RP (2008). "Regulation of the fructose transporter GLUT5 in health and disease." *Am J Physiol Endocrinol Metab* **295**(2): E227-37.

Droste P, Weitzel M and Wiechert W (2008). "Visual exploration of isotope labeling networks in 3D." *Bioprocess and biosystems engineering* **31**(3): 227-39.

Edick MJ, Tesfay L, Lamb LE, Knudsen BS and Miranti CK (2007). "Inhibition of integrin-mediated crosstalk with epidermal growth factor receptor/Erk or Src signaling pathways in autophagic prostate epithelial cells induces caspase-independent death." *Mol Biol Cell* **18**(7): 2481-90.

Fan T and Lane A (2008). "Structure-based profiling of metabolites and isotopomers by NMR." *Progress in Nuclear Magnetic Resonance Spectroscopy* **52**(2-3): 69-117.

Fan T, Lane A, Higashi R, Farag M, Gao H, Bousamra M and Miller D (2009). "Altered regulation of metabolic pathways in human lung cancer discerned by 13C stable isotope-resolved metabolomics (SIRM)." *Mol Cancer* **8**(1): 41.

Fan TWM, Kucia M, Jankowski K, Higashi RM, Ratajczak J, Ratajczak MZ and Lane AN (2008). "Rhabdomyosarcoma cells show an energy producing anabolic metabolic phenotype compared with primary myocytes." *Mol Cancer* **7**: 79.

Farghali H, Caraceni P, Rilo HL, Borle AB, Gasbarrini A, Gavaler JS and Van Thiel DH (1996). "Biochemical and 31P-NMR spectroscopic evaluation of immobilized perfused rat Sertoli cells." *J Lab Clin Med* **128**(4): 408-16.

Farghali H, Rossaro L, Gavaler JS, Van Thiel DH, Dowd SR, Williams DS and Ho C (1992). "31P-NMR spectroscopy of perifused rat hepatocytes immobilized in agarose threads: application to chemical-induced hepatotoxicity." *Biochim. Biophys. Acta* **1139**(1-2): 105-14.

Farrell G and Larter C (2006). "Nonalcoholic fatty liver disease: from steatosis to cirrhosis." *Hepatology* **43**(2 Suppl 1): S99-S112.

Fick A (1855). "On Liquid Diffusion." *Philos. Mag. J. Sci.* **10**: 31-39.

Fielding L (2007). "NMR methods for the determination of protein-ligand dissociation constants." *Progress in Nuclear Magnetic Resonance Spectroscopy* **51**: 219-242.

Filippone M, Camastra F, Masulli F and Rovetta S (2008). "A survey of kernel and spectral methods for clustering." *Pattern Recognition* **41**: 176-190.

From AM, Bartholmai BJ, Williams AW, Cha SS and McDonald FS (2008). "Mortality associated with nephropathy after radiographic contrast exposure." *Mayo Clin Proc* **83**(10): 1095-100.

Frydman L and Blazina D (2007). "Ultrafast two-dimensional nuclear magnetic resonance spectroscopy of hyperpolarized solutions." *NATURE PHYSICS* **3**: 415-419.

Funari V, Herrera V, Freeman D and Tolan D (2005). "Genes required for fructose metabolism are expressed in Purkinje cells in the cerebellum." *Molecular Brain Research* **142**(2): 115-122.

Gabellieri C, Beloueche-Babari M, Jamin Y, Payne GS, Leach MO and Eykyn TR (2009). "Modulation of choline kinase activity in human cancer cells observed by dynamic 31P NMR." *NMR Biomed.* **22**(4): 456-61.

Gallagher FA, Kettunen MI, Day SE, Hu DE, Ardenkjaer-Larsen JH, in't Zandt R, Jensen PR, Karlsson M, Golman K, Lerche MH and Brindle KM (2008). "Magnetic resonance imaging of pH in vivo using hyperpolarized C-13-labelled bicarbonate." *Nature* **453**(7197): 940-U73.

Gallagher FA, Kettunen MI, Day SE, Lerche M and Brindle KM (2008). "13C MR spectroscopy measurements of glutaminase activity in human hepatocellular carcinoma cells using hyperpolarized 13C-labeled glutamine." *Magnetic resonance in medicine : official journal of the Society of Magnetic Resonance in Medicine / Society of Magnetic Resonance in Medicine* **60**(2): 253-7.

Galons JP, Job C and Gillies R (1995). "Increase of GPC levels in cultured mammalian cells during acidosis. A 31P MR spectroscopy study using a continuous bioreactor system." *Magnetic resonance in medicine : official journal of the*

Society of Magnetic Resonance in Medicine / Society of Magnetic Resonance in Medicine **33**(3): 422-6.

Gamcsik M, Ford J, Millis K and McGovern K (1996). "A versatile oxygenator and perfusion system for magnetic resonance studies." *Biotechnol Bioeng* **49**(3): 348-354.

Gamcsik MP (1999). "13C-Isotopic enrichment of glutathione in cell extracts determined by nuclear magnetic resonance spectroscopy." *Anal. Biochem.* **266**(1): 58-65.

Gamcsik MP, Bierbryer RG and Millis KK (2004). "Noninvasive monitoring of glutathione turnover in perfused MCF-7 cells." *Free Radic. Biol. Med.* **37**(7): 961-8.

Gamcsik MP, Dubay GR and Cox BR (2002). "Increased rate of glutathione synthesis from cystine in drug-resistant MCF-7 cells." *Biochem Pharmacol* **63**(5): 843-51.

Ganapathy V, Thangaraju M and Prasad PD (2008). "Nutrient transporters in cancer: Relevance to Warburg hypothesis and beyond." *Pharmacol Ther*.

Gartland KP, Beddell CR, Lindon JC and Nicholson JK (1991). "Application of pattern recognition methods to the analysis and classification of toxicological data derived from proton nuclear magnetic resonance spectroscopy of urine." *Mol Pharmacol* **39**(5): 629-42.

Gasbarrini A, Borle AB, Farghali H, Bender C, Francavilla A and Van Thiel D (1992). "Effect of anoxia on intracellular ATP, Na+i, Ca2+i, Mg2+i, and cytotoxicity in rat hepatocytes." *J. Biol. Chem.* **267**(10): 6654-63.

Gatenby RA, Gawlinski ET, Gmitro AF, Kaylor B and Gillies R (2006). "Acid-mediated tumor invasion: a multidisciplinary study." *Cancer Res.* **66**(10): 5216-23.

Gatenby RA and Gillies RJ (2004). "Why do cancers have high aerobic glycolysis?" *Nat. Rev. Cancer* **4**(11): 891-9.

Gatenby RA and Gillies RJ (2007). "Glycolysis in cancer: A potential target for therapy." *Int J Biochem Cell Biol*.

Gillies R, Liu Z and Bhujwalla ZM (1994). "31P-MRS measurements of extracellular pH of tumors using 3-aminopropylphosphonate." *Am J Physiol* **267**(1 Pt 1): C195-203.

Gillies RJ, Galons JP, McGovern KA, Scherer PG, Lien YH, Job C, Ratcliff R, Chapa F, Cerdan S and Dale BE (1993). "Design and application of NMR-compatible bioreactor circuits for extended perfusion of high-density mammalian cell cultures." *NMR Biomed.* **6**(1): 95-104.

Gillies RJ and Gatenby RA (2007). "Hypoxia and adaptive landscapes in the evolution of carcinogenesis." *Cancer Metastasis Rev*.

Gillies RJ, Scherer PG, Raghunand N, Okerlund LS, Martinez-Zaguilan R, Hesterberg L and Dale BE (1991). "Iteration of hybridoma growth and productivity in hollow fiber bioreactors using 31P NMR." *Magn Reson Med* **18**(1): 181-92.

Goel HL, Li J, Kogan S and Languino LR (2008). "Integrins in prostate cancer progression." *Endocr Relat Cancer* **15**(3): 657-64.

Goldman M, Jóhannesson H, Axelsson O and Karlsson M (2005). "Hyperpolarization of 13C through order transfer from parahydrogen: a new contrast agent for MRI." *Magnetic resonance imaging* **23**(2): 153-7.

Golman K, Ardenkjaer-Larsen JH, Petersson JS, Mansson S and Leunbach I (2003). "Molecular imaging with endogenous substances." *Proc. Natl. Acad. Sci. U.S.A.* **100**(18): 10435-9.

Golman K, Axelsson O, Johannesson H, Mansson S, Olofsson C and Petersson JS (2001). "Parahydrogen-induced polarization in imaging: subsecond (13)C angiography." *Magn Reson Med* **46**(1): 1-5.

Golman K, Zandt RI, Lerche M, Pehrson R and Ardenkjaer-Larsen JH (2006). "Metabolic imaging by hyperpolarized 13C magnetic resonance imaging for in vivo tumor diagnosis." *Cancer Res* **66**(22): 10855-60.

Goo YA and Liu AY (2005). "Proenkephalin (PENK): A candidate stromal mesenchyme cell gene in epithelial differentiation whose expression is down-regulated in cancer." *Journal of Urology* **173**(4): 387-388.

Goodson BM (2002). "Nuclear magnetic resonance of laser-polarized noble gases in molecules, materials, and organisms." *J. Magn. Reson.* **155**(2): 157-216.

Goux WJ (1985). "Complex Isomerization of Ketoses - a C-13 Nmr-Study of the Base-Catalyzed Ring-Opening and Ring-Closing Rates of D-Fructose Isomers in Aqueous-Solution." *Journal of the American Chemical Society* **107**(14): 4320-4327.

Gross JD, Constantinidis I and Sambanis A (2007). "Modeling of encapsulated cell systems." *Journal of Theoretical Biology* **244**(3): 500-10.

Gruetter R, Adriany G, Choi I-Y, Henry P-G, Lei H and Oz G (2003). "Localized in vivo 13C NMR spectroscopy of the brain." *NMR in biomedicine* **16**(6-7): 313-38.

Hanigan MH, Gallagher BC, Townsend DM and Gabarra V (1999). "Gamma-glutamyl transpeptidase accelerates tumor growth and increases the resistance of tumors to cisplatin in vivo." *Carcinogenesis* **20**(4): 553-9.

Heath CA, Belfort G, Hammer BE, Mirer SD and Pimbley JM (1990). "Magnetic Resonance Imaging and Modeling of Flow in Hollow-Fiber Bioreactors." *AIChe Journal* **36**(4): 547-558.

Hohn-Berlage M, Okada Y, Kloiber O and Hossmann KA (1989). "Imaging of brain tissue pH and metabolites. A new approach for the validation of volume-selective NMR spectroscopy." *NMR Biomed* **2**(5-6): 240-5.

Hsu PP and Sabatini DM (2008). "Cancer cell metabolism: warburg and beyond." *Cell* **134**(5): 703-7.

Hu S, Lustig M, Chen AP, Crane J, Kerr A, Kelley DA, Hurd R, Kurhanewicz J, Nelson SJ, Pauly JM and Vigneron DB (2008). "Compressed sensing for resolution enhancement of hyperpolarized 13C flyback 3D-MRSI." *J Magn Reson* **192**(2): 258-64.

Huynh M, Luiken JJ, Coumans W and Bell R (2008). "Dietary fructose during the suckling period increases body weight and fatty acid uptake into skeletal muscle in adult rats." *Obesity (Silver Spring)* **16**(8): 1755-62.

in't Zandt R, Kettunen MI, Karlsson M, Rose Jensen P, Gisselsson A, Gallagher FA, Hu DE, Hansson G, Brindle KM and Lerche M (2009). 13C-labeled malate as a treatment response marker in a murine lymphoma model in vivo. ISMRM. Honolulu, Hawaii**:** 55.

Iorio E, Mezzanzanica D, Alberti P, Spadaro F, Ramoni C, D'Ascenzo S, Millimaggi D, Pavan A, Dolo V, Canevari S and Podo F (2005). "Alterations of choline phospholipid metabolism in ovarian tumor progression." *Cancer Res.* **65**(20): 9369-76.

Jucker BM, Lee JY and Shulman RG (1998). "In vivo 13C NMR measurements of hepatocellular tricarboxylic acid cycle flux." *J. Biol. Chem.* **273**(20): 12187-94.

Kaplan O and Cohen JS (1991). "Lymphocyte activation and phospholipid pathways. 31P magnetic resonance studies." *J Biol Chem* **266**(6): 3688-94.

Kaplan O and Cohen JS (1994). "Metabolism of breast cancer cells as revealed by non-invasive magnetic resonance spectroscopy studies." *Breast Cancer Res Treat* **31**(2-3): 285-99.

Keshari KR, Kurhanewicz J, Bok R, Chen A, Wilson D, Jeffries R, Criekinge MV, Vigneron D and Macdonald J (2008). "Characterization of a hepatoma cell line in a novel 3D bioreactor flow system using hyperpolarized 13C MRS." *International Society of Magnetic Resonance*.

Keshari KR, Lotz JC, Kurhanewicz J and Majumdar S (2005). "Correlation of HR-MAS spectroscopy derived metabolite concentrations with collagen and proteoglycan levels and Thompson grade in the degenerative disc." *Spine* **30**(23): 2683-8.

Keshari KR, Lotz JC, Link TM, Hu S, Majumdar S and Kurhanewicz J (2008). "Lactic acid and proteoglycans as metabolic markers for discogenic back pain." *Spine* **33**(3): 312-7.

Keshari KR, Zektzer AS, Swanson MG, Majumdar S, Lotz JC and Kurhanewicz J (2005). "Characterization of intervertebral disc degeneration by high-resolution magic angle spinning (HR-MAS) spectroscopy." *Magnetic resonance in medicine : official journal of the Society of Magnetic Resonance in Medicine / Society of Magnetic Resonance in Medicine* **53**(3): 519-27.

King A, Andersson A and Sandler S (2000). "Cytokine-induced functional suppression of microencapsulated rat pancreatic islets in vitro." *Transplantation* **70**(2): 380-3.

Kohler SJ, Yen Y, Wolber J, Chen AP, Albers MJ, Bok R, Zhang V, Tropp J, Nelson S, Vigneron DB, Kurhanewicz J and Hurd RE (2007). "In vivo 13 carbon metabolic imaging at 3T with hyperpolarized 13C-1-pyruvate." *Magn Reson Med* **58**(1): 65-9.

Kroemer G and Pouyssegur J (2008). "Tumor cell metabolism: cancer's Achilles' heel." *Cancer Cell* **13**(6): 472-82.

Kurhanewicz J, Dahiya R, Macdonald JM, Jajodia P, Chang LH, James TL and Narayan P (1992). "Phosphorus metabolite characterization of human prostatic adenocarcinoma in a nude mouse model by 31P magnetic resonance spectroscopy and high pressure liquid chromatography." *NMR in biomedicine* **5**(4): 185-92.

Kurhanewicz J, Swanson MG, Nelson SJ and Vigneron DB (2002). "Combined magnetic resonance imaging and spectroscopic imaging approach to molecular imaging of prostate cancer." *J Magn Reson Imaging* **16**(4): 451-63.

Kurhanewicz J, Swanson MG, Nelson SJ and Vigneron DB (2002). "Combined magnetic resonance imaging and spectroscopic imaging approach to molecular imaging of prostate cancer." *Journal of magnetic resonance imaging : JMRI* **16**(4): 451-63.

Kurhanewicz J, Vigneron DB, Nelson SJ, Hricak H, Macdonald JM, Konety B and Narayan P (1995). "Citrate as an in vivo marker to discriminate prostate cancer from benign prostatic hyperplasia and normal prostate peripheral zone: detection via localized proton spectroscopy." *Urology* **45**(3): 459-66.

Lan SJ and Henderson LM (1968). "Uptake of nicotinic acid and nicotinamide by rat erythrocytes." *J. Biol. Chem.* **243**(12): 3388-94.

Lane A and Fan T (2007). "Quantification and identification of isotopomer distributions of metabolites in crude cell extracts using 1H TOCSY." *Metabolomics* **3**(2): 79-86.

Lane AN, Fan TW, Higashi RM, Tan J, Bousamra M and Miller DM (2009). "Prospects for clinical cancer metabolomics using stable isotope tracers." *Experimental and Molecular Pathology* **86**(3): 165-73.

Lei H, Morgenthaler F, Yue T and Gruetter R (2007). "Direct validation of in vivo localized 13C MRS measurements of brain glycogen." *Magnetic resonance in medicine : official journal of the Society of Magnetic Resonance in Medicine / Society of Magnetic Resonance in Medicine* **57**(2): 243-8.

Levin YS, Mayer D, Yen Y-F, Hurd RE and Spielman DM (2007). "Optimization of fast spiral chemical shift imaging using least squares reconstruction: application for hyperpolarized (13)C metabolic imaging." *Magnetic resonance in medicine : official journal of the Society of Magnetic Resonance in Medicine / Society of Magnetic Resonance in Medicine* **58**(2): 245-52.

Lindon JC and Nicholson JK (2004). "Toxicological applications of magnetic resonance." *Proc Nucl Magn Reson Spectrosc* **45**: 109-143.

Lu D, Mulder H, Zhao P, Burgess SC, Jensen MV, Kamzolova S, Newgard CB and Sherry AD (2002). "13C NMR isotopomer analysis reveals a connection between pyruvate cycling and glucose-stimulated insulin secretion (GSIS)." *Proc. Natl. Acad. Sci. U.S.A.* **99**(5): 2708-13.

Lundberg P, Roy S and Kuchel PW (1994). "Immobilization methods for NMR studies of cellular metabolism--a practical guide." *Immunomethods* **4**(2): 163-78.

Lyon RC, Faustino PJ and Cohen JS (1986). "A perfusion technique for 13C NMR studies of the metabolism of 13C-labeled substrates by mammalian cells." *Magn Reson Med* **3**(5): 663-72.

Macdonald J, Griffin J, Kubota H, Griffith L, Fair J and Reid L (1999). Bioartificial Livers. Boston, Birkhauser.

Macdonald J, Xu A, Kubota H, Rong Y, Moss N, Lodestro C, Luntz T, Wolfe S and Reid L (2001). Epithelial Cell Culture: Liver. Methods of Tissue Engineering. W. Lanza, R. Langer and J. Vacanti. San Diego, CA, Academic Press. **1:** 151-201.

Macdonald JM, Grillo M, Schmidlin O, Tajiri DT and James TL (1998). "NMR spectroscopy and MRI investigation of a potential bioartificial liver." *NMR in biomedicine* **11**(2): 55-66.

Macdonald JM, Haas AL and London RE (2000). "Novel mechanism of surface catalysis of protein adduct formation. NMR studies of the acetylation of ubiquitin." *J Biol Chem* **275**(41): 31908-13.

Macdonald JM, Kurhanewicz J, Dahiya R, Espanol MT, Chang LH, Goldberg B, James TL and Narayan P (1993). "Effect of glucose and confluency on phosphorus metabolites of perfused human prostatic adenocarcinoma cells as determined by 31P MRS." *Magnetic resonance in medicine : official journal of the Society of Magnetic Resonance in Medicine / Society of Magnetic Resonance in Medicine* **29**(2): 244-8.

Macdonald JM, LeBlanc DA, Haas AL and London RE (1999). "An NMR analysis of the reaction of ubiquitin with [acetyl-1-13C]aspirin." *Biochem Pharmacol* **57**(11): 1233-44.

Macdonald JM, Schmidlin O and James TL (2002). "In vivo monitoring of hepatic glutathione in anesthetized rats by 13C NMR." *Magnetic resonance in medicine : official journal of the Society of Magnetic Resonance in Medicine / Society of Magnetic Resonance in Medicine* **48**(3): 430-9.

Maharjan RP and Ferenci T (2003). "Global metabolite analysis: the influence of extraction methodology on metabolome profiles of Escherichia coli." *Anal. Biochem.* **313**(1): 145-54.

Mancuso A, Beardsley NJ, Wehrli S, Pickup S, Matschinsky FM and Glickson JD (2004). "Real-time detection of 13C NMR labeling kinetics in perfused EMT6 mouse mammary tumor cells and betaHC9 mouse insulinomas." *Biotechnol Bioeng* **87**(7): 835-48.

Mancuso A, Fernandez EJ, Blanch HW and Clark DS (1990). "A nuclear magnetic resonance technique for determining hybridoma cell concentration in hollow fiber bioreactors." *Biotechnology (NY)* **8**(12): 1282-5.

Mancuso A, Zhu A, Beardsley NJ, Glickson JD, Wehrli S and Pickup S (2005). "Artificial tumor model suitable for monitoring 31P and 13C NMR spectroscopic changes during chemotherapy-induced apoptosis in human glioma cells." *Magnetic resonance in medicine : official journal of the Society of Magnetic Resonance in Medicine / Society of Magnetic Resonance in Medicine* **54**(1): 67-78.

Mason GF, Petersen KF, de Graaf RA, Shulman GI and Rothman DL (2007). "Measurements of the anaplerotic rate in the human cerebral cortex using 13C magnetic resonance spectroscopy and [1-13C] and [2-13C] glucose." *J Neurochem* **100**(1): 73-86.

Masson S and Quistorff B (1992). "The 31P NMR visibility of ATP in perfused rat liver remains about 90%, unaffected by changes of metabolic state." *Biochemistry* **31**(33): 7488-93.

Massou S, Nicolas C, Letisse F and Portais J-C (2007). "NMR-based fluxomics: quantitative 2D NMR methods for isotopomers analysis." *Phytochemistry* **68**(16-18): 2330-40.

Mayer D, Levin YS, Hurd RE, Glover GH and Spielman DM (2006). "Fast metabolic imaging of systems with sparse spectra: application for hyperpolarized 13C imaging." *Magn Reson Med* **56**(4): 932-7.

McClelland RE, Macdonald JM and Coger RN (2003). "Modeling O2 transport within engineered hepatic devices." *Biotechnol Bioeng* **82**(1): 12-27.

McLimans WF, Blumenson LE and Tunnah KV (1968). "Kinetics of Gas Diffusion in Mammalian Cell Culture Systems. II. Theory." *Biotechnol Bioeng* **X**: 741-763.

Merritt ME, Harrison C, Mander W, Malloy CR and Sherry AD (2007). "Dipolar cross-relaxation modulates signal amplitudes in the (1)H NMR spectrum of hyperpolarized [(13)C]formate." *J. Magn. Reson.* **189**(2): 280-5.

Merritt ME, Harrison C, Storey C, Jeffrey FM, Sherry AD and Malloy CR (2007). "Hyperpolarized 13C allows a direct measure of flux through a single enzyme-catalyzed step by NMR." *Proc Natl Acad Sci U S A* **104**(50): 19773-7.

Miccheli A, Tomassini A, Puccetti C, Valerio M, Peluso G, Tuccillo F, Calvani M, Manetti C and Conti F (2006). "Metabolic profiling by 13C-NMR spectroscopy: [1,2-13C2]glucose reveals a heterogeneous metabolism in human leukemia T cells." *Biochimie* **88**(5): 437-48.

Mørch YA, Donati I, Strand BL and Skjåk-Braek G (2006). "Effect of Ca2+, Ba2+, and Sr2+ on alginate microbeads." *Biomacromolecules* **7**(5): 1471-80.

Munger J, Bennett BD, Parikh A, Feng X-J, Mcardle J, Rabitz HA, Shenk T and Rabinowitz JD (2008). "Systems-level metabolic flux profiling identifies fatty acid synthesis as a target for antiviral therapy." *Nat Biotechnol* **26**(10): 1179-86.

Murtas S, Capuani G, Dentini M, Manetti C, Masci G, Massimi M, Miccheli A and Crescenzi V (2005). "Alginate beads as immobilization matrix for hepatocytes perfused in a bioreactor: a physico-chemical characterization." *Journal of biomaterials science Polymer edition* **16**(7): 829-46.

Narayan KS, Moress EA, Chatham JC and Barker PB (1990). "31P NMR of mammalian cells encapsulated in alginate gels utilizing a new phosphate-free perfusion medium." *NMR in biomedicine* **3**(1): 23-6.

Nicholas PC, Kim D, Crews FT and Macdonald JM (2008). "1H NMR-based metabolomic analysis of liver, serum, and brain following ethanol administration in rats." *Chem Res Toxicol* **21**(2): 408-20.

Overhauser AW (1953). "Polarization of Nuclei in Metals." *Phys Rev* **92**(2): 411-415.

Pasternack LB, Laude DA, Jr. and Appling DR (1994). "13C NMR analysis of intercompartmental flow of one-carbon units into choline and purines in Saccharomyces cerevisiae." *Biochemistry* **33**(1): 74-82.

Pauling L, Robinson AB, Teranishi R and Cary P (1971). "Quantitative analysis of urine vapor and breath by gas-liquid partition chromatography." *Proc Natl Acad Sci U S A* **68**(10): 2374-6.

Peng H, Long F and Ding C (2005). "Feature Selection Based on Mutual Information: Criteria of Max-Dependency, Max-Relevance, and Min-Redundancey." *IEEE* **27**(8): 1226-1238.

Petersen A, Kappler F, Szwergold BS and Brown TR (1992). "Fructose metabolism in the human erythrocyte. Phosphorylation to fructose 3-phosphate." *Biochem J* **284 (Pt 2)**: 363-6.

Pilatus U, Shim H, Artemov D, Davis D, vanZijl PCM and Glickson JD (1997). "Intracellular volume and apparent diffusion constants of perfused cancer cell cultures, as measured by NMR." *Magnetic Resonance in Medicine* **37**(6): 825-832.

Pravica MG and Weitekamp DP (1998). "Net NMR Alignment by Adiabatic Transport of Parahydrogen Addition Products to High Magnetic Field." *Chemical Physics Letters* **145**(4): 255-258.

Rahimi A and Recht B (2004). "Clustering with normalized cuts is clustering with a hyperplane." *Statistical Learning in Computer Vision*.

Randers-Eichhorn L, Bartlett RA, Frey DD and Rao G (1996). "Noninvasive oxygen measurements and mass transfer considerations in tissue culture flasks." *Biotechnol Bioeng* **51**(4): 466-78.

Ratiney H, Sdika M, Coenradie Y, Cavassila S, van Ormondt D and Graveron-Demilly D (2005). "Time-domain semi-parametric estimation based on a metabolite basis set." *NMR in biomedicine* **18**(1): 1-13.

Reddy TJ, Iwama T, Halpern HJ and Rawal VH (2002). "General synthesis of persistent trityl radicals for EPR imaging of biological systems." *J Org Chem* **67**(14): 4635-9.

Reeder SB, Brittain JH, Grist TM and Yen Y-F (2007). "Least-squares chemical shift separation for (13)C metabolic imaging." *Journal of magnetic resonance imaging : JMRI* **26**(4): 1145-52.

Rekharsky MV and Inoue Y (1998). "Complexation thermodynamics of cyclodextrins." *Chemical Reviews* **98**(5): 1875-1917.

Ronen S and Degani H (1989). "Studies of the metabolism of human breast cancer spheroids by NMR." *Magn Reson Med* **12**(2): 274-81.

Ronen SM, Stier A and Degani H (1990). "NMR studies of the lipid metabolism of T47D human breast cancer spheroids." *FEBS Lett* **266**(1-2): 147-9.

Ruoslahti E (1996). "RGD and other recognition sequences for integrins." *Annu Rev Cell Dev Biol* **12**: 697-715.

Saks V (2007). Molecular System Bioenergetics: Energy for Life, Wiley.

Santos C, Kurhanewicz J, Keshari K, Butler T, Joun D, Nelson S, Vigneron D and Swanson M (in press). "Correlation of Choline-Containing Metabolites with Gene Expression of Kennedy Cycle Enzymes." *NMR in biomedicine*.

Schindler M, Grabski S, Hoff E and Simon SM (1996). "Defective pH regulation of acidic compartments in human breast cancer cells (MCF-7) is normalized in adriamycin-resistant cells (MCF-7adr)." *Biochemistry* **35**(9): 2811-7.

Schlattner U, Tokarska-Schlattner M and Wallimann T (2006). "Mitochondrial creatine kinase in human health and disease." *Biochim Biophys Acta* **1762**(2): 164-80.

Schneider HJ, Hacket F, Rudiger V and Ikeda H (1998). "NMR studies of cyclodextrins and cyclodextrin complexes." *Chemical Reviews* **98**(5): 1755-1785.

Schroeder MA, Atherton HJ, Ball DR, Cole MA, Heather LC, Griffin JL, Clarke K, Radda GK and Tyler DJ (2009). "Real-time assessment of Krebs cycle metabolism using hyperpolarized 13C magnetic resonance spectroscopy." *The FASEB Journal*.

Schroeder MA, Cochlin LE, Heather LC, Clarke K, Radda GK, Tyler DJ and Shulman RG (2008). "In vivo assessment of pyruvate dehydrogenase flux in the heart using hyperpolarized carbon-13 magnetic resonance." *Proceedings of the National Academy of Sciences of the United States of America* **105**(33): 12051-12056.

Seo Y, Murakami M, Watari H, Imai Y, Yoshizaki K, Nishikawa H and Morimoto T (1983). "Intracellular pH determination by a 31P-NMR technique. The second dissociation constant of phosphoric acid in a biological system." *J Biochem* **94**(3): 729-34.

Serp D, Cantana E, Heinzen C, Von Stockar U and Marison IW (2000). "Characterization of an encapsulation device for the production of monodisperse alginate beads for cell immobilization." *Biotechnol Bioeng* **70**(1): 41-53.

Shanaiah N, Desilva MA, Nagana Gowda GA, Raftery MA, Hainline BE and Raftery D (2007). "Class selection of amino acid metabolites in body fluids using chemical derivatization and their enhanced 13C NMR." *Proc Natl Acad Sci U S A* **104**(28): 11540-4.

Shannon CE (1948). "A Mathematical Theory of Communication." *Bell Syst. Tech. J.* **27**: 379-423.

Shi J and Malik J (2000). "Normalized Cuts and Image Segmentation." *IEEE Trans. on Pattern Analysis and Machine Intelligence* **22**(8): 888-904.

Shulman GI, Rothman DL, Smith D, Johnson CM, Blair JB, Shulman RG and DeFronzo RA (1985). "Mechanism of liver glycogen repletion in vivo by nuclear magnetic resonance spectroscopy." *J. Clin. Invest.* **76**(3): 1229-36.

Sibson NR, Dhankhar A, Mason GF, Behar KL, Rothman DL and Shulman RG (1997). "In vivo 13C NMR measurements of cerebral glutamine synthesis as evidence for glutamate-glutamine cycling." *Proc Natl Acad Sci USA* **94**(6): 2699-704.

Skoog M, Johansson G, Olsson B and Appelqvist R (1988). "Fructose Determination Using Immobilized Enzymes in a Flow System with Special Emphasis on the Effect of Isomerism." *Mikrochimica Acta* **III**: 131-142.

Sreekumar A, Poisson LM, Rajendiran TM, Khan AP, Cao Q, Yu J, Laxman B, Mehra R, Lonigro RJ, Li Y, Nyati MK, Ahsan A, Kalyana-Sundaram S, Han B, Cao X, Byun J, Omenn GS, Ghosh D, Pennathur S, Alexander DC, Berger A, Shuster JR, Wei JT, Varambally S, Beecher C and Chinnaiyan AM (2009). "Metabolomic profiles delineate potential role for sarcosine in prostate cancer progression." *Nature* **457**(7231): 910-4.

Starling EH (1896). "On the Absorption of Fluids from the Connective Tissue Spaces." *J Physiol* **19**(4): 312-26.

Stephanopoulos G and Gill RT (2001). Metabolic Engineering. Heidelberg, Springer Berlin.

Strong P, Mullings R and Illingworth JA (1979). "Aerobic lactate synthesis by cardiac muscle." *Eur J Biochem* **102**(2): 625-36.

Swanson M, Keshari KR, Tabatabai Z, Simko J, Shinohara K, Carroll P, Zektzer A and Kurhanewicz J (2008). "Quantification of choline- and ethanolamine-containing metabolites in human prostate tissues using (1)H HR-MAS total correlation spectroscopy." *Magnetic resonance in medicine : official journal of the Society of Magnetic Resonance in Medicine / Society of Magnetic Resonance in Medicine* **60**(1): 33-40.

Swanson MG, Vigneron DB, Tabatabai ZL, Males RG, Schmitt L, Carroll PR, James JK, Hurd RE and Kurhanewicz J (2003). "Proton HR-MAS spectroscopy and quantitative pathologic analysis of MRI/3D-MRSI-targeted postsurgical prostate tissues." *Magnetic resonance in medicine : official journal of the Society of Magnetic Resonance in Medicine / Society of Magnetic Resonance in Medicine* **50**(5): 944-54.

Syrota A, Samson Y, Boullais C, Wajnberg P, Loc'h C, Crouzel C, Maziere B, Soussaline F and Baron JC (1985). "Tomographic mapping of brain intracellular pH and extracellular water space in stroke patients." *J Cereb Blood Flow Metab* **5**(3): 358-68.

Tessem M-B, Swanson MG, Keshari KR, Albers MJ, Joun D, Tabatabai ZL, Simko JP, Shinohara K, Nelson SJ, Vigneron DB, Gribbestad IS and Kurhanewicz J (2008). "Evaluation of lactate and alanine as metabolic biomarkers of prostate cancer using 1H HR-MAS spectroscopy of biopsy tissues." *Magnetic resonance in medicine : official journal of the Society of Magnetic Resonance in Medicine / Society of Magnetic Resonance in Medicine* **60**(3): 510-6.

Thelwall PE, Yemin AY, Gillian TL, Simpson NE, Kasibhatla MS, Rabbani ZN, Macdonald JM, Blackband SJ and Gamcsik MP (2005). "Noninvasive in vivo detection of glutathione metabolism in tumors." *Cancer Res.* **65**(22): 10149-53.

Thomsen HS (2008). "Is NSF only the tip of the "gadolinium toxicity" iceberg?" *J Magn Reson Imaging* **28**(2): 284-6.

Tong X, Zhao F and Thompson CB (2009). "The molecular determinants of de novo nucleotide biosynthesis in cancer cells." *Curr Opin Genet Dev* **19**(1): 32-7.

Tyagi RK, Azrad A, Degani H and Salomon Y (1996). "Simultaneous extraction of cellular lipids and water-soluble metabolites: evaluation by NMR spectroscopy." *Magn Reson Med* **35**(2): 194-200.

Unkefer CJ and London RE (1984). "In vivo studies of pyridine nucleotide metabolism in Escherichia coli and Saccharomyces cerevisiae by carbon-13 NMR spectroscopy." *J. Biol. Chem.* **259**(4): 2311-20.

van de Ven F (1995). Multidimensional NMR in Liquids: Basic Principles and Experimental Methods. New York, Wiley-VCH.

Van de Wiele C, Dumont F, Dierckx RA, Peers SH, Thornback JR, Slegers G and Thierens H (2001). "Biodistribution and dosimetry of (99m)Tc-RP527, a gastrin-releasing peptide (GRP) agonist for the visualization of GRP receptor-expressing malignancies." *J Nucl Med* **42**(11): 1722-7.

van der Zijden JP, van Eijsden P, de Graaf RA and Dijkhuizen RM (2008). "1H/13C MR spectroscopic imaging of regionally specific metabolic alterations after experimental stroke." *Brain* **131**(Pt 8): 2209-19.

van Zijl PCM, Jones CK, Ren J, Malloy CR and Sherry AD (2007). "MRI detection of glycogen in vivo by using chemical exchange saturation transfer imaging (glycoCEST)." *Proc. Natl. Acad. Sci. U.S.A.* **104**(11): 4359-64.

Vizán P, Alcarraz-Vizán G, Díaz-Moralli S, Solovjeva O, Frederiks W and Cascante M (2009). "Modulation of pentose phosphate pathway during cell cycle progression in human colon adenocarcinoma cell line HT29." *Int J Cancer* **124**(12): 2789-96.

Vlachostergios PJ, Patrikidou A, Daliani DD and Papandreou CN (2009). "The Ubiquitin-Proteasome System in cancer, a major player in DNA Repair. Part 1: Post-translational regulation." *J Cell Mol Med*.

Vlachostergios PJ, Patrikidou A, Daliani DD and Papandreou CN (2009). "The Ubiquitin-Proteasome System in cancer, a major player in DNA Repair. Part 2: Transcriptional regulation." *J Cell Mol Med*.

Voet D and Voet JG (2004). Biochemistry. New York, J. Wiley & Sons.

Wang CS (1977). "Inhibition of human erythrocyte lactate dehydrogenase by high concentrations of pyruvate. Evidence for the competitive substrate inhibition." *Eur J Biochem* **78**(2): 569-74.

Wang Y, Holmes E, Nicholson JK, Cloarec O, Chollet J, Tanner M, Singer BH and Utzinger J (2004). "Metabonomic investigations in mice infected with Schistosoma mansoni: an approach for biomarker identification." *Proc Natl Acad Sci U S A* **101**(34): 12676-81.

Wang YM and van Eys J (1981). "Nutritional significance of fructose and sugar alcohols." *Annu Rev Nutr* **1**: 437-75.

Warburg O (1956). "On the origin of cancer cells." *Science* **123**(3191): 309-14.

Warburg O, Wind F and Negelein E (1927). "The Metabolism of Tumors in the body." *The Journal of General Physiology*: 519-530.

Warren WS, Jenista E, Branca RT and Chen X (2009). "Increasing hyperpolarized spin lifetimes through true singlet eigenstates." *Science* **323**(5922): 1711-4.

Weber A, Groyer-Picard MT, Franco D and Dagher I (2009). "Hepatocyte transplantation in animal models." *Liver Transpl* **15**(1): 7-14.

Wilson DM, Hurd RE, Keshari KR, Van Criekinge M, Chen AP, Nelson SJ, Vigneron DB and Kurhanewicz J (2009). "Generation of hyperpolarized substrates by secondary labeling with [1,1-13C] acetic anhydride." *Proc. Natl. Acad. Sci. U.S.A.* **106**(14): 5503-7.

Wilton DC (1979). "The mechanism of adduct formation between NAD+ and pyruvate bound to pig heart lactate dehydrogenase." *Biochem J* **177**(3): 951-7.

Wolfe SP, Hsu E, Reid LM and Macdonald JM (2002). "A novel multi-coaxial hollow fiber bioreactor for adherent cell types. Part 1: hydrodynamic studies." *Biotechnol Bioeng* **77**(1): 83-90.

Yang CH and Williams JM (2004). "Palladium-catalyzed cyanation of aryl bromides promoted by low-level organotin compounds." *Organic Letters* **6**(17): 2837-2840.

Young WF, Jr. (2007). "Clinical practice. The incidentally discovered adrenal mass." *N Engl J Med* **356**(6): 601-10.

Zamora-León SP, Golde DW, Concha II, Rivas CI, Delgado-López F, Baselga J, Nualart F and Vera JC (1996). "Expression of the fructose transporter GLUT5 in human breast cancer." *Proc. Natl. Acad. Sci. U.S.A.* **93**(5): 1847-52.